University of Leoben

Dissertation

FRACTURE & FATIGUE OF INHOMOGENEOUS MATERIALS

Dipl.-Ing. Johannes Zechner

Leoben, December 2012

Financial support by the Austrian Federal Government and the Styrian Provincial Government within the research activities of the K2 Competence Center “Integrated Research in Materials, Processing and Product Engineering”, under the frame of the Austrian COMET Competence Center Program, is gratefully acknowledged (Project A4.11-WP2).

Erich Schmid Institute of Materials Science
Austrian Academy of Sciences
Jahnstrasse 12
A-8700 Leoben

Affidavit

I declare in lieu of oath, that I wrote this thesis
and performed the associated research myself,
using only literature cited in this volume.

_____

Dipl. Ing. Johannes Zechner

Leoben, December 2012

Danksagung

Für meine Doktorarbeit schulde ich sehr vielen Menschen einen herzlichen Dank.

Besonders bedanken möchte ich mich bei Prof. Otmar Kolednik für die Betreuung der Doktorarbeit, die unzähligen fachlichen Diskussionen und seine Mühe, mir die Welt der Bruchmechanik näherzubringen.

Gedankt sei auch allen nicht wissenschaftlichen Mitarbeitern des Erich Schmid Instituts, besonders Franz Hubner für die ausgezeichnete Proben- und Bauteilfertigung und Peter Kutlesa für die Hilfe und Unterstützung bei vielen Versuchen.

Ebenso möchte ich dem wissenschaftlichen Personal für viele Ideen und Hilfestellungen danken, besonders Prof. Reinhard Pippan, Anton Hohenwarter, Stefan Wurster, Megan Cordill, Peter Gruber und Marianne Kapp.

Eine große Hilfe bei der Probenvorbereitung und den Versuchen war meine studentische Mitarbeiterin Riccarda Rust, wofür ich ihr herzlichst Danken möchte.

Ein herzlicher Dank gebührt auch Jozef Predan von der Universität Marburg für die Unterstützung bei vielen Versuchen und seine Modellierungsarbeiten.

Bei Herrn Dr. Henkel von der AMAG rolling GmbH möchte ich mich für die hochfesten Aluminiumbleche bedanken, die die Firma gratis zur Verfügung gestellt hat.

Meiner Familie und meinen Freunden sei besonders für Unterstützung und Rückhalt während der Dissertation gedankt.

"It is not because things are difficult that we do not dare; it is because we do not dare that they are difficult."

Lucius Annaeus Seneca, Epistulae Morales

1

INTRODUCTION

1.1 Motivation

In traditional structural design a material is chosen as adequate for a certain application, if the predicted applied stress is lower than the yield stress of the material. This approach is based on the assumption that the structure is free of cracks and crack like flaws. If such cracks, which could be introduced during manufacturing or by mechanical or corrosive damage, are present, the load bearing capacity of the structure could be drastically reduced. Stress concentrations around the crack tip are responsible for this behavior, which might lead to component fracture.

In the middle of the 20th century, a design approach, which considers the presence of cracks, was developed in the then new field of fracture mechanics. It takes into account three variables for the design of structures: Like in the traditional approach the applied stress, furthermore a crack size and, replacing the yield strength, a material parameter called fracture toughness. The fracture toughness describes the resistance of a material to the growth of a pre-existing flaw. The task of fracture mechanics is to describe the interactions of the three variables and to correctly determine the fracture toughness experimentally [1].

Besides the problem of fracture of a cracked body under monotonic loading, another damage mechanism, not covered in traditional structural design, can lead to premature material failure. This damage mechanism is called fatigue and may occur whenever a component is subjected to cyclic stresses or strains that produce permanent damage. Since their introduction, the concepts and tools of fracture mechanics have also been used to characterize fatigue crack growth.

Most of the work conducted in fracture mechanics and fatigue, both analytically and experimentally, have treated homogeneous structural materials, for example metals, ceramics or polymers. In contrast to that, many technical structures consist of inhomogeneous materials or material combinations, e.g. brazed, welded or glued joints or the rapidly growing field of composite materials. Gaining a deeper understanding of the effect a material inhomogeneity has on the fracture and fatigue behavior of a structure is necessary to be able to properly design such structures and to predict their behavior.

Furthermore an understanding of these processes could allow the design and construction of new composite materials with unique property combinations, such as high strength and high fracture toughness, which are often not achievable in one homogeneous material. Several biological materials, like certain deep-sea glas sponges, serve as model materials for such composite designs and received growing attention in the last years due to their exceptional combination of stiffness and toughness.

1.2 Literature survey – state of the art

As multilayer materials are highly anisotropic, which means that their properties are depending on the direction in the material, it is important to distinguish between the studied geometries. Knowledge about the relationship between the orientation of the crack growth plane and the orientation of the layers is important for fracture and fatigue studies of multilayer systems. In general two types of cracked multilayered structures, denominated crack arrester and crack divider configurations are investigated with respect to the fracture and fatigue behavior. In the crack arrester (CA) configuration, see Fig. 1.1a, the crack grows perpendicularly to the layers and through one layer after another. In the crack divider (CD) configuration, the crack also propagates perpendicular to the layers, but through all layers at once, Fig. 1.1b.

Besides the differentiation with respect to the multilayer orientation, it is also necessary to divide the multilayer systems into groups with respect to the multilayer compositions to allow a systematic study of the effects. Two types of inhomogeneities are distinguished here denominated as elastic- and yield stress- inhomogeneities. If the materials combined in the multilayers have a large difference in the elastic properties, e.g. the Young's modulus, the inhomogeneity is denominated as elastic. The constituent with the higher Young's modulus is denominated stiff, the one with the lower Young's modulus compliant; therefore multilayers with an elastic inhomogeneity are also called stiff/compliant multilayers. Multilayers with a yield strength inhomogeneity have the same elastic properties but a variation in the yield strength. The material with higher yield strength is designated as hard, the one with the lower as soft, consequently these structures are also referred to as hard/soft multilayers.

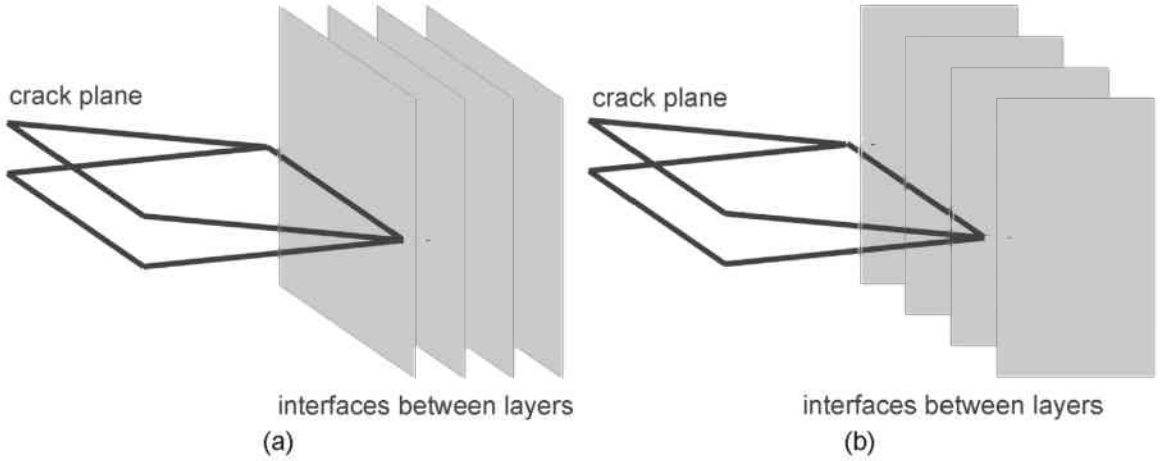

Fig. 1.1 The (a) crack arrester and (b) crack divider configurations.

1.2.1 Fracture of inhomogeneous materials

Classical toughening mechanisms of multilayers

The fracture behavior of layered inhomogeneous metallic materials has been experimentally investigated intensively since the 1970's. Embury et al. [2] were the first to study the fracture behavior of brazed and explosion clad steel multilayers in CA and CD configuration using Charpy impact tests in 1967. Since then numerous studies have been published covering different material combinations and various test methods: Lesuer et al. [3] and Wadsworth et al. [4] published reviews on the investigations on metal/metal laminates and Embury et al. [5] one especially focusing on steel/steel laminates. Most of the work conducted focused on the effects the interlayers have on the impact behavior, but also fracture toughness tests have been conducted. Impact tests on aluminum-based metal/metal composites in CA configuration were recently conducted by Cepeda-Jimenez et al. [6,7].

The fracture behavior of metal/polymer multilayers was first investigated by Alic et al. [8] and Kaufmann et al. [9], who determined crack growth resistance curves in terms of the stress intensity factor K for adhesively bonded aluminum sheets in CD configuration. Metal/polymer laminates received increasing attention in recent years due to the introduction of fiber metal laminates such as Glare and Arall [10,11], consisting of high strength metal sheets bonded with fiber reinforced epoxy resins. The main focus of these works was on the impact behavior of the laminates in CA configuration, see the review by Sadighi et al. [12], but also the fracture toughness has been investigated in CD configuration [13,14].

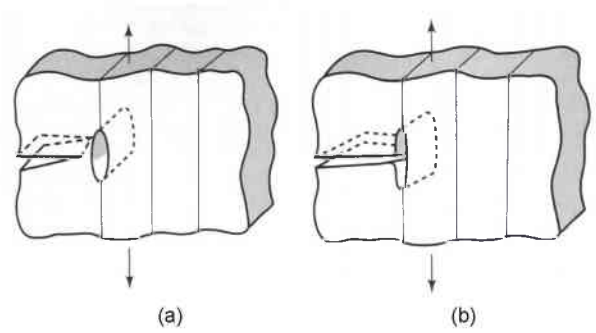

Fig. 1.2 (a) Delamination ahead of the crack tip and (b) crack tip blunting [15].

Summarizing the results of the aforementioned works, it can be concluded that the multilayer structures in CA configuration in general exhibit highly improved impact toughness, i.e. a shift of the transition temperature to lower temperatures, or higher fracture resistance if compared to the homogeneous constituents. Also the specimens tested in CD configuration show a superior impact- and fracture toughness to that of the homogeneous constituents.

The improvement of the impact- or fracture toughness by the introduction of interlayers in CA configuration is classically reported to be caused by the delamination of weak interfaces in front of the crack tip. A weak interface in front of the crack tip can be pulled apart by the tensile stresses acting in crack growth direction in the crack tip field [15]. The delamination generates an internally free surface, see Fig. 1.2a, which reduces the crack tip triaxiality as the stress component acting normal to the free surface has to be zero. Additionally the crack tip blunts if the initial crack grows into the delaminated interface, which also reduces the local stress intensity, see Fig. 1.2b. Caused by the delamination, the crack can arrest at the interface and has to be re-nucleated in the adjacent layer, which consumes a high amount of energy and can markedly increase the impact- or fracture toughness.

The main contribution to toughening in the CD configuration is attributed to a local change in the stress state at the crack tip, caused by interface delamination. Delamination causes the specimen to act like a series of thin-plane stress samples, instead of one thick-plane strain sample. The thin samples exhibit a higher fracture toughness than the thick one as the degree of plastic constraint acting on the crack tip is smaller and the material volume capable of plastic deformation is higher. The dependence of the critical Mode I fracture toughness K_I on specimen thickness is sketched in Fig. 1.3, where the decrease in K_I with increasing thickness is clearly visible. Therefore, the series of thin samples with the same total thickness as the thick specimen have higher fracture toughness than the thick one.

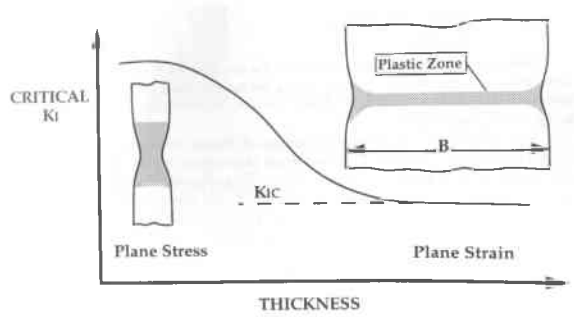

Fig. 1.3 Effect of specimen thickness on Mode I fracture toughness [1].

The material inhomogeneity effect

The classical toughening mechanisms like crack deflection and blunting are not sufficient to describe the exceptional resistance to fracture of several layered biological materials, e.g. the deep-sea sponge Euplectella aspergillum [16]. An additional effect resulting from the variation of the mechanical properties of the constituents of the multilayers was found to strongly influence the fracture behavior of multilayer materials [16]. This effect, denominated material inhomogeneity effect was treated in several theoretical and numerical studies in the last decade. A detailed introduction to and explanation for the material inhomogeneity effect is given in Chapter 3. It is important to note that the material inhomogeneity effect, in contrast to the classical toughening mechanisms of multilayers, is also acting if no interface delamination occurs.

1.2.2 Fatigue in inhomogeneous materials

A short literature overview about fatigue in multilayered materials in the CD and CA configurations is given, with respect to the type of investigated inhomogeneity.

Elastic inhomogeneities

Numerous elastically inhomogeneous multilayer systems have been investigated with respect to their fatigue behavior, including metal/metal and metal/polymer systems.

The fatigue behavior of discontinuously reinforced aluminum (DRA), laminated with high strength aluminum alloys, was studied by the group of Lewandowski [17-19] for the CA configuration. They found an improved fatigue resistance, expressed by an increase in the fatigue threshold and a decrease in the Paris law slope. For both configurations, this behavior is partially attributed to the delamination of interfaces as described for the fracture behavior above. In CA configuration an additional improvement is found to result from the mismatch of the Young's modulus and the coefficient of thermal expansion of the constituents. According to [17] an increase in the Young's modulus in crack

growth direction in CA configuration decreases the local cyclic crack tip opening displacement and consequently the level of crack closure, which also influences the local effective stress intensity range. The difference of the coefficient of thermal expansion introduces thermal residual stresses in the laminate if they are tested at high or low temperature, which can, depending on if they are compressive or tensile in nature, strongly enhance or decrease the local crack driving force [22,23].

Due to their importance for the aerospace industry, fiber metal laminates were investigated intensively in the last years [19]. They were found to have a significantly improved fatigue resistance in CD configuration, as fatigue crack growth is constrained to the aluminum layers while in the resin layers unbroken fibers in the wake of the crack tip bridge the crack, which reduces the stresses at the crack tip [20].

Yield strength inhomogeneities

Most of the experimental work conducted on material combinations with a yield strength inhomogeneity in CA configuration has been carried out on steel/steel bimaterials with one sharp interface [24-27]. Suresh et al. [24] investigated fatigue crack growth in an austenitic/ferritic bimaterial, in which both steels have the same Young's modulus but the austenite is harder than the ferrite. They found that for a soft/hard transition the crack growth rate da/dN, at a constant applied stress intensity range ΔK, decreases to zero when the crack approaches the interface and the crack deflects away from the mode I growth plane. In this case the interface exerts a shielding effect on the crack tip. For the opposite case of a hard/soft transition, the crack grows through the interface along the mode I growth plane. A slight acceleration of the crack growth rate is observed for crack growth before the interface is reached, which is called an anti-shielding effect. Furthermore, it was found that acceleration or decrease in the crack growth rate starts when the plastic zone in front of the crack tip starts to interact with the interface. The crack arrest for the soft/hard transition is explained by two effects: First, the obstruction of cyclic slip in the plastic zone when it interacts with the interface, and secondly due to changes in the triaxiality in front of the crack tip.

Pippan et al. [25] conducted similar experiments on an iron/ferritic-steel bimaterial. This system has the advantage that both constituents have very similar Young's moduli and coefficients of thermal expansion. This is important, because it was found that the difference in the coefficients of thermal expansion between austenite and ferrite have an influence on the fatigue behavior that was not accounted for by Suresh et al. [24]. The acceleration and decrease of the crack growth rates was also observed in [25] for hard/soft and soft/hard transitions. A bifurcation of the crack in the vicinity of the soft/hard interfaces was observed for the soft/hard transitions at high applied ΔK values, which drastically reduces the crack driving force and leads to crack arrest in the soft

material. In the case of a low applied ΔK value, the fatigue crack was able to propagate through the interface into the hard material. Besides the experiments treating a single bimaterial interface, also the cases of a soft iron interlayer in the hard steel and a steel interlayer in iron were studied. In the first case, the fatigue crack grew into the soft interlayer, bifurcated at the soft/hard interface and arrested there. No crack growth through the soft interlayer into the hard material could be observed. In the opposite case, where the crack grew from the soft material towards the hard interlayer, the crack bifurcated at the first soft/hard interface.

Numerical studies on the fatigue behavior of multilayers

Only the most important works describing fatigue crack growth in multilayer materials should be listed here. Several numerical and analytical works were conducted to explain the shielding and anti-shielding effects on fatigue cracks in multilayer materials, e.g. by Sugimura et al. [28], Pippan et al. [29], Bhat et al. [27] and Kolednik et al [30]. Detailed literature surveys on the numerical work conducted in this field are given in [27,30].

1.3 Aim of the work

The purpose of this work is to contribute to the better understanding of the fracture and fatigue behavior of different types of inhomogeneities encountered in materials. The main questions the current study should answer are:

- How does the material inhomogeneity effect influence the fracture and fatigue behavior in multilayer materials?
- Which are the similarities and differences between structures with an elastic and a yield stress inhomogeneity?
- Can the material inhomogeneity effect in technical materials be used to create damage resistant structures?

To achieve this goal, experimental techniques for the production and fracture mechanical testing of these materials are developed. The experimental studies can be divided into three main groups:

1. The development of new techniques to determine the fracture toughness of short fiber composites.
2. Fracture mechanical investigations on the influence of different types of material inhomogeneities on the fracture behavior of multilayer composites.
3. The fatigue behavior of multilayer structures is studied with respect to the different types of inhomogeneities.

To gain a better understanding of the observed effects, the experimental work is supported by numerical analysis using the concept of configurational forces.

2

FUNDAMENTALS OF FRACTURE MECHANICS

2.1 Preface

An introduction into the principles of fracture mechanics, as far as they are of interest for this work, should be given in this chapter. A complete overview of the field is given in several monographies, e.g. the books by Anderson [1] and Broek [31], on which this chapter is based.

Fracture mechanics is used to describe damage and fracture processes in materials that are already containing defects by the use of concepts of continuum mechanics. Classical fracture mechanics concepts distinguish between linear-elastic and elastic-plastic fracture mechanics. In both cases it is possible to describe the stress- and strain-fields in front of a sharp crack tip by a single parameter, denominated stress intensity factor K for the linear-elastic and J-integral J for the elastic-plastic case. Linear-elastic fracture mechanics has been developed to describe fracture in ideally brittle materials and can be applied only if very limited plastic deformation occurs in front of the crack tip. This is generally not the case for the materials used in this work; therefore elastic-plastic fracture mechanics is used.

2.2 Elastic-plastic fracture mechanics

In materials where initiation of crack growth and crack propagation are accompanied by considerable plastic deformations, elastic-plastic fracture mechanics has to be used. Two approaches are widely used to determine the fracture initiation toughness and crack growth toughness in elastic-plastic fracture mechanics: The first is the *CTOD*-concept, proposed by Wells [32,33], where a critical crack tip opening displacement (*CTOD*) is the parameter describing fracture initiation. The second is the J-integral concept introduced by Rice [34], which is widely used in this work for the experimental investigation of the fracture behavior of materials.

2.2.1 The crack tip opening displacement

In elastic-plastic materials an initially sharp crack tip blunts due to plastic deformation before fracture initiation. The amount of blunting prior to crack growth initiation increases with increasing material toughness, but is a constant for a material and denoted as the critical COD_i-value. The crack tip opening displacement can be converted into J-values (see next chapter) using,

$$J = m\sigma_F COD \ . \tag{2.1}$$

The dimensionless parameter m depends mainly on the strain hardening behavior of the material; for many cases $m \approx 2$. An average flow stress σ_F is calculated as the mean value of yield stress and tensile strength.

Several methods for the determination of COD_i have been proposed, the most precise one being the measurement of COD_i directly on the fracture surface using stereophotogrammetry [35]. One drawback of this method is the high experimental effort.

2.2.2 The *J*-integral

The J-integral is a path-independent contour integral, which equals the energy release rate in a nonlinear elastic body and is given by

$$J = -\frac{d\Pi}{dA} = \int_\Gamma \left(\phi dy - T_i \frac{\partial u_i}{\partial x} ds \right), \tag{2.2}$$

where Π is the potential energy and A the crack area. J is calculated along a counter-clockwise path Γ around the crack tip, see Fig. 2.1; The strain energy density ϕ is given by the equation,

$$\phi = \int_0^{\varepsilon_{ij}} \sigma_{ij} d\varepsilon_{ij} \ , \tag{2.3}$$

where σ_{ij} and ε_{ij} are the stress and strain tensors. T_i and u_i are the components of the traction and displacement vectors, respectively, and ds is a length increment along the contour Γ.

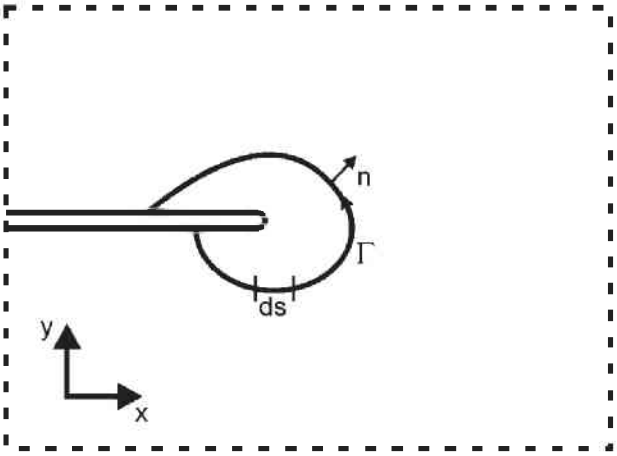

Fig. 2.1 Path Γ around the crack tip

The components of the traction vector are calculated from the relation,

$$T_i = \sigma_{ij} n_j , \tag{2.4}$$

where n_j are the components of the unit vector normal to Γ. The *J*-integral is only path independent if the material is homogeneous and no volume forces occur.

For a nonlinear elastic material the total strain energy density ϕ is reversible, whereas in an elastic-plastic material only the elastic portion of the strain energy density is reversible, while the plastic portion has been dissipated. Thus the *J*-integral does not characterize the crack driving force in elastic-plastic materials [36].

Hutchinson [37] and Rice and Rosengren [38] showed that the *J*-integral characterizes the intensity of the stress and strain fields, denominated HRR field, in front of the crack tip for a nonlinear elastic material. In an elastic-plastic material, a small zone around the crack tip, denominated process zone, undergoes high deformations, violating the assumed small strain conditions, and cannot be described by the HRR field. If a *J* dominated zone exists around the process zone, the *J*-integral can be used to experimentally determine the fracture initiation toughness or crack growth resistance curve in terms of the *J*-integral for elastic-plastic materials.

2.3 *J*-integral testing

The most widely used *J*-integral testing technique was introduced by Rice and allows the calculation of a *J*-value at a certain load or displacement from the load–displacement-curve of a single cracked specimen. This method is also the basis of most standards for fracture mechanical testing, e.g. ASTM E-1820 [39], ISO 12135 [40] and ESIS P2-92 [41], which are applied in this work.

2.3.1 Measuring the fracture initiation toughness

ASTM E-1820 describes the determination of crack growth resistance curves (J–Δa-curves) and the fracture initiation toughness J_{IC}. To evaluate the experimental J-integral the applied load P and resulting load-line-displacement have to be measured during a test. The experimental J is calculated from an elastic and a plastic component,

$$J = J_{el} + J_{pl} . \tag{2.5}$$

The elastic component is given by

$$J_{el} = \frac{K^2(1-\nu^2)}{E}, \tag{2.6}$$

with ν being the Poisson's ratio and E the Young's modulus. The stress intensity factor K is calculated from the applied load, the specimen thickness B, width W and crack length a according to [1],

$$K = \frac{P}{B\sqrt{W}} f\left(\frac{a}{W}\right). \tag{2.7}$$

The dimensionless geometry factor f(a/W) takes into account the type of specimen tested and is given in literature, e.g. the work by Tada et al. [42]. The most widely used specimen in the current study is the single edge notch tension (SENT or SE(T)) specimen, which can be either loaded via clamped ends or pins. The geometry factor varies for the two loading types and, for the clamped specimens, it is also dependent on the ratio of the distance between the clamps H and W. Cravero et al. [43] determined $f(a/W)$ for pin-loaded and clamped specimens with various H/W-ratios. The results are given by a fifth order polynomial fit,

$$f\left(\frac{a}{W}\right) = \xi_0 + \xi_1\left(\frac{a}{W}\right)^1 + \xi_2\left(\frac{a}{W}\right)^2 + \xi_3\left(\frac{a}{W}\right)^3 + \xi_4\left(\frac{a}{W}\right)^4 + \xi_5\left(\frac{a}{W}\right)^5 . \tag{2.8}$$

The polynomial coefficients ξ are provided in Table 2.1. It should be mentioned that in [1] an analytical expression is given for $f(a/W)$ of the pin-loaded specimen. Only for very short cracks and $a/W < 0.05$ a deviation of the results of [43] and [1] can be seen. In the technically important range $0.1 < a/W < 0.7$ both expressions yield the same results.

Table 2.1 Coefficients of the polynomial fitting given in Eq. (1.8), [43].

	ξ_0	ξ_1	ξ_2	ξ_3	ξ_4	ξ_5
Pin-loaded:	-0.072	11.6294	-61.6928	223.4007	-355.5166	239.3969
Clamped:						
H/W=2	0.239	4.7685	-10.839	22.8483	-25.1329	13.8204
H/W=4	0.2565	4.4604	-7.0538	18.6928	-19.4703	9.2523
H/W=6	0.2681	4.1916	-4.5098	12.5442	-6.4726	0.7304
H/W=8	0.2852	3.8168	-1.4522	3.5078	9.4071	-7.8491
H/W=10	0.2832	3.8497	-1.4885	4.1716	9.9094	-7.4188
H/W=20	0.2682	4.1767	-3.8639	14.9622	-7.9416	9.4143
H/W=50	0.0746	8.2866	-34.2306	117.6196	-165.6966	104.8546

The plastic component of the experimental *J*-integral J_{pl} is calculated from the dissipated plastic work A_{pl}, the specimen thickness *B* and ligament length $b_0 = W - a_0$,

$$J_{pl} = \frac{\eta_{pl} A_{pl}}{B b_0}. \tag{2.9}$$

The dimensionless factor η_{pl} in Eq. (2.9) was introduced by Sumpter [44] and Turner [45] to connect the plastic work A_{pl} to the plastic portion of the *J*-integral and is also given for many specimen types in literature. The plastic work is calculated by subtracting the elastic work A_{el} from the total applied work, which corresponds to the area under the load displacement curve. For the SENT specimen also η_{pl} was determined in [43]. If the load-line-displacement, like in the present work, is used for the *J*-integral evaluation, the η_{pl}-factor for both loading types, clamped ends and pin-loading, is dependent on *a/W*, *H/W* and the strain hardening coefficient *n.* No expressions are given for the η_{pl} calculation, instead it has to be measured from plots drawn in [43].

If, alternatively, the crack mouth opening displacement (*CMOD*) was used for the *J*-integral measurement, η_{pl} is only dependent on *a/W*, which facilitates the evaluation significantly.

To construct the *J*–Δa-curve it is necessary to measure the amount of crack extension Δa for every *J*-value. This can be done via two methods denominated single specimen technique and multiple specimen technique:

As the name suggests, in the single specimen technique only one specimen is needed to construct the complete *J*–Δa-curve. Therefore the crack extension is measured continuously or at several points during the test. The mostly used methods to measure Δa are the unloading compliance method and the potential drop technique. In the former, the specimen is partially unloaded several times during the test and Δa is calculated from the change in the specimen compliance [43]. In the latter, a direct or alternating electric potential

is applied to the specimen. The potential changes with crack growth and is monitored during the test. From the ratio of the actual potential V and the zero-potential V_0, the actual crack length a is calculated using the equation proposed by Johnson [46]:

$$a = \frac{2W}{\pi}\cos^{-1}\left\{\frac{\cosh\left(\frac{\pi y}{2W}\right)}{\cosh\left[\left(\frac{V}{V_0}\right)\cosh^{-1}\left(\cosh\left(\frac{\pi y}{2W}\right)/\cosh\left(\frac{\pi a_0}{2W}\right)\right)\right]}\right\}. \qquad (2.10)$$

The distance between the points where the potential is measured is $2y$ and the initial crack length is a_0. The potential change with crack extension is depending on the type of investigated material and requires a calibration of the technique for every material tested. Details on the calibration procedure and the application of the potential drop technique are given in ESIS P2-92 [41].

In the multiple specimen method, several specimens, who have the same initial crack length are loaded to different amounts of Δa. Afterwards, the specimens are unloaded and fatigued up to final fracture. From the fracture surfaces Δa can be measured optically.

Having determined both J and the corresponding Δa allows the construction of the crack growth resistance curve. An example is shown in Fig. 2.2. The first, steeply rising, part of the J–Δa-curve can be described by a so-called blunting line, given by

$$J = M\sigma_y\Delta a\ , \qquad (2.11)$$

with $M = 2$ for many materials.

The fracture initiation toughness J_{IC} is defined as the intersection of the J–Δa-curve, with a line parallel to the blunting line, which intersects the abscissa at Δa = 0.2 mm, denominated 0.2 mm offset line. J_{IC} is only a valid fracture initiation toughness value if certain qualification requirements, given in [38], are fulfilled. In cases where the qualification requirements are not fulfilled in this work, but the fracture initiation toughness is nevertheless given in terms of the J-integral, it is denominated J_i or J_c and defined explicitly.

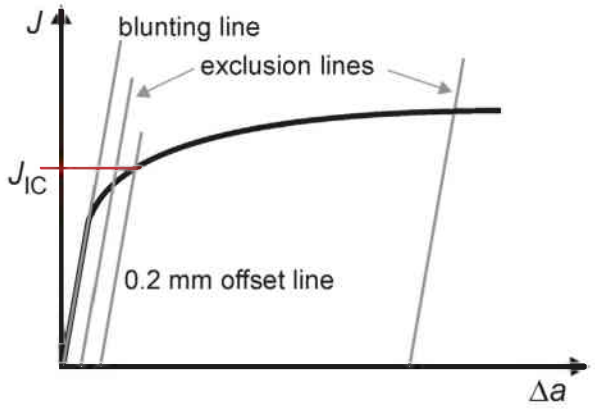

Fig. 2.2 Schematic of a crack growth resistance curve in terms of the *J*-integral with the blunting- and the 0.2 mm offset line.

2.3.2 The crack growth corrected *J*-integral

If not only the fracture initiation toughness but the complete run of the *J*–Δ*a*-curve is of interest and the crack extension is a large fraction of the ligament length, the *J*-values should be corrected for crack growth. The *J* evaluation at a certain point *n* with actual crack length a_n and ligament length b_n follows the procedure described in Section 2.3.1 and is calculated as the sum of the elastic and plastic components of the *J*-integral. To account for the crack growth, Eq. (2.9) changes to:

$$J_{pln} = \left[J_{pln-1} + \frac{\eta_{n-1}}{b_{n-1} B} \left(A_{pln} - A_{pln-1} \right) \right] \times \left[1 - \frac{\gamma_{n-1}}{b_{n-1}} \left(a_n - a_{n-1} \right) \right]. \tag{2.12}$$

Equation 2.12 is valid for several specimen geometries. The parameter γ, which accounts for crack extension, is dependent of the specimen type and is given by

$$\gamma_{n-1} = \left[-1 + \eta_{n-1} - \left(\frac{b_{n-1}}{W} \frac{\eta'_{n-1}}{\eta_{n-1}} \right) \right], \tag{2.13}$$

for the SENT specimen, with

$$\eta'_{n-1} = W \left. \frac{d\eta}{da} \right|_{n-1}. \tag{2.14}$$

Of the presented fracture mechanics test methods the *J*–Δ*a*-curve determination using the multiple specimen method and the single specimen method with the direct current potential drop technique are used in this work. Depending on the amount of crack extension J_{pl} is either calculated with or

without crack growth correction. The applied method is explicitly stated for every experiment.

3

THE CONFIGURATIONAL FORCES CONCEPT

3.1 Preface

In this chapter a brief introduction to the concept of configurational forces should be given. For general information on the topic of configurational forces the reader is referred to the books by Maugin [47], Gurtin [48] and Kienzler and Herrmann [49]. Two separate force systems are considered here: One, describing the response of a body to deformation is treated by standard deformational forces acting in the current configuration. The second force system acts in the reference configuration and is denominated configurational forces. Configurational forces were first used by Eshelby to study the driving forces on lattice defects [50]. Later the Eshelbian material forces approach was used to describe fracture, e.g. by Maugin [51,52], Maugin and Trimarco [53], Gurtin and Podio-Guidugli [54].

Crack growth, although always associated with deformations around the crack tip, cannot be described by classic deformational forces as it resembles a movement of the crack tip from one material point to another in the reference configuration. This movement in the reference configuration necessitates the description of the thermodynamic driving force on the crack tip using the configurational forces concept. Consequently the two force systems have separate balance laws.

3.2 The crack-driving force in inhomogeneous bodies

This chapter is based on the works of Simha et al. [55] and Kolednik et al. [56], where the influence of an inhomogeneity on the crack driving force is described shortly using the configurational forces concept. The detailed fundamentals and derivations of the given equations are presented in the works by Simha et al. [57,58]. For the further considerations heat transfer and inertia are ignored and the deformational forces are not treated in the current configuration, which would result in the Cauchy stresses, but in the reference configuration resulting in the Piola-Kirchhoff stresses.

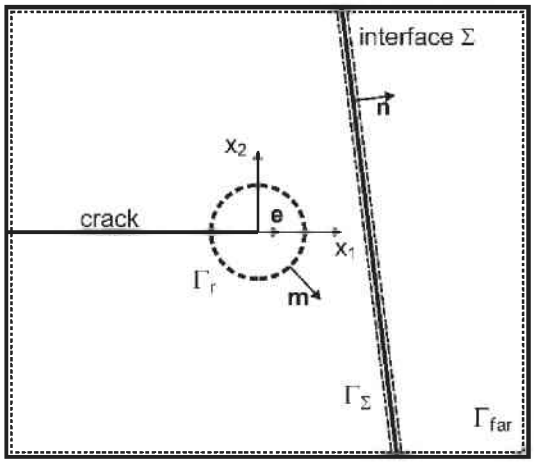

Fig. 3.1 Crack in a two-dimensional bimaterial body containing a sharp interface [56].

A two-dimensional body with a crack and a single, sharp interface Σ is shown in Fig. 3.1. At the interface the material properties exhibit a jump. The bulk configurational stress **C** is defined as,

$$\mathbf{C} = \phi\mathbf{I} - \mathbf{F}^{\mathrm{T}}\mathbf{S} \,, \tag{3.1}$$

where ϕ is the strain energy density, see Eq. (2.3), **I** is the identity tensor, **F** is the deformation gradient and **S** is the 1st Piola-Kirchhoff stress. The configurational stress **C** is identical to Eshelby's energy momentum tensor. The configurational body force **f** is the negative divergence $\nabla\cdot$ of **C**,

$$\mathbf{f} = -\nabla \cdot \mathbf{C} = -\nabla \cdot \left(\phi\mathbf{I} - \mathbf{F}^{\mathrm{T}}\mathbf{S}\right). \tag{3.2}$$

The parameter $\mathbf{F}^{\mathrm{T}}$ is the transposed of the deformation gradient. The configurational force acting on the crack tip $\mathbf{f}_{\mathrm{tip}}$ is given by

$$\mathbf{f}_{\mathrm{tip}} = -\lim_{r\to 0}\int_{\Gamma_r}\left(\phi\mathbf{I} - \mathbf{F}^{\mathrm{T}}\mathbf{S}\right)\mathbf{m}\,\mathrm{d}l \,, \tag{3.3}$$

with **m** as the unit normal to a circle Γ_r centered at the crack tip. The component of $\mathbf{f}_{\mathrm{tip}}$ in crack growth direction is equivalent to

$$J_{\mathrm{tip}} = \mathbf{e}\cdot\left(-\mathbf{f}_{\mathrm{tip}}\right) = \mathbf{e}\cdot\lim_{r\to 0}\int_{\Gamma_r}\left(\phi\mathbf{I} - \mathbf{F}^{\mathrm{T}}\mathbf{S}\right)\mathbf{m}\,\mathrm{d}l \,. \tag{3.4}$$

with **e** as the unit vector in crack growth direction. The right side of Eq. (3.4) is Rice's *J*-integral, describing the crack driving force near the crack tip J_{tip}.
Along the interface Σ the configurational force $\mathbf{f}_\Sigma$ is

$$\mathbf{f}_{\Sigma} = -\left([[\phi]]\mathbf{I} - [[\mathbf{F}^{\mathrm{T}}]]\cdot\langle\mathbf{S}\rangle\right)\mathbf{n}, \tag{3.5}$$

where the vector n is the unit normal to Σ. The jump of a quantity at Σ is designated [[]], e.g. $[[\mathbf{S}]] = \mathbf{S}^{+} - \mathbf{S}^{-}$; the average of this quantity across Σ is designated $\langle\ \rangle$, e.g. $\langle\mathbf{S}\rangle = (\mathbf{S}^{+} + \mathbf{S}^{-})/2$. All the configurational forces along the interface $\mathbf{f}_{\Sigma}$ contribute to the crack driving force by a scalar term C_{inh}

$$C_{\mathrm{inh}} = -\mathbf{e}\cdot\int_{\Sigma}\left([[\phi]]\mathbf{I} - [[\mathbf{F}^{\mathrm{T}}]]\cdot\langle\mathbf{S}\rangle\right)\mathrm{n}\,\mathrm{dl}, \tag{3.6}$$

which is denominated material inhomogeneity term. The integral in Eq. (3.8) gives the sum over all configurational forces at the interface, $\mathbf{f}_{\Sigma}$, and represents them in vector form. The material inhomogeneity term is the projection of this vector in the crack growth direction represented by the unit vector **e** and corresponds to the negative crack driving force term of the interface.

The far-field *J*-integral J_{far} is the crack driving force induced by the applied load into the body; it can be obtained by the summation over all configurational forces in the body, including $\mathbf{f}_{\mathrm{tip}}$ acting on the crack tip along the external boundary of the body Γ_{far} [59]. For an elastic body with a crack, a sharp interface and homogeneous materials on either side of the interface, the configurational force $\mathbf{f} = 0$, everywhere in the body, except at the crack tip and the interface, where $\mathbf{f}_{\mathrm{tip}}$ and $\mathbf{f}_{\Sigma}$ act.

Besides the direct evaluation of J_{tip} in Eq. (3.4) can also be calculated as the sum of the applied far-field *J*-integral J_{far} and the material inhomogeneity term C_{inh} in both scalar and vector form,

$$J_{\mathrm{tip}} = J_{\mathrm{far}} + C_{\mathrm{inh}} \tag{3.7}$$

and

$$\mathbf{J}_{\mathrm{tip}} = \mathbf{J}_{\mathrm{far}} + \mathbf{C}_{\mathrm{inh}}\ . \tag{3.8}$$

If $C_{\mathrm{inh}} = 0$, which is the case for a homogeneous material, the *J*-integral is path independent and $J_{\mathrm{tip}} = J_{\mathrm{far}}$. Several numerical studies show that for crack propagation from a material with lower Young's modulus or yield strength to one with higher Young's modulus or yield strength C_{inh} is negative and thus the driving force on the crack tip is smaller than the applied far-field crack driving force [57]. This is the explanation for the shielding effect encountered for compliant/stiff or soft/hard transitions described in Section 1.2.2. In the opposite case, for a stiff/compliant or hard/soft transition, C_{inh} is positive and $J_{\mathrm{tip}} > J_{\mathrm{far}}$, which explains the anti-shielding effect. In the next chapter a qualitative

explanation for the occurrence of the shielding and anti-shielding effects is given.

Concludingly it should be mentioned that the configurational forces concept has the advantage that it is a general concept, free from restricting assumptions concerning the material behavior and the type and spatial distribution of the inhomogeneities.

3.3 An intuitive explanation of the material inhomogeneity effect

With the explanations for the material inhomogeneity effect in Section 3.2 being rather abstract and complex, an intuitive explanation for the effect should be given here. This energy-based explanation was already outlined in [57] and presented in detail in Kolednik et al. [16] and is only repeated here.

First, a crack in a loaded homogeneous elastic body is assumed. A certain strain energy ϕ, is stored in the crack tip field due to the loading. If linear elastic fracture mechanics is valid, the strain energy is only depending on the applied stress intensity factor K and the Young's modulus E. Thus, ϕ can be calculated for a point with polar coordinates (r, Θ), with respect to the crack tip, see Fig. 3.2a. For an increment of crack extension Δa the strain energy of the point does not change; the complete crack driving force has to be provided by the applied loading.

Now a bimaterial body with a crack and a sharp interface is assumed where a jump from a high Young's modulus E_S to a low Young's modulus E_C occurs (see Fig. 3.2b), which is denominated stiff/compliant transition. Before crack extension the strain energy density ϕ_S is stored at the point (r, Θ). If, upon crack extension, the point crosses the interface, the stored strain energy density changes to ϕ_C with $\phi_S > \phi_C$. The energy difference $\phi_S - \phi_C$ is not needed for moving the crack tip field and becomes available for crack extension, thus increasing the crack driving force. This corresponds to the anti-shielding effect described for the stiff/compliant transition. The crack tip field is likely to change size and form due to the interface, which is ignored here.

For a compliant/stiff transition (Fig. 3.2c) where the point crosses an interface from a material with low to one with high Young's modulus, the strain energy of the point increases. Therefore, an additional amount of energy $\phi_S - \phi_C$ is needed for the movement of the crack tip field, which is not available for extending the crack; the crack driving force is decreased. In this case, the interface shields the crack tip.

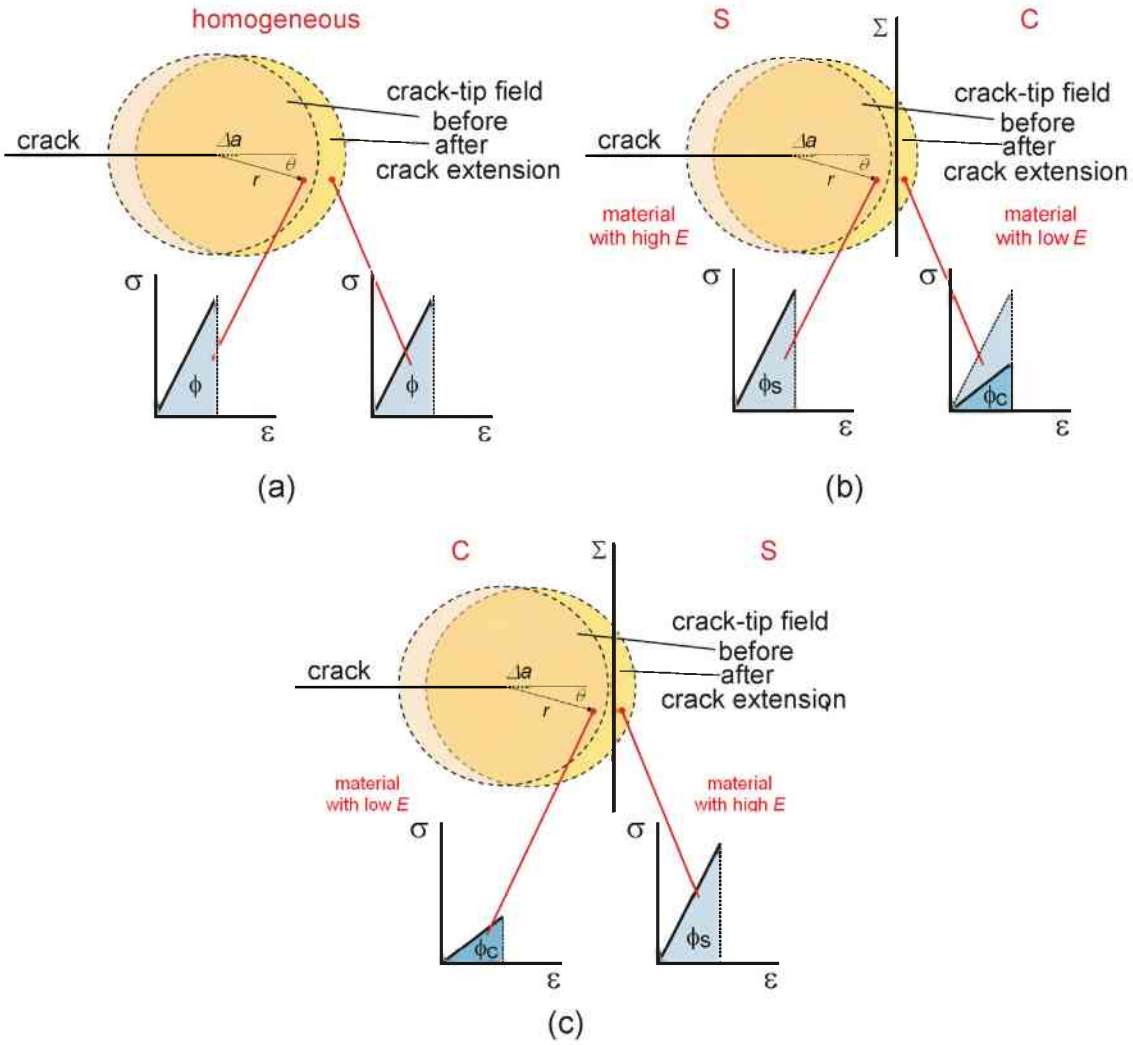

Fig. 3.2 (a) Crack tip field in a homogeneous material with the strain energy density ϕ at point (r, Θ). Crack perpendicular to a bimaterial interface for a (b) stiff/compliant (S/C) and (c) compliant/stiff transition. [16]

Numerical case studies by Simha et al. [60] have shown that the local crack driving force J_{tip} approaches infinity close to the interface for a stiff/compliant transition and zero for a compliant/stiff transition.

The effect can be explained similarly if the constituents of the bimaterial have the same Young's modulus but different yield strength. For crack growth from the hard constituent, i.e. the one with the higher yield strength, towards the soft, i.e. the one with the lower yield strength, an anti-shielding effect is found. In the opposite case, a transition soft/hard, shielding occurs.

3.4 The crack driving force in structures with compliant interlayers

For a crack growing from a stiff material towards a compliant interlayer a combination of the two transitions discussed above occurs. First the crack experiences an anti-shielding effect when it approaches the compliant interlayer. After growing into the interlayer the crack driving force is reduced due to the shielding effect of the compliant/stiff transition.

Kolednik et al. [16] conducted finite element analysis on a composite resembling the structure of a deep-sea glass sponge, with a periodical variation of the Young's modulus, see Fig. 3.3a. The stiff layers in the deep-sea sponge consist of bioglass with a Young's modulus of 42 GPa. The compliant phase is a protein with a Young's modulus of 1 GPa. The Young's moduli have been determined by Woesz et al. [61] by nanoindentation measurements on the layered microstructure of the deep-sea sponge Monorhaphis chuni. The stiff and compliant layers of the modeled composite have thicknesses of 5 µm and 0.1 µm, respectively. The interfaces between the layers are modeled as perfect, i.e. no delamination can occur. In modeling the composite is loaded by applying a global strain of 1 % and the local driving force acting on the crack tip in the composite J_{tip} is numerically evaluated.

Fig. 3.3b shows the variation of J_{tip} plotted versus the crack length in the vicinity of an interlayer. The variation of the Young's modulus is plotted as a blue line. In homogeneous bioglass J_{tip} increases linearly with increasing crack length, which is additionally plotted in Fig. 3.3b. In the vicinity of the interlayer, J_{tip} of the composite increases much stronger than that of homogeneous bioglass due to the strong anti-shielding effect exerted by the interlayer. This is detrimental to the fracture resistance, as the anti-shielding effect promotes crack growth initiation. Inside the interlayer the crack driving force decreases precipitously to nearly zero, which causes the crack to arrest in the interlayer after fracture of the stiff layer. Due to the low J_{tip} inside the interlayer, the crack cannot grow into the next stiff layer. Thus a new crack has to initiate in the stiff material, which becomes the controlling step for fracture and leads to an increase in the fracture resistance of the structure, as initiation of crack growth consumes more energy than crack propagation.

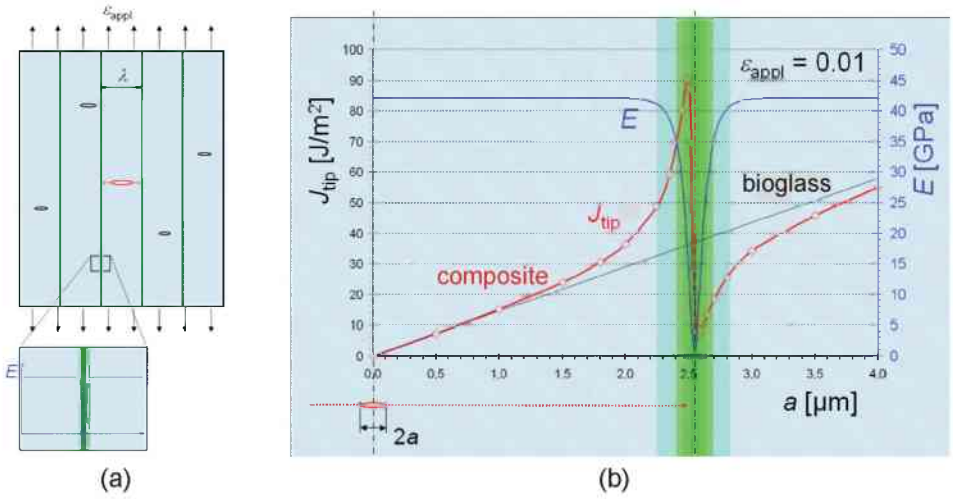

Fig. 3.3 (a) Layered structure with Young's modulus variation and several short cracks. (b) The variation of the driving force acting on the crack tip J_{tip} with crack length. [16]

3.5 Optimizing the material inhomogeneity effect

According to [57], for an elastic inhomogeneity the material inhomogeneity term from Eq. (3.8) can be roughly estimated by

$$C_{inh} \approx \Psi(L,h)\frac{E_C - E_S}{E_C + E_S} J_{far}\,, \tag{3.11}$$

where the parameter Ψ depends on the distance from the crack tip to the interface L, and the geometry of the configuration, accounted for by the height h.

It is assumed that $E_C < E_S$ and the crack grows from the compliant to the stiff phase. The fraction term in Eq. (3.11) characterizes the relative jump of the elastic properties at the interface and is known as Dundurs parameter [62].

The maximum material inhomogeneity term resulting from the Young's modulus inhomogeneity is achieved if the Dundurs parameter is –1. The nanoindentation measurements on the layered microstructure of the deep-sea sponge by Woesz et al. [61] gave a Young's modulus of 42 GPa for the bio-glass and one of 1 GPa for the compliant protein. Inserting these values into the Dundurs parameter in Eq. (3.11) yields a value of –0.95, being very close to –1 and explaining the extremely damage resistant behavior of the sponge.

A similar effect was also analytically described by Kolednik [63] and numerically verified in [57] for bimaterials with a yield stress inhomogeneity. Also in this case, the material inhomogeneity effect increases with an increase in the property jump at the interface. The results of [57] and [63] are able to qualitatively explain the experimental findings in [24,25].

The material inhomogeneity effect, both for elastic and yield stress inhomogeneities, is also influencing fatigue crack growth. The local crack driving force J_{tip} calculated according to Eq. (3.9), influenced by C_{inh}, can be converted into a local stress intensity range acting on a crack tip, which was shown by Kolednik et al. in [64] and is explained in Appendix I. Consequently, the shielding and anti-shielding effects exerted by the interface on the crack driving force also amplify or decrease the stress intensity range.

One of the main goals of this work was to produce and study damage resistant multilayer materials, i.e. with a high jump of the mechanical properties at the interface. Thereafter, these materials are investigated with respect to their fracture and fatigue behavior. In the following section, the materials used for multilayer construction are introduced and the multilayer production is explained.

4

MATERIALS & MULTILAYER CONSTRUCTION

4.1 Introduction

To experimentally investigate the material inhomogeneity effect and its influence on the fracture and fatigue behavior of layered composites, multilayer structures with different types of inhomogeneities are produced. Two elastically inhomogeneous multilayers and one with a yield strength inhomogeneity are considered. As the load bearing capacity of the structures decreases with increasing volume fraction of the compliant or soft phase, it is sought to only introduce a low amount of the mechanically weaker phase.

The multilayers considered are either based on commercial printing paper or the high strength aluminum alloy Al7075-T6. Stacks of the commercial printing paper, separated by air, which acts as the compliant phase, are investigated as a model multilayer with Young's modulus inhomogeneity. For the experiments using AL7075-T6, the aluminum alloy is either bonded with a thermoplastic adhesive to form a multilayer with Young's modulus inhomogeneity, or with technically pure aluminum Al1050, resulting in a structure with a yield strength inhomogeneity. Prior to multilayer construction, the mechanical properties of all constituents are determined. Fracture mechanics tests are conducted on the base materials to allow a comparison with the results of the multilayer tests.

4.2 Materials

4.2.1 Printing paper

The paper used has a grammage of 250 g/m², a sheet thickness of 0.25 mm, and is provided in sheets of DIN-A4 dimensions. The mechanical properties are determined in tensile tests in longitudinal and transverse direction of the material, as paper is highly anisotropic. Five double shoulder specimens with the dimensions and shape given in Fig. 4.1 are tested for each orientation using a Zwick tensile testing machine with a 1 kN load cell and an attached video extensometer for elongation measurement. The testing speed is 0.8 mm/min. Fig. 4.2 shows the stress–strain-curves for both orientations. The

mechanical properties, Young's modulus E, 0.1% proof stress $R_{p0.1}$, ultimate tensile strength R_m and elongation to fracture ε_f, are given in Table 4.1.

The description of paper fracture using fracture mechanics is complicated by the formation of a large process zone in front of the crack tip, which inhibits crack length measurement. Two new techniques have been developed to determine the crack growth resistance curve of paper, which are described in detail in Section 5.2. For the fracture mechanics testing of paper clamped single edge notched tension (SENT) specimens and double edge notch tension (DENT) specimens are used, see Publication A.

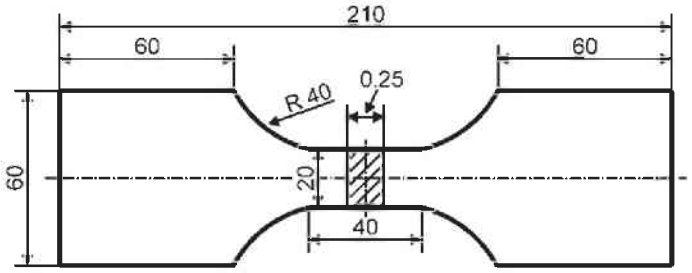

Fig. 4.1 Tensile test specimen for paper testing.

Table 4.1 Mechanical properties of the printing paper.

	E [GPa]	$R_{p0.1}$ [MPa]	R_m [MPa]	ε_f [%]
Longitudinal Direction	4.45	20.1 ± 1.4	48.9 ± 1.9	2.5 ± 0.2
Transverse Direction	2.42	10 ± 0.5	25.8 ± 2.1	6.5 ± 0.2

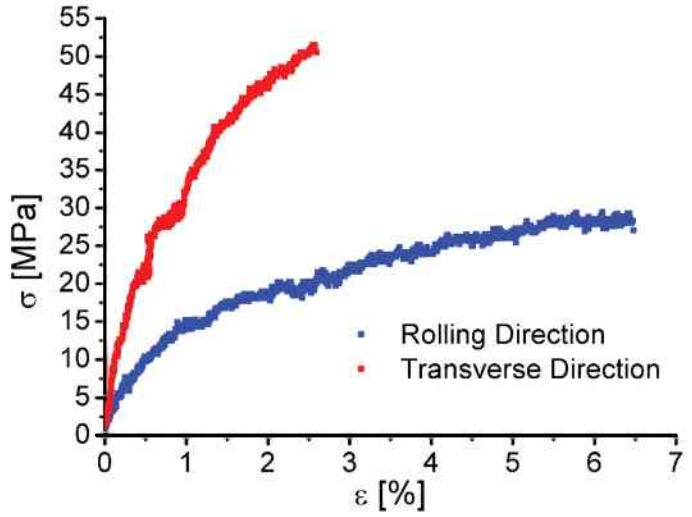

Fig. 4.2 Engineering stress–strain-curves of the commercial printing paper.

4.2.2 Aluminum alloy Al7075-T6

High strength Al7075-T6 served as the stiff or hard component in the multilayers. The chemical composition, according to ASTM B209-07 [65], of the alloy is given in Table 4.2. The material is provided in sheets of 2.3 x 1.8 m² with a thickness t = 3.18 mm (1/8"). Tensile tests are conducted in the rolling and transverse direction of the sheets. Specimens of type H according to DIN 50125, see Fig. 4.4, are used for the testing. The tests are conducted at the Materials Center Leoben Forschung GmbH on a Zwick/Roell Z250 tensile testing machine with a 250 kN load cell and a laser speckle extensometer for displacement measurement. The engineering stress–strain-curves and the mechanical properties for the two directions are shown in Fig. 4.3 and, Table 4.3 respectively. Additionally, the microhardness of the Al7075-T6 sheets is measured with a Buehler® Micromet 5104 microhardness tester with a load of 100 g. A hardness of 175.3 ± 2 HV is measured.

Table 4.2 Chemical composition of Al7075-T6 in mass percent.

Si	Fr	Cu	Mn	Mg	Cr	Zn	Al
0.40	0.50	1.2-2.0	0.3	2.1-2.9	0.18-0.28	5.1-6.1	remainder

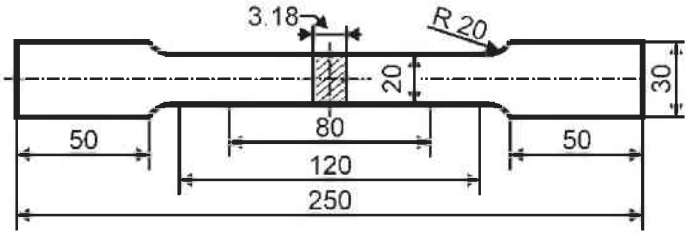

Fig. 4.3 Tensile test specimen type H, DIN 50125:2009-07.

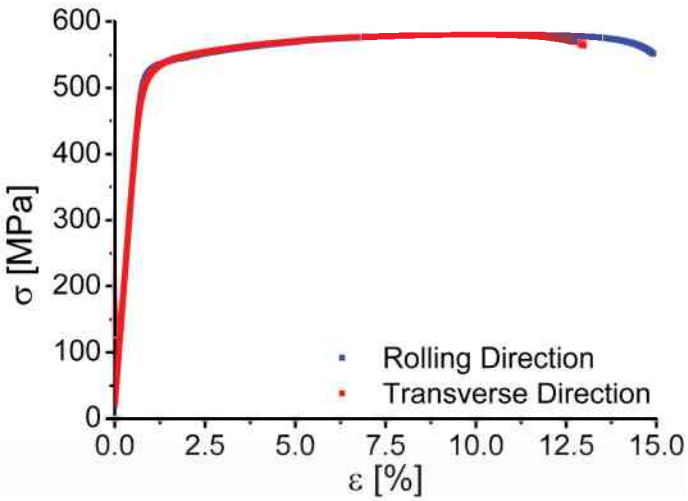

Fig. 4.4 Engineering stress–strain-curves of Al7075-T6.

Table 4.3 Mechanical properties of Al7075-T6

	E [GPa]	$R_{p0.2}$ [MPa]	R_m [MPa]	ε_f [%]
Rolling Direction	69.2 ± 0.1	520.7 ± 1.2	579.3 ± 1.2	13.9 ± 0.3
Transverse Direction	70.2 ± 0.4	518.3 ± 3.86	585.7 ± 4.0	12.4 ± 0.6

Fracture mechanics experiments to determine the crack growth resistance curve in terms of the J-integral of the alloy sheets are carried out using pin-loaded SENT specimens of width W = 20 mm. The specimen geometry is shown in Fig. 4.3. Before testing the specimens are pre-fatigued to an initial crack length of $a_0 = 0.5W$. The testing is conducted according to ASTM E1820-08 [39] and the J-integral evaluation procedure for SENT specimens as described in Section 2.3 using the multiple specimen technique. The resulting crack growth resistance curve of the test is shown in Fig. 4.6. A fracture initiation toughness of J_{IC} = 8 kJ/m² is determined for Al7075-T6, which corresponds to a K_{JC} value of 25 MPa√m.

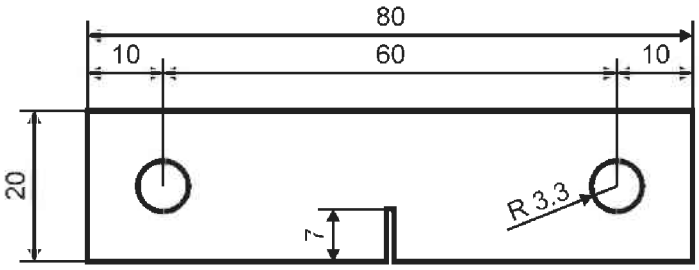

Fig. 4.5 Pin-loaded SENT geometry used for J-integral testing of Al7075-T6.

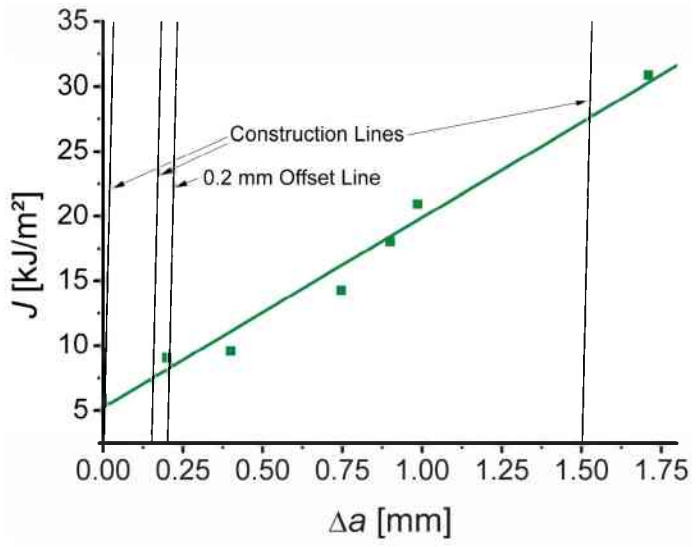

Fig. 4.6 Crack growth resistance curve of Al7075-T6.

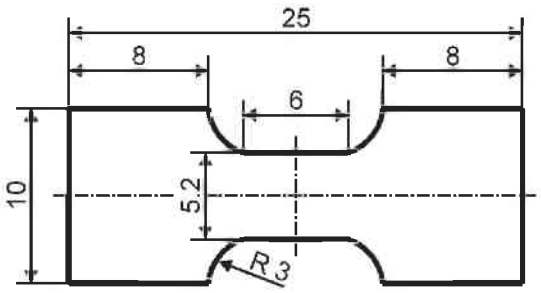

Fig. 4.7 Tensile test specimen used for SS315 and Al1050 testing.

4.2.3 Weld-On SS315

Weld-On® SS315 is the trade name of the two-component methacrylate adhesive used as compliant interlayer in the elastically inhomogeneous multilayer based on Al7075-T6. The adhesive is provided in pre-measured 50 ml cartridges, dispensing the adhesive in the proper 10:1 adhesive to activator mix ratio needed for curing. At room temperature the working time of the adhesive after dispensing is 15 min, 80% of the maximum strength R_m are achieved after 90 min. The maximum strength is reached after approximately 24 h, depending on the glue thickness.

Double shoulder tensile test specimens with dimensions given in Fig. 4.7 are cut with a razorblade from 0.1 mm thick adhesive films. The tensile tests are conducted on a Kammrath and Weiss tensile testing machine with a 200 N load cell at a rate of 0.6 mm/min. Due to the formation of cracks at defects introduced during specimen cutting the determination of stress–strain-curves is inhibited. Therefore, the mechanical properties of the polymer are taken from the technical data sheet of the producer and given in Table 4.4.

Table 4.4 Mechanical properties of SS315.

E [GPa]	R_m [MPa]	ε_f [%]
0.24 ± 0.3	15	100

4.2.4 Al1050

The material for the soft interlayers in the multilayers with yield strength inhomogeneity is technically pure aluminum with a minimum Al content of 99.5 mass percent. The aluminum is provided as sheets of 0.4 x 0.2 m² with a thickness of 0.3 mm. Tensile tests are conducted on seven double-shoulder specimens with outer dimensions shown in Fig. 4.7. The tests are conducted with the same tensile testing equipment and parameters used in Section 4.2.3.

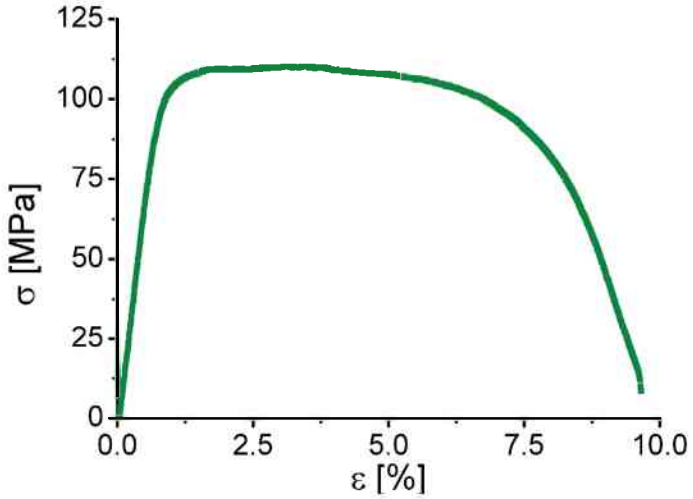

Fig. 4.8 Engineering stress–strain-curve of Al1050

The engineering stress–strain-curve for the material is given in Fig. 4.8 and the mechanical properties in Table 4.5. The Young's modulus of Al1050 is taken from Herzberg [15]. The hardness of the sheets is determined with the microhardness tester described in Section 0 and a load of 25 g. The pure aluminum has a hardness of 32.1 ± 1.5 HV.

Table 4.5 Mechanical properties of Al1050

E [GPa]	$R_{p0.2}$ [MPa]	R_m [MPa]
70	105 ± 3.4	115 ± 4.2

4.3 Multilayer Construction

4.3.1 Multilayers with elastic inhomogeneity 1: Paper multilayers

The idea behind the paper multilayer system is to construct a model structure with a material inhomogeneity effect that is as high as possible. The multilayer consists of paper sheets which are separated by air. Assuming that air has a Young's modulus of zero and inserting $E_c = 0$ in Eq. 3.11 in Section 3.5 gives a Dundurs parameter $(E_c - E_s)/(E_c + E_s) = -1$, which corresponds to the highest possible material inhomogeneity effect for an elastically inhomogeneous multilayer.

DIN A4 paper sheets of thickness t are stacked and glued together at the ends, where they are clamped during testing, with a special paper glue (Planatol BB®).

For the CD configuration multilayers with thickness $B = 5t$, width $W = 60$ mm, total specimen length $L_0 = 180$ mm, length between the clamps $L_1 = 70$ mm and gauge length $H_0 = 40$ mm are constructed, see Fig. 4.9a.

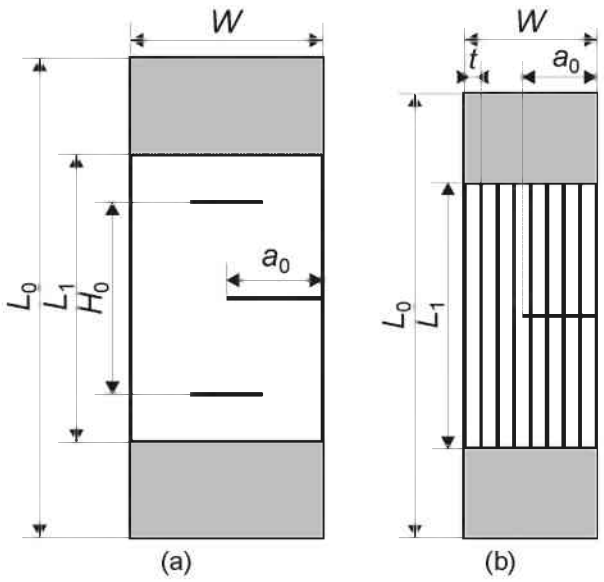

Fig. 4.9 Specimen geometries of the paper multilayers in (a) crack divider and (b) crack arrester configuration.

In CA configuration 32 sheets are glued together giving $W = 32t$. For these specimens B = 10 mm, L_0 = 180 mm and $L_1 = H_0$ = 90 mm, see Fig. 4.9b.

During fracture mechanics testing the specimens are clamped in the glued areas, shown in grey in Fig. 4.9. Notches up to approximately half the specimen width, $a_0 = 0.5W$ are introduced into the multilayers in both configurations using a razorblade. Details on the specimen preparation are also given in Publication B.

The fracture mechanics tests are conducted on a Zwick tensile testing machine with a 1 kN load cell, a video extensometer for displacement measurement and a testing speed of 0.8 mm/s.

4.3.2 Multilayer with elastic inhomogeneity 2: Al7075/Adhesive

The second multilayer system with an elastic inhomogeneity is composed of Al7075-T6 and Weld-on® SS-315. Inserting the Young's moduli fromTable 4.3 and Table 4.4 into Eq. 3.11, Section 3.5, gives a Dundurs parameter of −0.99, which should result in a very strong material inhomogeneity effect.

From the 2.3 x 0.8 m² sheets, samples with the shape and dimensions given in Fig. 4.10 are laser-cut. The multilayers consist of five aluminum layers connected with four adhesive layers of 0.1 mm nominal thickness. This results in volume fractions of 2% polymer and 98% Al7075-T6. Before bonding the aluminum samples are degreased using ethanol. The adhesive is dispensed on one side of the sheets, which are thereafter pressed together for 2h to allow the adhesive to cure.

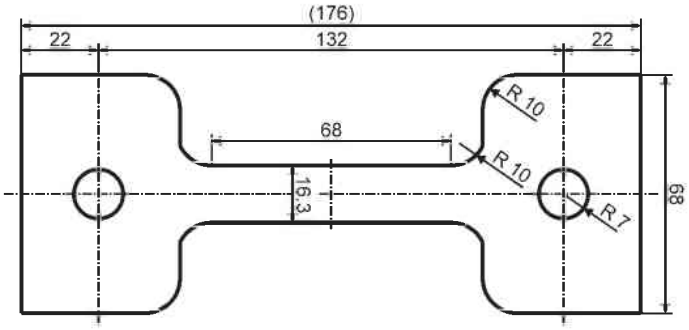

Fig. 4.10 Geometry of the laser-cut Al7075-T6 sheets.

Fig. 4.11 Photograph of the Al7075/Adhesive multilayer.

Before further machining, the adhesive is given an additional 24 h curing time to reach maximum strength. The multilayers have a total thickness of 16.3 mm, which gives an average adhesive layer thickness of 0.1 mm. A photograph of a polished cross section of a multilayer is shown in Fig. 4.11, the dark adhesive layers are clearly visible.

Fracture mechanics testing

For fracture mechanics testing the multilayers are notched depending on the desired configuration, see Fig. 4.12a and Fig. 4.12b for photographs of the CA and CD configuration, respectively. The specimens in both configurations have a quadratic cross section in the reduced area, where $W = B = 16.3$ mm. Before fracture mechanics testing, an apparatus with a razorblade and 1 µm diamond paste are used to introduce a sharp notch at the tip of the machined one. Subsequently the samples are pre-fatigued according to [38] to an initial crack length $a_0 = 0.5W$.

Fracture mechanics testing in both configurations is carried out on a Zwick tensile testing machine with a 100 kN load cell at a loading rate of 0.8 mm/min. The load line displacement is measured using a video extensometer and a clip gauge. In CA configuration the tests are stopped regularly to take digital photographs of the specimens with a digital camera attached to the crosshead of the tensile testing machine. An average of 120 photographs is taken during each test.

(a)

(b)

Fig. 4.12 Al7075/Adhesive fracture mechanics testing specimens in the (a) crack arrester and (b) crack divider configuration.

In CD configuration single specimen tests are conducted by measuring the crack extension in one Al7075-T6 layer using the potential drop technique described in Section 2.3.1. This technique is not applicable in CA configuration due to the insulating adhesive layers in front of the crack tip. Therefore, the point of crack growth initiation is taken as the point where a first load drop is observed in the load−displacement-curve and further crack extension is measured from the digital photographs.

Fatigue testing

One specimen in CA configuration with the same dimensions as the fracture mechanics samples is subjected to a fatigue test. The test is conducted on a Schenk servo-hydraulic testing machine with a 60 kN load cell at a frequency of 10 Hz. The crack length is measured on one specimen side during the test with a long-distance OLYMPUS BXFM optical microscope, attached directly to the testing machine. Furthermore pictures are taken during the test with a CANON digital camera attached to the microscope. The test is conducted at a constant applied stress intensity range ΔK = 9 MPa$\sqrt{m}$ and a stress ratio R = 0.1. Therefore the test is stopped regularly, approximately 20 times, to measure the crack length and to adjust the applied loads.

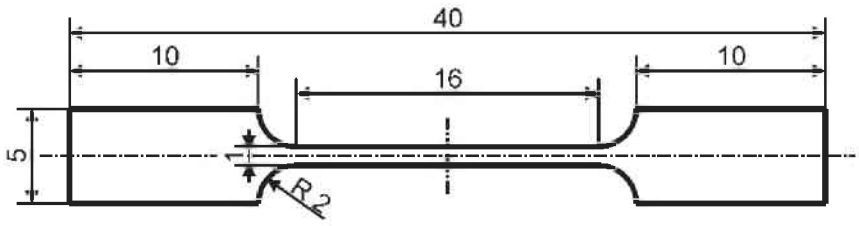

Fig. 4.13 Fatigue test specimen for the Al7075/Adhesive and Al7075/1050 multilayers.

An additional specimen with the outer dimensions given in Fig. 4.13 and width W = 5 mm, composed of two aluminum layers bonded with a 0.1 mm adhesive layer is also fabricated for fatigue testing in CA configuration. A 1 mm notch is introduced into the specimen with a wire saw. The notch is sharpened using the apparatus to introduce a razorblade cut described above. The fatigue test is carried out with the same parameters and equipment as the above mentioned one. For testing, the shoulders of the specimen are clamped in holders, which are pin-loaded during testing.

4.4 Multilayer with yield strength inhomogeneity: Al7075/Al1050

4.4.1 Techniques for metal/metal laminate construction

The hard/soft multilayers are based on Al7075-T6 with thin interlayers of Al1050. Both aluminum grades have the same Young's modulus, resulting in a Dundurs parameter of zero, but a factor five difference in the yield strength, compare Table 4.3 and Table 4.5. To investigate the material inhomogeneity effect it is advantageous to achieve thin, straight interfaces with good bond strength. Various techniques are available to create metal/metal laminates, e.g. diffusion bonding, explosion cladding or roll bonding. These techniques are described in detail in the books by Schrader [66] and Groover [67].

Diffusion bonding

The advantage of diffusion bonding is that straight interfaces with good bond strength are formed, which generally are very thin, i.e. the chemical and mechanical properties exhibit a sharp jump between the materials. Nevertheless, diffusion bonding of aluminum alloys is complicated due the presence of the dense and temperature stable alumina layer forming on the metal surface, which inhibits the diffusion of metal atoms through the interface and makes it an unattractive method for aluminum joining. In general, bonding of aluminum alloys necessitates the application of reactive metallic interlayers and the use of high temperature pressing under vacuum conditions [68].

Explosion cladding

The interfaces generated by explosion cladding are generally also very thin and exhibit good strength, but due to the shock wave propagating through the materials a wavy interface morphology forms, which is disadvantageous for studying the material inhomogeneity effect.

Roll-bonding

Roll-bonding is another widely used technique to join metal sheets. In roll-bonding two or more metal sheets are passed between rolls, which apply a pressure high enough to join the sheets. A schematic of the roll-bonding process is given in Fig. 4.14. If external heat is applied, the process is called hot roll-bonding, otherwise cold roll-bonding. Due to the applied pressure and high plastic deformations during rolling, oxide layers on the surface are fractured and bare metal surfaces are generated, which can bond together. In cold roll-bonding a minimum thickness reduction of approximately 60% is necessary in the first rolling pass to achieve bonding. In hot roll-bonding this critical reduction can be reduced significantly and the forces to achieve bonding are lower than for cold roll-bonding.

The quality of the surfaces to be joined has a strong influence on the bonding strength; therefore a thorough cleaning of the components before rolling is necessary.

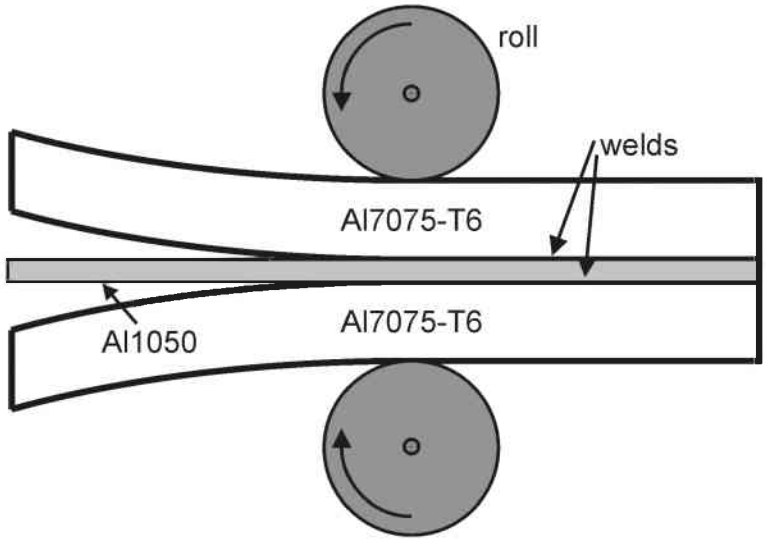

Fig. 4.14 Schematic of the roll-bonding process.

4.4.2 Al7075/Al1050 laminate fabrication

Due to the generally good interface properties and the possibility to easily change the thickness of the single layers by changing the distance between the rolls, hot roll-bonding is used for the production of the hard/soft multilayers. A two-high reversing mill with a roll diameter of 260 mm is used for the roll bonding at the Erich Schmid Institute. To reduce the forces necessary to achieve bonding, roll-bonding is carried out at 480 °C, which corresponds to the solutionising temperature of Al7075.

The Al7075-T6 and Al1050 are cut into sheets of 200 x 70 mm² and degreased with acetone and ethanol. To remove the alumina layer from the metal surface, the Al7075-T6 sheets are brushed with a steel brush directly before stacking the layers. The cold deformation introduced by the brushing also forms a hard surface layer, which increases the bond strength of the roll-bonded material as described by Kim et al. [69]. Stacks of alternating Al7075-T6 and Al1050 layers are built directly after brushing.

To prevent sliding of the single layers relative to each other during rolling, the stacks must be connected. The most widely used methods to fix the layers in the stack are welding and the use of rivets. Rolling tests are conducted with stacks that are joined by tungsten inert gas welding, but the strength of the welding joint is not sufficient to prevent the stacks from sliding and falling apart. This is due to the generally bad fusion weldability of Al7075 caused by the high copper and zinc contents of the alloy. In a next step, aluminum and iron rivets are used for bonding the stack. At the elevated temperature where roll-bonding is conducted, the strength of the rivets is not sufficient to bond the stack and the rivets fracture, see Fig. 4.15. Such an opening of the stack is called alligatoring. The iron rivets do not fracture upon rolling, but the difference in the deformability of iron and aluminum at 480 °C leads to the formation of cracks originating at the rivets, which inhibit the bonding of the aluminum layers. Fig. 4.16 shows a cross section of a stack bonded with iron rivets after rolling. Copper rivets are found to be able to maintain the integrity of the stack during rolling, but are also deformable enough not to cause cracking between the aluminum layers. Therefore, copper rivets are applied for the roll-bonding of the hard/soft multilayer.

Before roll-bonding, the brushed and jointed stacks are annealed at 480 °C for 30 min. In the first rolling pass the thickness is reduced by approximately 30% and between 10% and 20% in all following passes. Every two passes the stacks are reheated at 480 °C for 10 min. Depending on the initial and final multilayer thickness between 5 and 12 rolling steps are carried out.

Fig. 4.15 Alligatored Al7075/Al1050 stack for roll bonding. The fractured aluminum rivets are clearly visible.

(a) (b)

Fig. 4.16 Al7075/Al1050 stack connected with iron rivets after roll bonding. Cracks formed at the interface rivet/aluminum inhibiting bonding.

After roll-bonding the multilayer structures underwent a T6 heat treatment according to ASTM B-918-01 [70]. The heat treatment is composed of 90 min solutionising at 480 °C followed by quenching in water and a two step precipitation heat treatment for 4h at 120 °C and 8h at 160 °C.

4.4.3 Al7075/Al1050 multilayers for fracture mechanics and fatigue testing

For the fracture mechanics and fatigue tests, a multilayer system consisting of four hard Al7075-T6 layers and three soft Al1050 layers is used. The stack is rolled from an initial thickness of 13.6 mm to a final thickness of 5 mm in 5 passes, which corresponds to a true strain of one. The average thicknesses of the hard Al7075-T6 and soft Al1050 layers are 1.17 mm and 0.11 mm, respectively, which results in a composition of approximately 93% Al7075-T6 and 7% Al1050. A metallographic section of the multilayer is shown in Fig. 4.17,

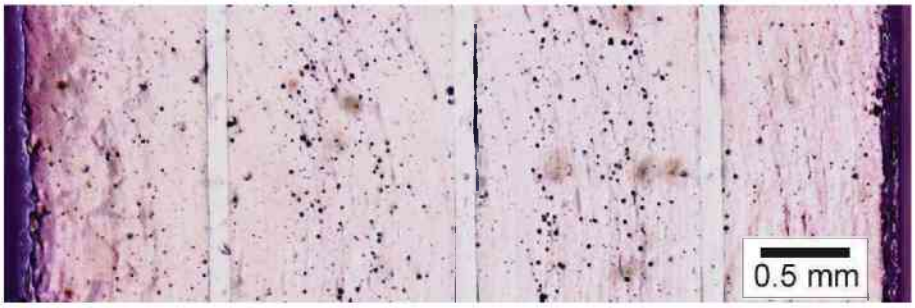

Fig. 4.17 Metallographic section of the roll-bonded Al7075/Al1050 multilayer.

where the Al1050 interlayers are clearly visible as white lines. The thin interfaces are generally very straight and the interlayer thickness is constant. After roll bonding and the T6 heat treatment, the microhardness of the single layers is measured with the equipment and loads described in Section 0. Hardness values of 177.8 ± 3 HV are measured for Al7075 and 28.4 ± 3 HV for Al1050. This is in good agreement with the values measured for the constituents before roll-bonding and shows that by the T6 heat treatment the same mechanical properties as before are achieved after roll-bonding.

Fracture mechanics testing

For fracture mechanics testing pin-loaded SENT specimens with W = 5 mm and outer dimensions given in Fig. 4.18 are used. A notch is introduced into the specimens using a wire saw, which is subsequently sharpened with a razorblade. Two specimens with different notch length are prepared this way. Specimen 1 is pre-fatigued in compression before the fracture mechanics tests using a RUMUL resonant testing machine at a frequency of 108 Hz. The initial crack length is a_0 = 3.46 mm after pre-fatiguing. The tip of the razorblade cut in Specimen 2 is at a_0 = 1.87 mm.

Testing is conducted on a Kammrath and Weiss tensile testing machine with a 10 kN load cell and an inductive displacement transducer at a speed of 0.6 mm/min. Photographs of one specimen side are taken during testing using a OLYMPUS digital camera mounted on a OLYMPUS SZX16 stereomicroscope.

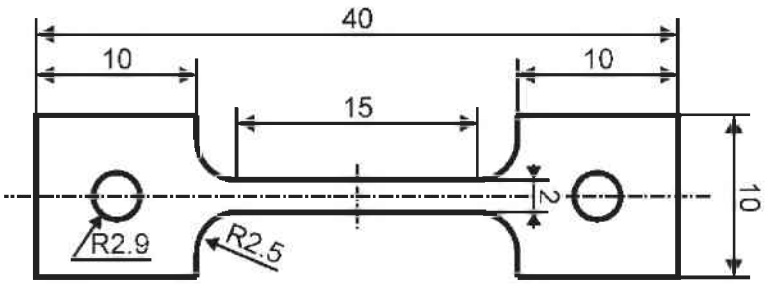

Fig. 4.18 Pin-loaded SENT specimen used for fracture mechanics testing of the hard/soft multilayers

Fatigue testing

For fatigue testing specimens with W = 5 mm and the outer dimensions given in Fig. 4.13 are machined. A photograph of a specimen is shown in Fig. 4.19. The test equipment and setup are the same as described for the fatigue tests conducted on the Al7075/SS315 multilayers described in Section 4.3.2. Tests are conducted at constant applied stress intensity ranges of ΔK = 9, 12 and 18 MPa$\sqrt{m}$. Additional tests are conducted at ΔK = 5 MPa$\sqrt{m}$ on an INSTRON servo-hydraulic testing machine with a 50 kN load cell, but otherwise identical test setup. Crack growth is monitored on both specimen sides using an Olympus BXFM long-distance optical microscope. Additionally images of the specimens are taken at several points of the tests with a Zeiss Leo 440 scanning electron microscope (SEM). To allow a distinction between the two constituents and improve the visibility of the interfaces, the specimens are prepared using a two step electrolytic etching process before testing. After etching, the specimens are cleaned in an ultrasonic cleaner in distilled water and ethanol to remove residues of the etchant and inhibit a corrosion influence on the subsequent tests.

Fig. 4.19 Notched and etched Al7075/Al1050 fatigue specimen with 4 hard and 3 soft layers.

5

FRACTURE OF INHOMOGENEOUS MATERIALS

5.1 Preface

The results of the fracture mechanics investigations on inhomogeneous materials, which represent the main part of the experimental work, are presented and discussed in this chapter. The conducted work can be divided into two topics: The first topic treats the development of two new methods for the fracture resistance determination of thin short fiber composites. This topic has originated during the investigation of the multilayered specimens made of paper, which is, in essence, a short fiber composite. Somewhat surprisingly, it has been found that it is not easy and not at all state of the art to determine the crack growth resistance of this type of material. The second topic investigates the fracture behavior of multilayered structures with respect to their ability to act as damage tolerant materials.

5.2 Fracture resistance of thin short fiber composites

To evaluate the effect the multilayer build-up described in Section 4.3.1 has on the fracture behavior of paper, it is essential to determine the crack growth resistance curve of the base material. Paper is a special case of a short fiber composite, consisting only of short cellulose fibers connected directly to each other, without a surrounding matrix [71]

To determine the crack growth resistance according to the ASTM standard [39], as described in Section 2.3, it is necessary to determine the *J*-integral and the crack extension Δa. The *J*-integral evaluation from the load-displacement records of the fracture mechanics test is standardized and poses no problem. However, the crack extension measurement in paper is complicated, as neither the single, nor the multiple specimen technique are applicable. Optical crack length measurement is impossible due to the large damage zone forming in front of the crack tip, where fiber fracture, bridging and pull-out occur.

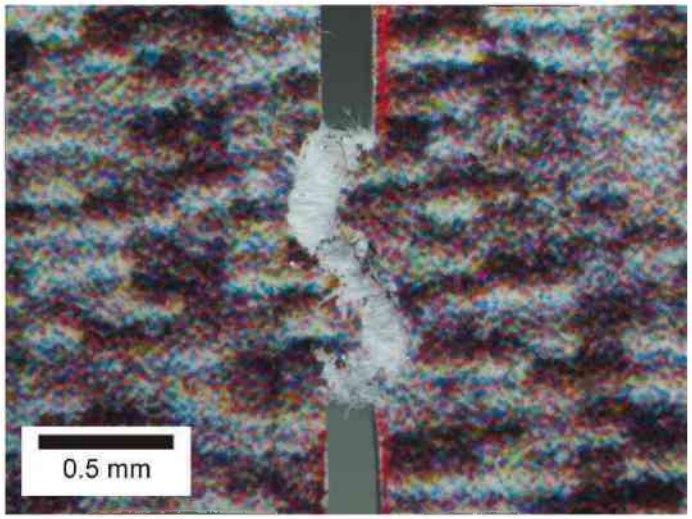

Fig. 5.1 LM-micrograph of the damage zone forming in a double edge notch tension specimen.

Fig. 5.1 shows a light-optical microscope (LM) micrograph, where the damage zone forming between the razorblade notches in a double edge notch tension specimen is clearly visible. Although the damage zone extends through the complete initial ligament length, the load bearing capacity of the specimen is still 20% of the maximum load. Also the single specimen techniques, see Section 2.3.1, cannot be applied, as paper is insulating and the unloading compliance method does not yield satisfactory results.

Are there other possibilities to measure crack extension in paper to be able to evaluate a crack growth resistance curve? This was the main question and problem treated in Publication A. This question is not only important for paper, but for many kinds of short fiber composites, e.g. polymer composites or concrete reinforced with short glass-fibers, where similar problems occur.

A literature survey on the work conducted in the field of fracture mechanics of paper is given in Publication A. Numerous studies applying different techniques to characterize fracture, including linear elastic fracture mechanics, elastic-plastic fracture mechanics, the essential work of fracture criterion and cohesive zone modeling, have been published to describe paper fracture. None of them is able to determine the crack growth resistance curve, as the point of crack growth initiation and further crack extension cannot be monitored.

In Publication A two new methods to determine the crack length in short fiber composites are proposed and applied to the printing paper:

In the first method, deeply-notched double edge notch tension (DENT) specimens are tested in-situ under an optical microscope with an attached digital camera. The DENT specimen with the short ligament length has the advantage that in the ligament area between the crack tips a constant strain and stress field forms. Therefore, it is possible to determine the stresses in the

ligament area by simply dividing the applied load by the cross-sectional ligament area. This leads to two distinct advantages of this specimen geometry: The first is that the fracture initiation toughness can be determined directly from the load−displacement-curve, without further knowledge about crack growth. The second is that from the applied load and the crack flank separation, which can be determined from the images taken during the test, the cohesive zone relation can be determined experimentally. The cohesive zone relation, together with the mechanical properties given in Table 4.1 allow the modeling of fracture mechanics tests of paper specimens in arbitrary geometries, and consequentially the evaluation of a crack growth resistance curve.

The second method uses local deformation analysis (LDA) to determine the crack length. In-situ tests are conducted on single edge notch tension specimens (SENT) under an optical microscope. Digital photographs taken during the tests are processed using LDA to determine the local strains around the crack tip. A critical strain is defined were the local load bearing capacity decreases to zero. If the local strains exceed this critical strain, the material is looked at as locally fractured. This allows the determination of the actual crack length using LDA.

The results of the methods are compared and a good agreement is found for the fracture initiation toughness values and the crack growth resistance curves of the different specimen geometries. This is especially important as it indicates that the determined results are independent of the tested geometry, which allows the transfer of the achieved results to other geometries.

Publication A

Determining the fracture resistance of thin sheet fiber composites - Paper as a model material

Johannes Zechner, Marian Janko and Otmar Kolednik

published in

Composites Science and Technology, 2013;74:43
http://dx.doi.org/10.1016/j.compscitech.2012.10.007

Abstract

In nonlinear fracture mechanics testing of thin-sheet short-fiber composites, special problems occur that do not appear in other engineering materials, such as steels. The most important problem is the formation of a long process zone, where fiber pull-out, realignment and breakage occur, making an optical crack length measurement impossible. This impedes the determination of a reproducible value of the fracture toughness and the construction of a crack growth resistance curve. Two new approaches are presented to overcome this problem. In the first one, a procedure is presented to determine experimentally the cohesive zone relation on deeply-notched double-edge notch tension specimens. The cohesive zone relation enables us, together with the mechanical properties, to simulate numerically a fracture mechanics test on an arbitrary geometry and to determine a crack growth resistance curve. In the second approach, the displacements and strains around the process zone are measured during in situ experiments under an optical microscope using digital image analysis. With this local deformation analysis, a critical local strain is determined where the load bearing capacity of the material decreases to zero. The knowledge of this critical strain is used to find the location of the crack tip and to determine a crack growth resistance curve. The application of the two approaches is demonstrated on commercial printing paper as model material. It is shown that reproducible fracture toughness parameters can be determined with both procedures.

Keywords: A. Short-fiber composites, B. Fracture toughness, C. Finite element analysis, C. Deformation, Cohesive zone model

1 Introduction

Standardized fracture mechanics experiments are available in order to determine the fracture toughness for various classes of materials and composites. Such experiments are conducted by loading a pre-cracked specimen while observing the extension of the crack. The fracture initiation toughness is determined at the onset of crack growth; in cases where the fracture toughness varies during crack growth, it is useful to determine the crack growth resistance as a function of the crack extension.

For some materials the measurement of the fracture toughness properties is still difficult, especially for thin sheet fiber composites that exhibit a nonlinear stress–strain behavior. The main problem in these materials is the measurement of the crack extension. A nonlinear region appears around the crack tip (plastic zone, see Fig A.1a) so that the onset of crack extension cannot

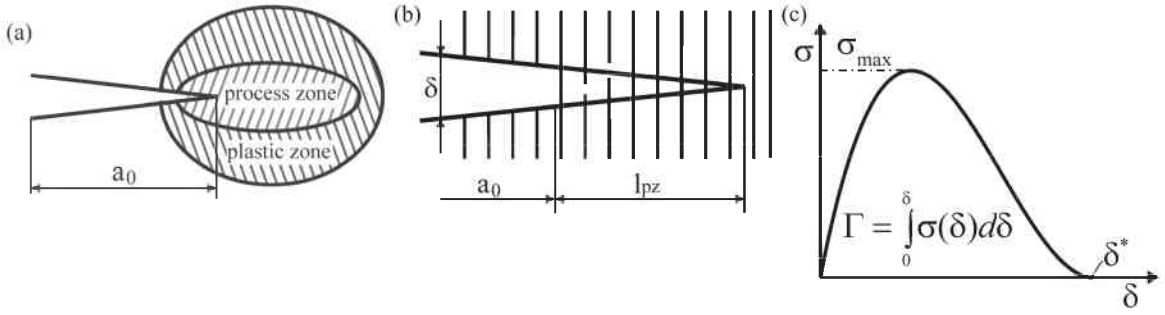

Fig. A.1. Schematics of the location of the process and plastic zone around the crack tip (a), of the process zone in a fiber composite (b) and of a cohesive zone relation (c).

be deduced from the nonlinearity of the load–displacement record. Inside the plastic zone, a process zone of length l_{pz} appears close to the crack tip where the micromechanical processes of crack growth occur, such as the fracture of the matrix material, fiber pull-out and -fracture (Fig A.1b). The behavior of the material within the process zone can be described by the cohesive zone model, i.e. a characteristic curve where the local stress perpendicular to the crack plane is plotted against the local separation δ of the crack flanks, Fig A.1c. Different proposals exist in literature how to define the current position of the crack tip in the process zone (which determines the current crack length) [A.1]. Let us assume, we define the crack tip at the position just behind the last unbroken fiber, where $\delta = \delta^*$ in Fig A.1c. This seems physically appropriate, since no force is transmitted between the upper and lower crack flank behind this position.

A problem now appears, if the process zone becomes very long during the fracture mechanics experiment. Depending on the specimen geometry, the process zone might even extend through the whole unbroken ligament. Paper is an example of a fiber composite where this problem appears. Fig A.2a shows a pre-cracked tensile specimen made of blackened paper where the process zone has extended over three quarters of the initial ligament and the load has dropped to 50% of the maximum load. Nevertheless, even at the initial crack tip region, the fibers have not yet fractured (or are not pulled out completely from the matrix), see Fig A.2b. This means that, according to our definition of the crack tip, the current crack length still equals the initial crack length a_0 and crack growth has not yet been initiated.

This suggests that the position of the crack tip in the process zone should be defined in a different way, but all other definitions are somewhat arbitrary. It is clear that a correct measurement of the fracture initiation toughness or the crack growth resistance is only possible if the current crack length is determined correctly.

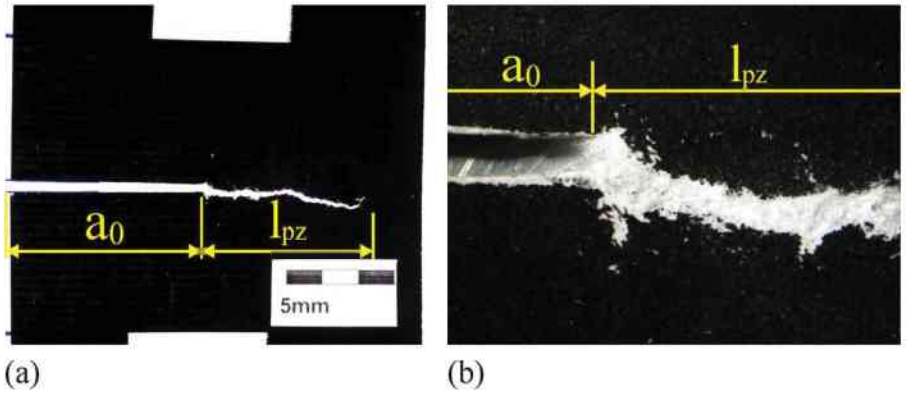

Fig. A.2. (a) Specimen surface of the blackened paper specimen showing the initial crack of length a_0 and the process zone of length l_{pz}, (b) detailed view of the process zone near the initial crack tip.

In the current paper, two different procedures are proposed to overcome this problem and to get reproducible fracture toughness properties of such materials. The first approach is based on the cohesive zone model and, especially, a procedure to experimentally determine the shape of the traction–separation-relation depicted in Fig A.1c. In the second approach, local deformation analysis is used to directly determine the position of the crack tip from the displacement- and strain fields around the crack. The functioning of the two procedures is demonstrated on commercial printing paper. The two approaches are compared and possibilities and limitations are discussed.

The following section presents a short review about fracture mechanics testing of paper.

2 Fracture mechanics testing of paper

The strength of paper is important in many technical applications, especially for the paper industry. As paper fracture is often initiated at pre-existing flaws, e.g. edge cracks introduced by handling, a fracture mechanical characterization is required to predict the behavior [A.2].

First works on the subject used linear elastic fracture mechanics to determine a critical energy release rate [A.2]. This is problematic as most types of paper show pronounced nonlinear behavior in tensile tests [A.2-A.4]. More recent works on the topic applied the essential work of fracture (EWF) method [A.5] and the *J*-integral criterion [A.4,A.6,A.7] to the analysis of paper fracture.

Aim of the EWF concept [A.5,A.8] is to determine the essential work of fracture, i.e. the energy needed to create a unit area of fracture surface, using double edge notch tension (DENT) specimens. The key assumption of the concept is that a circular plastic zone forms between the crack tips of a DENT specimen in plane stress conditions, on the contrary to the process zone that

extends linearly from crack tip to crack tip [A.8]. As the plastic work and the EWF scale differently with the ligament lengths, the testing of specimens with similar dimensions but different ligament length, allows the determination of the EWF.

The *J*-integral is a loading parameter of a crack that can be applied in the regimes of nonlinear and linear elastic fracture mechanics [A.9]. The values of *J* are calculated from the area below the load–displacement record. The *J*-values are plotted versus the crack extension Δa and at a precisely defined point the fracture initiation toughness is determined, denoted as the critical *J*-integral J_c or J_i [A.10-A.12]. The slope of the J–Δa-curve is a measure of the crack growth resistance [A.13]. As discussed above, the problem is the measurement of crack extension in paper. In metallic alloys, indirect methods are often applied to measure crack extension, especially the potential drop technique [A.14], but this method is not applicable to paper or other insulating materials, e.g. most polymers. Also the unloading compliance technique [A.14] does not work well in thin fiber composites.

In [A.7] double edge notch tension (DENT) specimens are tested and a critical *J*-integral J_c is calculated using the single [A.15] and multiple [A.16] specimen methods. In the test method proposed in [A.6], middle cracked tension specimens are used to determine J_c. In both methods J_c is taken as the *J*-value at the maximum load, although it is unclear if crack growth really initiates at this point or not. The disadvantage of this procedure is that the maximum load depends on specimen type (SENT, DENT, etc.), geometry (a_0/W) and size, resulting in a geometry- and size dependent critical *J*-integral. This fact strongly limits the usefulness of such data. The procedure can be only applied for comparative material characterization, if always the same specimen geometries are used.

3 Material and Mechanical Properties

The tested material is a commercially available printing paper with a grammage of 250 g/m² and a sheet thickness of B = 0.25 mm. Tensile tests are conducted on a Zwick tensile testing machine, with an attached video extensometer for displacement measurement, to determine the mechanical properties of the material. The tests are carried out at a constant displacement rate of 0.8 mm/min at approximately 25 °C in ambient air. Double-shoulder tension specimens with a width of 20 mm in the gauge length and 60 mm in the region where the specimens are clamped are used.

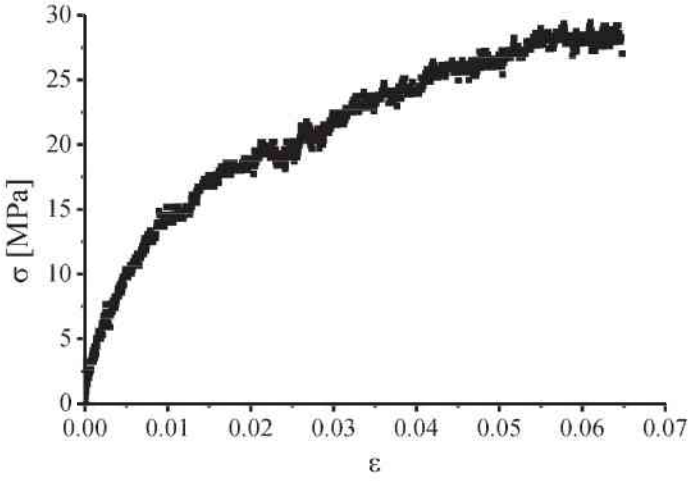

Fig. A.3. True stress vs. true strain curve of the tested paper in transverse direction.

Fig A.3 shows a true stress vs. true strain curve in TD, which corresponds to the direction of all subsequent fracture mechanics tests. From the initial slope of the stress–strain-curve a Young's modulus of E = 2.42 GPa is measured, which is in good accordance with values measured in TD on other paper qualities [A.5].

It should be noted that the material properties of paper are sensitive to both temperature and moisture [A.17] and, in general, the scatter of the data is quite high.

4 The cohesive zone approach

4.1 The cohesive zone model

In other material classes where similar problems are encountered concerning the crack length measurement, e.g. concrete or tough polymers where crazing occurs, the cohesive zone model (CZM) has been applied successfully to characterize the fracture behavior [A.18-A.21]. The CZM, first applied on concrete [A.21], is an expansion of the strip-yield models originally introduced in [A.22,A.23] to describe the plastic zone in front of the crack tip. In the CZM a traction–separation (σ–δ) relation, also called cohesive zone relation (CZR), is defined (Fig A.1c), which fully describes the localized load transfer from damage initiation to final failure in the process zone [A.24-A.26]. The maximum occurring stress in the CZR is denominated cohesive strength (σ_{max}). The area under the traction–separation curve is the cohesive energy Γ, being the energy required to generate a unit area of the crack surfaces, which therefore equals the EWF described in Section 2. The displacement where the traction has decreased to zero is defined as the critical separation δ^*. If, as in our case, the crack tip is assumed at the position just behind the last unbroken

fiber where $\delta = \delta^*$, the critical separation can be understood also as the critical crack tip opening displacement at fracture initiation COD_i [A.11,A.12]. The parameters Γ, σ_{max} and δ^* are termed the characteristic parameters of the CZR [A.20]. They determine the fracture behavior, while the accurate shape of the CZR is mostly considered to be of second order relevance [A.27,A.28]. Various types of CZR are commonly applied for different classes of materials, see e.g. [A.24,A.25]. It is also important to note that the total dissipated energy in a fracture mechanics test is split into the local work of damage and separation within the process zone Γ and the non-reversible energy consumed by deformation of the surrounding material [A.24].

The tensile behavior of commercial printing paper sheets has recently been described using the CZM [A.29,A.30]. There, the softening branch of the stress–elongation-curve of a tensile test (i.e. a specimen without crack) is used to calibrate an exponentially decreasing CZR. Such a calibration is correct only if the material damage is confined to a single zone over the length of the tensile specimen. As this cannot be assured – damage could be initiated at multiple flaws which then would contribute to the total dissipated energy for damage formation – this method is somewhat questionable. Furthermore, in both articles no critical separation is defined for the CZR, which then only allows the description of the damage behavior of the material, but neither that of fracture initiation nor crack growth. The same problem occurs for the description of material fracture using the essential work of fracture concept where only the critical energy for fracture initiation is measured, which alone does not allow predicting crack extension.

An interesting method to experimentally determine the CZR for tough polyethylene is presented in [A.18,A.19]. There, a round circumferential notch is machined into prismatic specimens with a cross section of 16 x 16 mm², which is then sharpened with a razorblade. The final ligament/bulk area ratio is 1:10. These deeply notched tensile specimens are used to determine the CZR. The deep notch assures that the damage zone is confined to the remaining ligament area and that, due to the small ligament area, the displacement along the remaining ligament is approximately constant. Therefore, the separation δ can be measured with a clip gauge directly at the crack flanks and the cohesive stress σ can be calculated by dividing the applied load by the ligament area.

This approach is adapted in the current work for the CZR determination of thin sheet fiber composites by changing the specimen geometry from a thick deeply-notched specimen with a ligament area under plane strain conditions to a thin deeply-notched double edge notch tension (DENT) specimen under plane stress conditions. Hereby the unbroken ligament should be narrow so that damage in the process zone appears simultaneously throughout the whole ligament and the separation along the ligament is constant.

4.2 Experimental determination of the cohesive zone relation

Five DENT specimens with length L_0 = 50 mm, width W = 9 mm and thickness B = 0.25 mm are used for the determination of the CZR of our printing paper. Cracks with initial length $a_0 \approx 4.1$ mm are cut with a razor blade, resulting in a very narrow initial ligament length $b_0 \approx 0.8$ mm. The specimen ends are clamped with a free length between the clamps L = 36 mm. A schematic of the specimen geometry is given in Fig A.4a.

The tests are performed on a Kammrath & Weiss tensile testing device with a 200 N load cell and an inductive displacement transducer recording the crosshead displacement. The displacement rate is 0.6 mm/min. The experiments are carried out in situ under an Olympus SZX16 stereomicroscope with an attached digital camera. Before testing, a_0 and b_0 are determined precisely for each specimen using the stereomicroscope.

Load P and load-line displacement v_{LL} are recorded during the tests, which are stopped at various displacements to take digital photographs of the ligament area. In total 34 photographs are taken during a test. An area of approximately 3.7 mm x 2.8 mm is captured in the pictures with a resolution of 3136 x 2352 pixels. The crack flank separation δ can be measured directly from the digital photographs. A displacement of 1 pixel corresponds to a separation of 1.2 µm.

For all specimens the cohesive stress σ in the ligament area is calculated by dividing the applied load P by the initial ligament area,

$$\sigma = \frac{P}{b_0 B} \qquad \text{(A.1)}$$

The σ–v_{LL}-curves are in good accordance for all tested specimens, and a standard deviation of 3.5% is measured for the cohesive strength σ_{max}. As the crack flank separation measurement from the photographs is rather time consuming, the CZR was determined for only one of the tested specimens, which exhibits an average σ–v_{LL}-curve.

The resulting CZR is plotted in Fig. A.4b. The characteristic parameters of the CZR of our printing paper are: cohesive strength σ_{max}= 34.24 MPa, cohesive energy Γ = 3.82 kJ/m² and critical separation δ^* = 425 µm. It should be mentioned that the correct measurement of δ^* is sensitive to the precision of the load cell and the ability to determine as accurately as possible the point where the load decreases to zero.

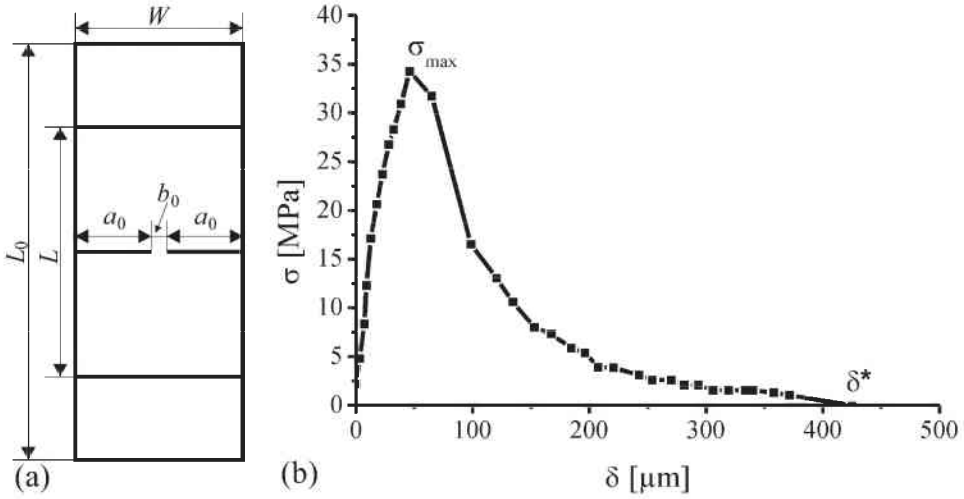

Fig. A.4 (a) Drawing of the DENT with short ligament *b*. (b) The cohesive zone relation determined experimentally from the DENT specimen with $a_0/W = 0.9$.

With the assumption that the CZR and its characteristic parameters are material parameters, i.e. independent of specimen type and geometry, the fracture initiation toughness and the crack growth resistance curve can be computed for arbitrary specimen geometries, see below. It is known that the characteristic parameters of the CZR may depend on the stress triaxiality [A.31,A.32]. The out-of-plane constraint may affect strongly the characteristic parameters, e.g. the cohesive strength near the midsection of a thick specimen is much higher than near the side surfaces [A.12,A.33]. As this paper considers thin specimens only, the out-of-plane constraint influence should be negligible. Also the in-plane constraint, which is for example high in deeply notched DENT specimens and low in middle cracked tension specimens and which decreases for low *a*/*W*-ratio [A.12], might have an influence on the characteristic parameters. However, it is generally assumed that this influence is much weaker [A.25].

The method presented here could also be applied for the experimental CZR determination in other material classes, where inverse techniques are used for the CZR identification, e.g. in fiber-reinforced cement [A.34] or polymer-matrix [A.35] composites.

4.3 Modeling of the crack growth resistance curve

Knowledge of the CZR and the mechanical properties allows the modeling of fracture mechanics tests on specimens or components with arbitrary geometries using the finite element (FE) method. In the current work, the geometry modeled is a single edge notch tension (SENT) specimen with $W = 60$ mm, $a_0 = 30$ mm, $b_0 = W - a_0$, and $L = 70$ mm, see Fig. A.5a. A 2-dimensional

FE-model is generated, consisting of four-node continuum elements in the bulk and four-node cohesive elements along the ligament where the crack extends. Along the upper and lower specimen boundary the displacements are constant in loading (y-) direction and fixed in x-direction. The upper boundary is loaded by prescribing the load-line displacement (v_{LL}). The mesh size is 0.1 mm around the initial crack and along the crack path. The cohesive elements have two integration points per element, resulting in a total of 600 integration points along the ligament. The mesh size increases further away from the crack plane up to 1.6 mm in order to reduce the computation time. The finite element mesh in the vicinity of the crack tip is shown in Fig. A.5b. Plane stress conditions are used. The simulation is performed with the finite element program ABAQUS [A.36].

The material is modeled as elastic-plastic; time-dependent behavior is not taken into account. Input parameters for the FE-modeling are the true stress vs. true strain curve of Fig. A.3 and the CZR of Fig. A.4b. Both curves are fitted piecewise by polynomial functions. The stress–strain-curve is linearly extrapolated to allow for higher strains in the modeling. The FE-modeling gives first a P–v_{LL}-curve and a Δa–v_{LL}-curve of the SENT specimen. The crack growth resistance curve (J–Δa-curve) is generated by evaluating for a given load line displacement v_{LL} the J-integral and plotting it against the corresponding value of the crack extension Δa.

As the J-integral calculation for SENT specimens is not standardized, J-values are calculated from a relation given in [A.37], where the total J-integral is split into an elastic and a plastic part, J_{el} and J_{pl}

$$J = J_{el} + J_{pl} = J_{el} + \frac{\eta_{pl} A_{pl}}{B b_0} \quad . \tag{A.2}$$

The component J_{el} is given by

$$J_{el} = \frac{K^2}{E}, \tag{A.3}$$

with the stress intensity factor K calculated from the load P and the geometry factor $f(a/W)$, see [A.12]:

$$K = \frac{P}{B\sqrt{W}} f\left(\frac{a}{W}\right). \tag{A.4}$$

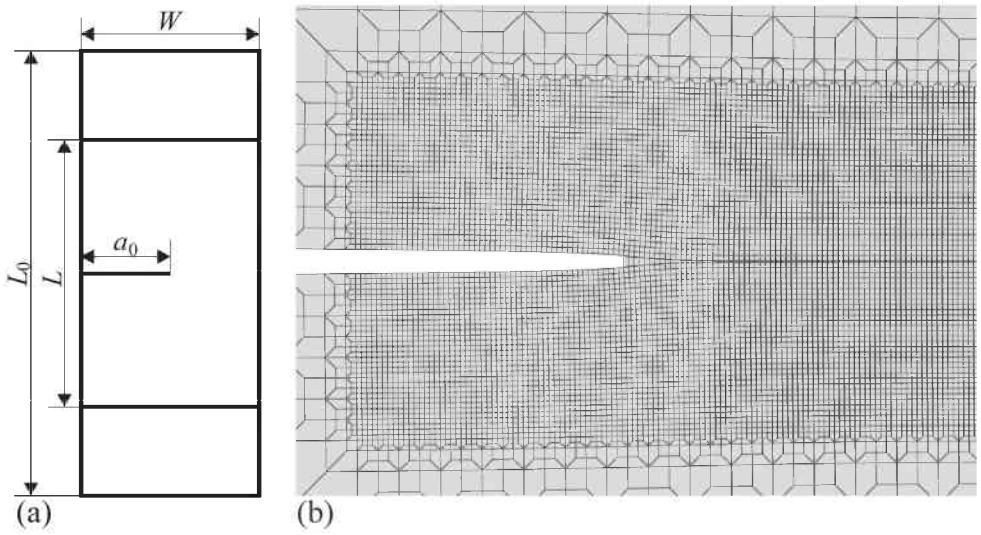

Fig. A.5 (a) Sketch of SENT specimen with W = 60 mm and a_0/W = 0.5. (b) Finite element mesh of the area around the crack tip.

The values of the geometry factor $f(a/W)$ are determined from the data tabulated in [A.37]; for our geometry $f(a/W) \approx 1.27$. In Eq. (A.2), the term A_{pl} is the plastic component of the area below the P–v_{LL}-curve and η_{pl} is a dimensionless parameter depending on the a_0/W-ratio. A corresponding η_{pl} vs. a_0/W curve is plotted in [A.37]; for our geometry $\eta_{pl} = 0.8$.

Fig A.6a shows a comparison between the P–v_{LL}-curve from the modeling with three experimental curves, measured for the same geometry, with the test equipment and parameters described in Section 3. Two of the specimens have been unloaded after a certain v_{LL}; only one is tested to final fracture. The modeled and measured curves agree quite well, but the agreement is, in general better for the rising than the decreasing part of the curve. Note that not a single fit parameter is used in the modeling. The results could be improved further by adjusting the values of the elastic modulus, the extrapolation of the stress–strain-curve for high strains and, especially, the characteristic parameters of the CZR. The determination of an average CZR of more than one specimen would probably improve the agreement of the results, but the functionality of the method is clearly shown.

The computed J–Δa-curve is shown in Fig. A.6b. The J-integral at fracture initiation is J_i = 7.3 kJ/m². A slightly rising J–Δa-curve is observed with increasing crack length.

It might be interesting in this respect to note that, for a given shape of the CZR, an increase of the cohesive energy Γ would enhance both J_i and the slope of the J–Δa-curve, whereas an increase of the cohesive strength would lead to an increase of the slope of the J–Δa-curve but has no influence on J_i, see [A.26].

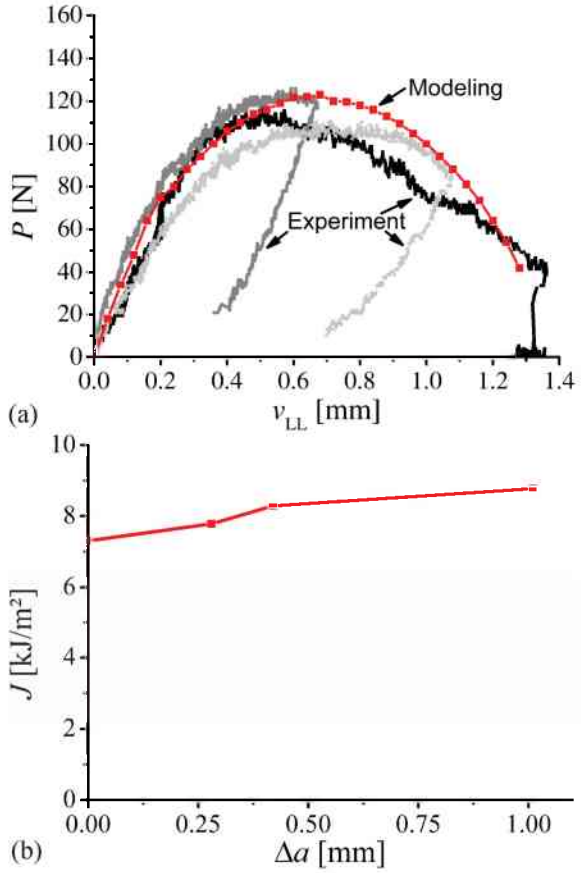

Fig. A.6. SENT specimen with W = 60 mm and a_0/W = 0.5: (a) Comparison between experimental and numerically evaluated load vs. displacement curves; (b) modeled J–Δa-curve. The numerical evaluation relies on the cohesive zone relation depicted in Fig. A.4b.

It should be also noted that finite element modeling using cohesive zones enables the prediction of crack initiation and crack growth also in components without initial crack. In such a case, cohesive elements must be inserted into the FE model on all positions where cracks might initiate or propagate, e.g. near stress concentrations. It is clear that the transferability of the CZR must be fulfilled.

4.4 Evaluation of the fracture initiation toughness J_i

Besides the CZR determination and the subsequent modeling, a fracture initiation toughness value J_i is directly calculated from the P–v_{LL}-record of the DENT specimen with the narrow ligament. Here, J_i is defined as the value of the J-integral at the point where the critical separation δ^* is reached along the ligament. The J-integral is calculated using the formula for the DENT specimen given in [A.15]:

$$J_i = J_{el} + \frac{1}{b_0} \cdot \left[2 \int_0^{v_{pl}} P dv_{pl} - P v_{pl} \right] . \qquad (A.5)$$

The plastic component of the displacement v_{pl} is determined from the P–v_{LL}-curve by subtracting the elastic component of the displacement.

The resulting fracture initiation toughness value is J_i = 7.56 kJ/m², which is about twice the cohesive energy, showing that a considerable amount of energy is consumed in non-reversible processes around the cohesive zone.

5 Application of local deformation analysis

Aim of the second approach is to experimentally determine the crack extension in paper by the use of local deformation analysis (LDA). LDA allows the measurement of the local displacements and strains around the crack tip of a fracture mechanics specimen. A critical local strain ε^{cr} should be identified in front of the initial crack tip at the point where crack extension is initiated. After such a critical strain has been found, the crack extension can be identified by LDA in arbitrary specimens, and the actual crack length in the fracture mechanics experiment can be measured.

5.1 Principles of the local deformation analysis (LDA)

LDA is a technique to determine local strains on the specimen surface from digital pictures taken at different deformation stages during an in situ experiment. Two pictures, one reference picture taken at the unloaded stage and one taken at a certain load, are processed by digital image correlation. A so-called “matching procedure”, described in detail in [A.38], identifies a large number of homologue points in the two photographs. A pair of homologue points, being points in the two pictures corresponding to the same physical point on the specimen, defines a displacement vector for this point. From the displacement field resulting from all measured pairs of homologue points, the in-plane strains can be calculated by numerical derivation of the displacements. For example, when u_x denotes the displacement in loading direction x at the picture coordinates x,y, the strain in loading direction ε_{xx} is given by

$$\varepsilon_{xx}(x,y) = \frac{du_x(x,y)}{dx} \tag{A.6}$$

The matching procedure, the numerical derivation and the accuracy of the procedure are described in more detail in [A.38]. LDA can be applied to analyze the local deformation behavior in tension-, compression- and bend experiments, as well as in fracture mechanics tests. With appropriate loading devices, the experiments can be conducted in the scanning electron microscope, e.g. [A.38,A.39], or under a light microscope.

A pre-condition for the application of LDA is that the specimen surface is structured so that the matching procedure yields a dense array of homologue points. If the specimen surface texture is not appropriate, an artificial surface texture must be generated by depositing a random dot pattern.

5.2 Experimental procedure

Fracture mechanics experiments are conducted on five SENT specimens in situ under the stereomicroscope. The equipment and testing parameters described in Section 4.2 are used. The specimen dimensions are L_0 = 50 mm, L = 40 mm, W = 10 mm, $a_0 \approx$ 5 mm. To enable LDA, a random dot pattern is printed on the surfaces of the specimens using a color laser printer. Digital photographs with a resolution of 3136 x 2352 pixels are taken during the tests. The analyzed area is 9.2 mm x 6.9 mm. About 10^5 pairs of homologue points are found for each image pair.

Fig A.7 shows the P–v_{LL}-record of the in situ test of a SENT specimen with W = 10.05 mm and a_0 = 5.1 mm, which is analyzed in detail using the LDA. All five tests show comparable P–v_{LL}-records and similar damage behavior, but only one specimen, with average behavior, is evaluated in detail due to the very time consuming LDA. A decrease in load is visible at several positions of the curve. This is caused by relaxation of the specimen due to halting the test in order to take the digital photographs. The positions where the pictures for the LDA are taken are marked by triangles. As these pictures are made directly after stopping the tests, no effect of the relaxation on the measured strains is expected.

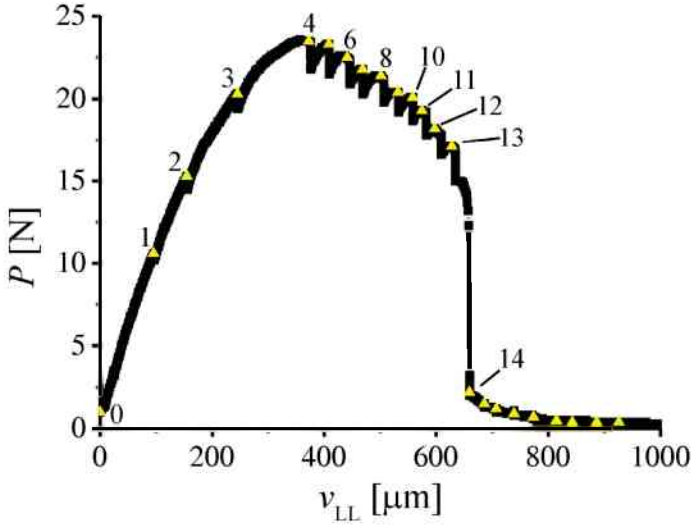

Fig. A.7. Experimental load–displacement-curve of the SENT specimen with W = 10.05 mm.

An example of the LDA is presented in Fig A.8: Fig A.8a depicts homologue points between the undeformed (Point 0) and deformed stage at Point 12 of the P–v_{LL}-curve in Fig A.7. In the area where the process zone is formed the pattern required for the LDA is destroyed due to fiber pull-out, making it impossible for the matching procedure to detect homologue points in this area, see the right image in Fig A. 8a. Fig A. 8b presents the distribution of the local strain in loading direction ε_{xx} along the ligament for Point 12. The strains are very high: ε_{xx} reaches 289% near the initial crack tip without visible crack extension. The local strains determined by LDA depend on the resolution and magnification of the images and the quality of the matching results, e.g. the density of the homologue points [A.38]. Thus, the determined strains, and in consequence the determined critical strains, do not only depend on the material but also on the LDA specifications. Therefore, different magnifications and resolutions in the pictures may lead to different results, which would limit the comparability of LDA results obtained with different parameters.

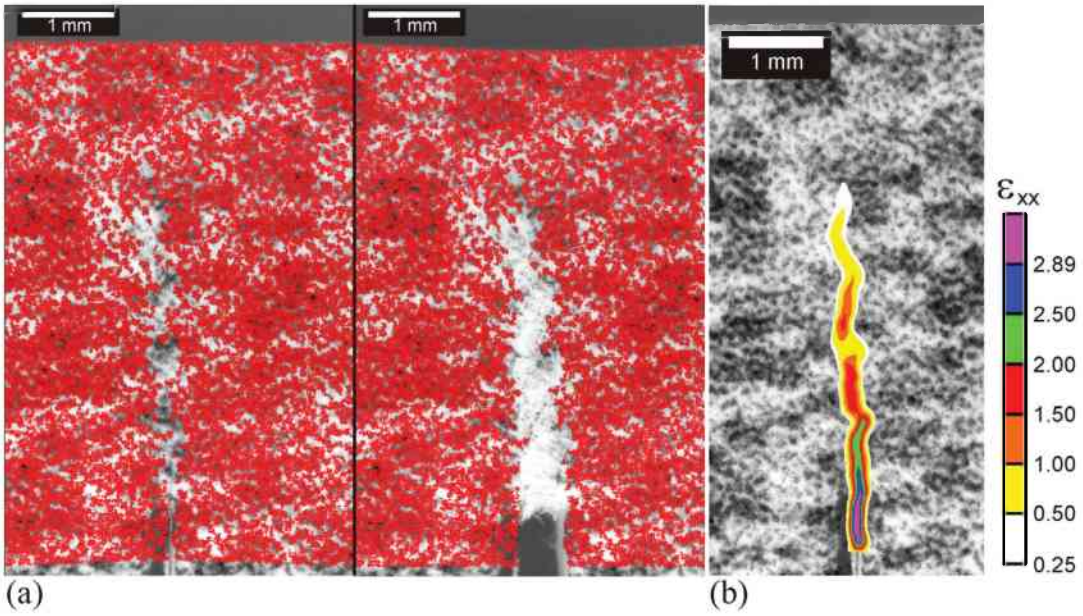

Fig. A.8. SENT specimen with W = 10.05 mm. (a) Homologue points between the undeformed stage (Point 0) and the deformed stage at Point 12 of the P–v_{LL}-curve of Fig. A.7, (b) Distribution of the local strain in loading direction ε_{xx} along the ligament at Point 12.

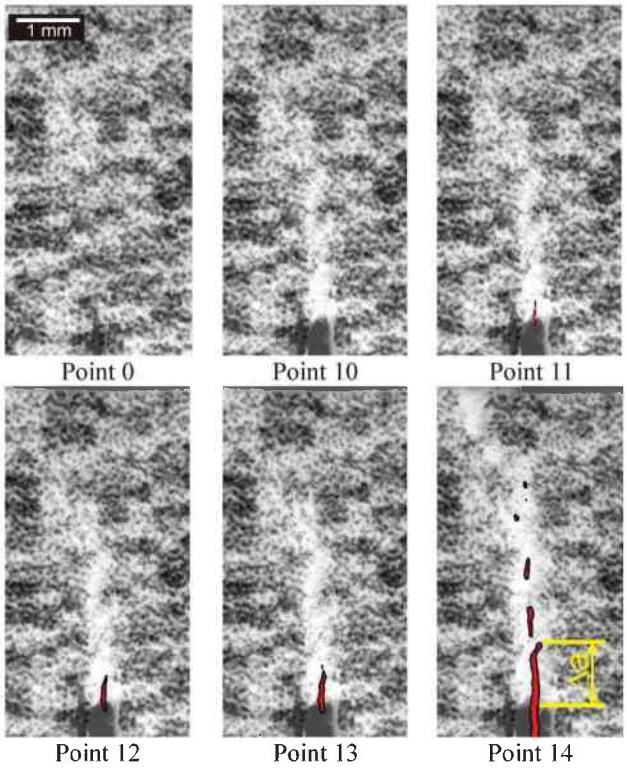

Fig. A.9. SENT specimen with W = 10.05 mm. Photographs of the crack tip regions at different deformation stages corresponding to the halting points marked in Fig. A.7. The regions with local strains equal or higher than the critical strain, ε^{cr} = 2.89, are marked in red.

If we take Point 11 as the critical point where crack growth is initiated, the critical strain equals the measured value of ε_{xx} just in front of the initial crack tip, i.e. ε^{cr} = 2.89. Fig. A.9 presents, for different loading stages, the regions in the paper specimen where the local strain equals or exceeds the critical strain, $\varepsilon_{xx} \geq \varepsilon^{cr}$. These areas are colored red. The location of the actual crack tip at a certain loading stage is taken at the tip of the red area that is still connected to the initial crack tip. In this way, the crack extension Δa can be determined at all the marked halting positions of the P–v_{LL}-curve in Fig A.7.

5.3 J–Δa-curve for different critical strains

In order to plot the J–Δa-curve for the critical strain ε^{cr} = 2.89, the J-integral is evaluated with Eq. (A.4) for all marked halting positions of the P–v_{LL}-curve in Fig A.7. The resulting curve is depicted in Fig A.10a. The J-integral at fracture initiation is J_i = 6.99 kJ/m². The J–Δa-curve slightly increases with increasing crack length.

This procedure can be repeated for other possible values of the critical strain ε^{cr}. For example, if we adopt the proposals of [A.6,A.7] and take the maximum load (near Point 4 of the P–v_{LL}-curve in Fig A.7) as the critical point

where crack growth is initiated, LDA yields a critical strain of ε^{cr} = 1.25. The corresponding J-integral at fracture initiation is now much lower, J_i = 4 kJ/m², but the J–Δa-curve exhibits a much higher slope than in the first case. On the contrary, if crack growth initiation is assumed at Point 13 of the P–v_{LL}-curve, just before the sudden load drop appears, a critical strain of ε^{cr} = 3.40, a fracture initiation toughness of J_i = 7.6 kJ/m² and a very flat J–Δa-curve are determined.

The three possible J–Δa-curves are compared in Fig A.10a. The halting points of the P–v_{LL}-curve are marked in each curve. Two remarks might be useful: (i) For the same point on the P–v_{LL}-record, slightly different J-values are calculated for different critical strains, e.g. Point 14 for ε^{cr} = 2.89 and ε^{cr} = 3.40 in Fig A.10a. The reason is that the elastic component of the J-integral J_{el} is higher for ε^{cr} = 2.89, since the current crack length $a = a_0 + \Delta a$ is larger. (ii) Since crack extension in paper is – as in most technical materials – a discontinuous process when considering it at the microscale [A.40], the J–Δa-curve can be also discontinuous.

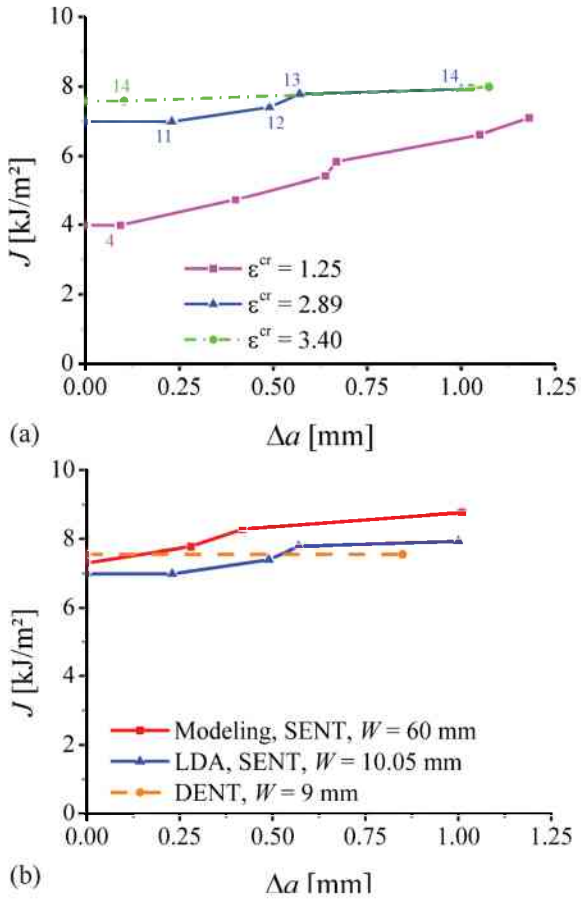

Fig. A.10. (a) The J–Δa-curves for the SENT specimen with W = 10.05 mm determined via LDA for three possible values of the critical strain ε^{cr}. Comparison to the DENT specimen with narrow ligament reveals the correct value, ε^{cr} = 2.89. (b) A comparison of the J–Δa-curves measured and numerically evaluated for different specimen geometries.

This section is concluded by stating that LDA enables the determination of the crack extension Δa, the fracture initiation toughness J_i and the increase of the J–Δa-curve, however, the correct value of critical strain ε^{cr} must be known.

5.4 Determination of the correct critical strain

From the test on the DENT specimen with the narrow ligament, the critical value of the crack tip opening displacement is known to be $COD_i = \delta^* = 425$ µm, see Section 4.2. COD_i characterizes the fracture initiation toughness of the material, similar to J_i, and depends only weakly on specimen type and geometry [A.11, A.12]. The COD- or δ-values of the SENT specimen with $W = 10.05$ mm can be measured on the digital photographs taken at the halting points, see Fig A.7. The COD-values are determined as displacements of the crack flanks just behind the initial crack tip.

COD at maximum load (Point 4 in Fig A.7) is $COD_{(Point\ 4)} = 173$ µm, which is much smaller than the critical COD. At Point 10, $COD_{(Point\ 10)} = 390$ µm, indicating that crack growth has not started yet. A COD of 420 µm measured at Point 11, which is approximately the COD_i, indicates that crack growth initiates at this point. Therefore, $\varepsilon_{cr} = 2.89$, which was determined before for crack growth initiation at Point 11 is the correct value, showing that crack growth does neither start at the maximum load, nor at the occurring load drop.

The correct critical strain ε^{cr} can also be deduced by performing LDA directly on the DENT specimen with the narrow ligament used for the CZR determination. The value of ε^{cr} is measured as the strain along the ligament that occurs at the onset of fracture, i.e. at the point in the CZR where the critical separation δ^* is reached. This yields a critical strain of $\varepsilon^{cr} = 2.80$. The resulting J–Δa-curve is nearly identical to the curve depicted in Fig A.8a for $\varepsilon^{cr} = 2.89$. As stated in Section 5.2, the results of the LDA depend on the magnifications of the photographs; therefore these should not be too different for the comparison of the two specimens. Otherwise the results could be distorted by the LDA.

6 Comparison of the two procedures

The *J-i*ntegral values at fracture initiation J_i of the different specimen geometries are collected in Table A.1. The crack growth resistance curves are compared in Fig A.10b. The average J_i-value is 7.28 kJ/m²; the difference between the results for the tested geometries is smaller than 5%. The results of the two different methods are in good accordance, allowing the assumption that both approaches can be used for the determination of the fracture resistance of

paper. The procedures will be applicable also for other thin sheet fiber composites with a similar fracture behavior.

It is important to notice that two different specimen types and different specimen sizes were tested, and all lead to comparable results. This suggests that the determined J_i-values are transferable, which is essential for the application of these values to other geometries.

This would not be so, for example, if the critical values of the J-integral were taken at the maximum load of each experiment. These J_{Pmax}-values exhibit a very large scatter, see last column in Table A.1.

It might be useful to perform additional experiments, e.g. on SENT specimens with short cracks, before applying the J_i-value to geometries with very low in-plane constraint, or before using the measured CZR or the critical strain of ε^{cr} = 2.80 for the numerical evaluation of the damage evolution in components without sharp cracks. However, since the experiments of the current paper have been conducted on geometries with high in-plane constraint, a transfer of the data to low-constraint geometries is safe. This means that the J_i-value in a specimen with low in-plane constraint will be equal or higher than J_i = 7.28 kJ/m²; it cannot be lower.

Table A.1
J_i-values for the different specimen geometries.

	W [mm]	a_0/W	J_i [kJ/m²]	J_{Pmax} [kJ/m²]
SENT	10.05	0.5	6.99	4.0
DENT	9	0.9	7.56	0.7
SENT (modeled)	60	0.5	7.3	7.3

It has to be mentioned that generally large scatter occurs in paper testing. Therefore, a thorough determination of the crack growth resistance of paper would require the testing of several specimens under a controlled atmosphere.

7 Summary

Standardized fracture mechanics experiments on many thin-sheet short-fiber composites fail, since the measurement of crack extension is impossible. In the present study, methods are proposed to overcome this difficulty. Two procedures for the determination of the crack growth resistance curve are introduced and demonstrated on the example of printing paper. Both procedures are capable of measuring the fracture initiation toughness in terms of the critical J-integral J_i and to record the variation of the crack growth resistance with increasing crack extension Δa.

In the first approach, the cohesive zone relation (CZR) is determined from the fracture mechanics test on a deeply-notched double-edged notched tensile specimen with narrow ligament. The CZR and the material properties measured in tensile tests can be used to numerically evaluate fracture mechanics tests of arbitrary geometries. This has been demonstrated on the example of a large single-edged notched tensile specimen.

The second approach uses local deformation analysis to determine a critical strain ε^{cr} in the damage zone evolving in front of the crack tip, where the load bearing capacity of the material decreases to zero and the material fails locally. The knowledge of this critical strain can be used to find the location of the crack tip and to record a crack growth resistance (J-Δa) curve.

For printing paper with a grammage of 250 g/m^2, a fracture initiation toughness of J_i = 7.28 kJ/m² was measured and a slightly increasing J–Δa-curve was found. The critical strain was ε^{cr} = 289%. The two different approaches yield nearly the same results. The agreement between the results of different specimen types and -geometries is very good, showing that the fracture behavior of the material has been characterized correctly.

Acknowledgements

Financial support by the Austrian Federal Government and the Styrian Provincial Government within the research activities of the K2 Competence Centre “Integrated Research in Materials, Processing and Product Engineering”, under the frame of the Austrian COMET Competence Center Programme, is gratefully acknowledged (Project A4.11 and A4.20).

References

[A.1] Chen CR, Kolednik O, Heerens J, Fischer FD. Engng Fract Mech 2005;72:2072-94.
[A.2] Seth RS, Page DH. J Mater Sci 1974;9:1745-53.
[A.3] Isaksson P, Hägglund R. Engng Fract Mech 2005;72:2299-2315.
[A.4] Westerlind BS, Carlsson LA, Andersson YM. J Mater Sci 1991;26:2630-36.
[A.5] Tanaka A, Yamauchi T. J Mater Sci 2000;35:1827-33.
[A.6] Wellmar P, Fellers C, Delhage L. Nord Pulp Pap Res J 1997;12:189-95.
[A.7] Yuhara T, Kortschot MT. J Mater Sci 1993;28:3571-80.
[A.8] Cotterell B, Reddel JK.. Int J Fracture 1977;13:267-77.
[A.9] Rice JR. J Appl Mech 1968;35:379-86.

[A.10] Standard test method for measurement of fracture toughness. E-1820-08. Annual Book of ASTM Standards, vol. 03.01, ASTM, West Conshohocken, PA, 2008.
[A.11] Kolednik O. Fracture mechanics. In: The Wiley Encyclopedia of Composites, Second Edition, Nicolais L, Borzacchiello A, editors. John Wiley & Sons, 2012. pp. 1126-1141.
[A.12] Anderson TL, Fracture Mechanics: Fundamentals and Applications, Taylor & Francis, 2005.
[A.13] Kolednik O. Engng Fract Mech 1991;38:403-12.
[A.14] Metallic materials – unified method of test for the determination of quasistatic fracture toughness, International Standard ISO 12135:2002(E), ISO, 2002, p. 83-90.
[A.15] Rice JR, Paris PC, Merkle JG. Some further results of *J*-integral analysis and estimates. In: ASTM STP 536, American Society for Testing and Materials, 1973, p. 231-45.
[A.16] Begley JA, Landes JD, The *J*-Integral as a fracture criterion. In: ASTM STP 514, American Society for Testing and Materials, 1972, p. 1-20.
[A.17] Haslach HW. Mech Time-Depend Mater 2008;13:11-35.
[A.18] Pandya KC, Williams JG. Composites 2000;29:439-46.
[A.19] Pandya KC, Ivankovic A, Williams JG. Composites 2000;29:447-52.
[A.20] Janko M, Ecker W, Pinter G, Kolednik O. Macromol Symp 2012;311:1-8.
[A.21] Hillerborg A, Modéer M, Petersson P-E. Cement Concrete Res 1976;6:773-81.
[A.22] Dugdale DS. J Mech Phys Solids 1960;8:100-04.
[A.23] Barenblatt GI. Adv Appl Mech 1962;7:55–129.
[A.24] Elices M, Guinea GV, Gómez J, Planas J. Engng Fract Mech 2002;69:137-63.
[A.25] Brocks W, Cornec A, Scheider I. Computational aspects of nonlinear fracture mechanics. In De Borst R, Mang HA, editors. Comprehensive Structural Integrity, Volume 3: Numerical and Computational Methods. Elsevier, New York, 2003, p. 127–209.
[A.26] Chen CR, Kolednik O, Scheider I, Siegmund T, Tatschl A. Int J Fracture 2003;132:517-36.
[A.27] Tvergaard V, Hutchinson JW. J Mech Phys Solids 1992;40:1377–97.
[A.28] Hutchinson JW, Evans AG. Acta Mater 2000;48:125–35.
[A.29] Mäkelä P, Östlund S. Engng Fract Mech 2012;79:50-60.
[A.30] Tryding J, Gustafsson PJ. Tappi J 2000;83:84-89.
[A.31] Siegmund T, Brocks W. Int J Fracture 1999;99:97–116.
[A.32] Siegmund T, Brocks W. Engng Fract Mech 2000;67:139–54.
[A.33] Chen CR, Kolednik O. Int J Fracture 2005;132:135-52.
[A.34] Shen B, Paulino GH. Cem Conc Compos 2011;33:572-85.

[A.35] Li S, Thouless MD, Waas AM, Schroeder JA, Zavattieri PD. Compos Sci Technol 2005;65:537-49.
[A.36] http://www.3ds.com/products/simulia/portfolio/abaqus/overview/, 14/05/12
[A.37] Cravero S, Ruggieri C. Engng Fract Mech 2007;74:2735-57.
[A.38] Tatschl A, Kolednik O. Mater Sci Engng 2003:A339:265-80.
[A.39] Kapp M, Hebesberger T, Kolednik O. Int J Mater Res 2011;102:687-91.
[A.40] Turner CE, Kolednik O. Fatigue Fract Eng Mater Struct 1994;17:1089-1107.

5.3 Damage resistant multilayer materials

5.3.1 Multilayer with elastic inhomogeneity 1: Paper multilayers

The investigations on the fracture behavior of the paper multilayers in crack divider (CD) and crack arrester (CA) configuration, see Section 4.3.1 for the experimental details, are described in Publication B. The Young's modulus of air, acting as interlayer in the multilayers, is zero, which gives a Dundurs parameter of −1 and should lead to the most pronounced material inhomogeneity effect possible according to Eq. (3.11). The main question sought to be answered in Publication B is: What is the influence this strong material inhomogeneity effect has on the fracture toughness of the multilayers, and what can be learnt from this model system?

Fracture mechanics testing on samples in the crack divider configuration shows that the crack growth resistance curve in this configuration is the same as for the single layer sheets, determined in Publication A. The advantageous behavior of crack divider specimens compared to bulk specimens, explained in Section 1.2.1, is caused by a different prevalent stress state acting in the bulk and layered specimens. In the investigated case, both the single layers and the CD samples have the same thickness and geometry and consequently fracture under the same stress state. Therefore no difference in the crack growth resistance curves can be expected.

The material inhomogeneity effect is supposed to operate and lead to damage resistant behavior in the CA configuration, when the crack tip interacts with the interlayer material. The fracture mechanics tests show that the fracture initiation toughness in the CA configuration is comparable to that of the other configurations, which was expected as the fracture toughness at initiation is a material property and thus independent of the tested geometry and configuration. After fracture initiation the first pre-damaged layer fractures and the crack grows into the interlayer and arrests there. After crack arrest a maximum occurring J-integral J_{max} ten times higher than the fracture initiation toughness is reached. This is caused by the crack arrest, where the triaxiality of the crack tip field is relieved and the remaining ligament deforms like in a tensile test. This is clearly seen in the similarity of stress-strain curves, which were calculated from the load displacement data of the fracture mechanics tests and the tensile test data. An estimation formula is given in Publication B, which allows an estimation of J_{max} from the mechanical properties of the stiff phase and the specimen geometry,

$$J_{max} = \eta L \int_0^{\varepsilon_f} \sigma d\varepsilon \,, \tag{5.1}$$

where η denotes the plastic η-factor used for J-integral calculation. The integral term in Eq. (5.1) calculates the area under the stress–strain-curve determined in the tensile test (Fig. 4.2) and corresponds to the strain energy density. Only the volume of the ligament undergoing inelastic deformation contributes to the increase of J_{max}. This volume is given by $V = Bb_0L$. The length of the deformed volume L in Eq. (5.1), corresponds to the gauge length of the tests in CA configuration for the paper multilayers. The J_{max} value estimated according to Eq. (5.1) is within the scatter band of the experimentally determined J_{max} values, which indicates that the equation makes it possible to give a good estimation of the maximum crack growth toughness.

Finally it can be concluded that the introduction of the interlayers, causes a change in the type of test. The initial fracture mechanics test changes into a tensile test of an unnotched specimen due to the crack arrest, which leads to a highly improved material behavior.

The paper multilayer investigated in Publication B is a model material to show the influence the material inhomogeneity effect has on the fracture behavior. The findings can be transferred to other multilayer materials with compliant interlayers, like the second stiff/compliant multilayered structure described in Section 5.3.2.

Publication B

Paper multilayer with a fracture toughness of steel

Johannes Zechner and Otmar Kolednik

submitted to

Composites Science and Technology

Abstract

We demonstrate in this paper that commercially available printing paper can reach very high fracture toughness, comparable to that of steel, simply due to a special arrangement of the paper sheets with respect to the crack. Fracture mechanics experiments are conducted on single sheets of paper as well as on multilayer specimens in crack divider and crack arrester configuration. It is demonstrated that an arrangement in crack arrester configuration leads to an increase of the fracture toughness by a factor ten. An explanation of the effect is given and the transferability to other materials is discussed.

Keywords: A. Layered structures; B. Fracture toughness; C. Damage tolerance; Material inhomogeneity effect;

1. Introduction

The unique combination of high stiffness, high strength, and high fracture toughness of certain biomaterials, such as the skeleton of the deep-sea sponge Euplectella aspergillum, has been investigated in great detail in the recent years [B.1-B.4]. The microstructure of the sponge consists of a layered structure of brittle silica, i.e. bio-glass, connected by thin protein interlayers. The main reasons for the high fracture toughness of these structures lie in the spatial variation of the material properties between hard silica and soft protein and in the small wavelength of the structure [B.3]. Spatial material property variations may strongly influence the crack driving force, which can be expressed in form of the equation [B.5],

$$J_{\text{tip}} = J_{\text{far}} + C_{\text{inh}} . \qquad \text{(B.1)}$$

In Eq. (B.1), the parameter J_{tip} denotes the crack driving force, measured in terms of the near-tip J-integral, J_{far} is the far-field J-integral, i.e. the driving force that is inserted into the body by the applied forces, and C_{inh} is the so-called "material inhomogeneity term", i.e. the driving force term that is induced due to the material inhomogeneity. If the crack grows from a material with low Young's modulus towards a material with high Young's modulus ("compliant/stiff-transition"), the material inhomogeneity term C_{inh} is negative and J_{tip} becomes smaller than J_{far}; the material inhomogeneity shields the crack tip. This effect occurs in the deep-sea sponge when a crack has grown from the bio-glass into the protein interlayer just before it re-enters the hard bio glass: the material inhomogeneity term is negative and the crack driving force J_{tip} becomes very low so that a very high applied load is necessary for further crack extension [B.3].

It should be noted that not only a spatial variation in Young's modulus produces a material inhomogeneity effect, but also a spatial variation in yield stress [B.5]. It is also important to note that this effect, i.e. the influence of the material inhomogeneity on the crack driving force, is principally different from the effect of interface decohesion on the fracture resistance, which is well known for composite structures [B.6,B.7].

Case studies for linear elastic materials have shown that the material inhomogeneity term near an interface is proportional to the relative jump of the Young's modulus at the interface [B.5,B.8],

$$C_{\text{inh}} = \Psi(L,h)\frac{E_1 - E_2}{E_1 + E_2} J_{\text{far}} . \qquad \text{(B.2)}$$

In Eq. (B.2), the parameters E_1 and E_2 are the Young's moduli left and right of the interface. The non-dimensional parameter Ψ is a function of the distance L between crack tip and interface and the geometry of the configuration, symbolized by the height h.

The consideration of Eq. (B.2) reveals that the "ideal" interlayer material should be air, since with $E_1 = 0$ the relative jump of the Young's modulus becomes -1, and the shielding effect of the material inhomogeneity would be maximized.

Therefore, in the current paper we fabricate model multilayers with air as interlayer material and study the material inhomogeneity effect on specimens with different crack plane configurations. For simplicity, commercial printing paper has been chosen as the hard phase, but the conclusions can be transferred to arbitrary other materials.

2. Experimental Procedures

2.1. Material and tensile tests

The base material for multilayer construction is a commercially available printing paper with a grammage of 250 g/m² and a thickness t = 0.25 mm. The mechanical properties of the material are determined in longitudinal and transverse direction in tensile tests. Five double-shoulder specimens, with a width of 20 mm in the gauge length and 60 mm where the specimens are clamped, are used for the tests.

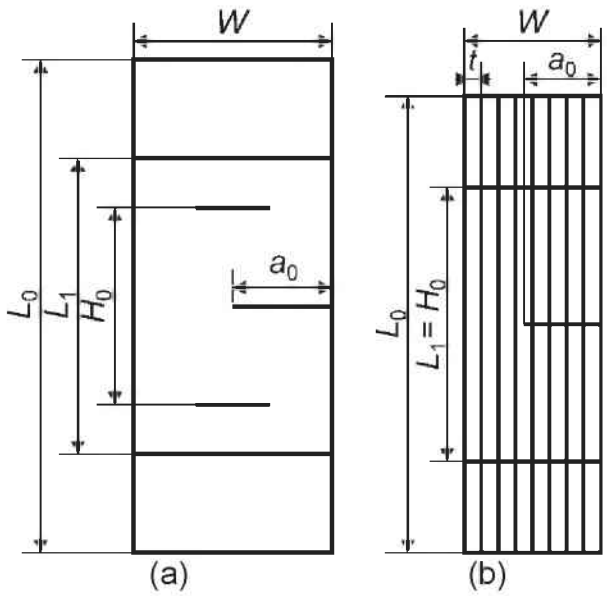

Fig. B.1 Single edge notch tension (SE(T)) specimens for the fracture mechanics tests. (a) Single layer and multilayer in crack divider configuration. (b) Multilayer in crack arrester configuration.

The tensile tests are carried out at a constant displacement rate of 0.8 mm/s on a Zwick tensile testing machine with a 1 kN load cell. Strain measurement is conducted with a videoextensometer. The tests are carried out at room temperature (approx. 25 °C) in ambient air.

2.2. Multilayer fabrication and fracture mechanics testing

For fracture mechanics testing of the single sheets of paper, single edge notch tension (SE(T)) specimens are fabricated. The SE(T) specimens have a width W = 60 mm, a total length L_0 = 180 mm and a thickness $B = t$ (Fig. B.1a). Before testing a notch is introduced with a razorblade. The initial crack length is $a_0 = 0.5W$. The specimens are clamped for testing with a distance between the clamps L_1 = 70 mm. The load line displacement is measured at an initial gauge length H_0 = 40 mm.

Multilayer specimens for fracture mechanics testing are manufactured in both crack arrester (CA) and crack divider (CD) configuration, see Fig. B.1. The specimens are glued together only at the ends, in the area where they are clamped during the tests. The glue used is Planatol BB®, a special paper glue.

The multilayer in CD configuration consists of five paper sheets, with a total thickness $B = 5t$, but otherwise the same geometry as described above for the single layers (Fig. B.1a). For the tests in CA configuration, SE(T) specimens with $W = 32t$ and $B \approx 10$ mm, glued similarly to the CD configuration, are fabricated. In this configuration the distance between the clamps equals the gauge length $L_1 = H_0$ = 90 mm and L_0 = 180 mm again (Fig. B.1b). Using a

razorblade 16 sheets are completely cut through and a 17th sheet is cut to about 0.5*B* from the side, giving an initial crack length of $a_0 \approx 16.5t$.

Fracture mechanics tests are conducted on 20 single sheet specimens, 5 multilayers in CD configuration and 10 specimens in CA configuration. Due to the high anisotropy in the tensile properties, all specimens are fabricated with the notch lying perpendicular to the transverse direction of the paper. The load line displacement (v_{LL}) is measured with a videoextensometer in CD configuration and with a clip-gauge in CA configuration. Photographs of the specimens are taken during the fracture mechanics tests using a digital camera mounted on the crosshead of the tensile testing machine. Otherwise the same testing equipment and parameters as for the tensile tests are used, see Section 2.1.

2.3 Determination of the *J*–Δ*a*-curve

As the load displacement curves in the fracture mechanics tests strongly deviate from linearity for the single sheets and both multilayer configurations, linear elastic fracture mechanics is not applicable and elastic-plastic fracture mechanics has to be used for the evaluation of the tests. Therefore the crack growth resistance is determined in terms of *J*-integral vs. crack extension (*J*–Δ*a*) curves. For the calculation of the experimental *J*-integral values, all specimens are treated as homogeneous specimens.

The *J*-integral evaluation is not standardized for the SE(T) specimen, therefore the procedure proposed in Cravero et al. [B.9] is used for the *J*-calculation. The experimental *J*-integral is calculated as the sum of the so-called elastic (J_{el}) and plastic (J_{pl}) components:

$$J = J_{el} + J_{pl}, \tag{B.3}$$

with

$$J_{el} = \frac{K^2\left(1-\nu^2\right)}{E}, \tag{B.4}$$

for plane strain conditions, with ν being the Poisson's ratio. A Poisson's ratio of $\nu = 0.29$ is taken from literature [B.10,B.11] for the transverse direction of paper. The stress intensity factor *K* is calculated according to [B.9,B.12]:

$$K = \frac{P}{B\sqrt{W}} f\left(\frac{a}{W}\right). \tag{B.5}$$

The geometry factor *f*(*a*/*W*), given in [B.9], increases from 2.74 for *a*/*W* = 0.5 to 4.3 for *a*/*W* = 0.67. The plastic component of the *J*-integral J_{pl} is determined by

$$J_{pl} = \frac{\eta A_{pl}}{Bb}. \qquad \text{(B.6)}$$

In Eq. (B.6), the parameter $b = W - a$ is the initial ligament length. The non-dimensional parameter η has been numerically evaluated and plotted for clamped SE(T) specimens with varying a/W and L_1/W ratios in [B.9]. For a/W = 0.5, η = 1.03 for the CA configuration, and η = 0.8 for the single sheets and the CD configuration. The plastic component of the work inserted into the specimen by the applied forces is denoted as A_{pl}, which is determined from the area under the load–displacement- (P–v_{LL}-) curve.

It has been tried to calculate the experimental J-integral values also following the crack growth corrected J-evaluation procedure described in [B.9]. Since the differences are less than 5 %, we adopt the simpler procedure as described above.

The measurement of the crack extension Δa in paper is difficult, as crack growth occurs inside a large damage zone where fiber pull-out, breakage and bridging occurs, making an optical crack length measurement difficult. In [B.13] two new methods to measure the fracture toughness in short fiber composites, such as paper, were introduced. These methods, the first using cohesive zone modeling, the second local deformation analysis, are applied to the single paper sheets investigated in the current work and allow the determination of the J–Δa-curve.

In the CA configuration the point of fracture initiation is taken where the first pre-damaged layer fractures, which is seen as a small load drop in the P–v_{LL}-curve. Subsequent crack extension due to fracture of previously undamaged sheets is monitored using photographs taken during the tests. Crack growth in this case is discontinuous and the crack length increases in steps of t.

3. Results

The results of the tensile tests for the longitudinal and transverse direction are summarized in Table B.1, where $R_{p0.1}$, R_m and ε_f denote the 0.1 % proof stress, the tensile strength, and the engineering fracture strain, respectively. For the transverse direction a Young's modulus E of 2.42 GPa is measured from the stress–strain- (σ–ε-) curves, which corresponds well with values measured in transverse direction for similar paper qualities [B.14].

Table B.1.
Material properties of the tested paper determined in tensile tests.

	$R_{p0.1}$ [MPa]	R_m [MPa]	ε_f [%]
Longitudinal Direction	20 (± 1.4)	48.9 (± 1.9)	2.51 (± 0.2)
Transverse Direction	10 (± 0.5)	28.5 (± 2.1)	6.46 (± 0.2)

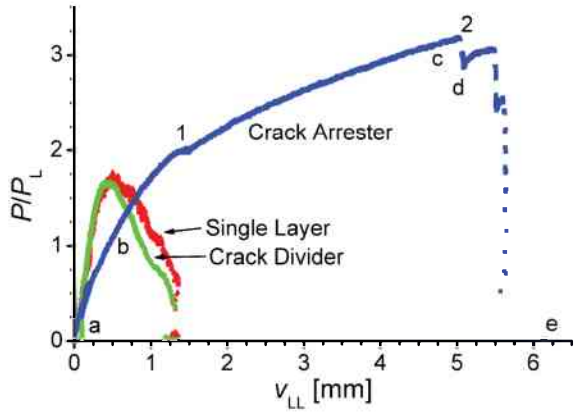

Fig. B.2 Normalized load displacement curves of single layer SE(T) specimens and the two multilayer configurations; P_L denotes the plastic limit load.

In Fig. B.2 the P–v_{LL}-records determined in the fracture mechanics tests of the single sheets, the crack divider (CD) and crack arrester (CA) configuration are plotted. The applied load P is normalized with the plastic limit load P_L, calculated according to [B.12],

$$P_L = 1.072\,\eta_L B b \sigma_F\,, \tag{B.7}$$

with

$$\eta_L = \sqrt{1+\left(\frac{a}{b}\right)^2} - \frac{a}{b}. \tag{B.8}$$

The parameter $\sigma_F = \left(R_{p0.1} + R_m\right)/2$ in Eq. (B.7) denotes an average flow stress of the material. The normalization is done to eliminate the influence of the specimen thickness on the load.

The P–v_{LL}-curve of the single sheet SE(T) specimen shows a maximum, where the damage zone starts to form in front of the initial crack tip. Thereafter the load decreases due to the occurring damage processes in the ligament and at a later stage due to crack extension. Final fracture of the specimens occurs at approximately one third of the maximum load, see [B.13] for a detailed analysis of the tests. The crack growth resistance (J–Δa-) curve determined from the experiments is shown in Fig. B.3. The single sheets show a J_i value of 7.3 ± 0.3 kJ/m² and a J_{max} of 8.4 ± 0.5 kJ/m².

The P–v_{LL}-curves of all five tested multilayer specimens in the CD configuration are very similar to those of the single sheet SE(T) specimens. An exemplary curve is shown in Fig. B.2. The J–Δa-curve in CD configuration is identical to that of the single sheets, with J_i = 7.3 ± 0.3 kJ/m² and J_{max} of 8.4 ± 0.5 kJ/m².

For the CA configuration the run of the P–v_{LL}-curves in Fig. B.2 varies strongly from that of the single layers or CD configuration. At point 1 in Fig. B.2,

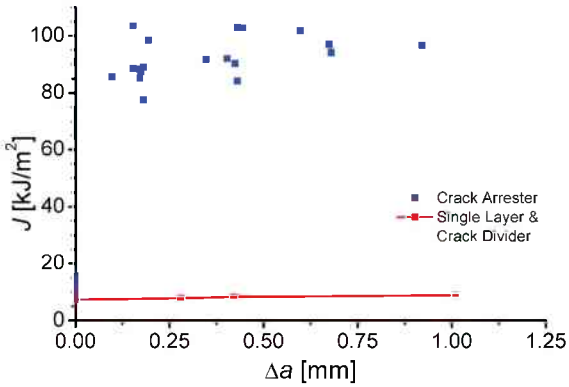

Fig. B.3 Crack growth resistance curves of the single layer specimens and the multilayers in crack arrester and crack divider configuration.

the first pre-damaged layer of the CA specimen breaks, indicating fracture initiation. Thereafter, the load further increases to a maximum value P_{max} (point 2), where, accompanied by distinct load drops, the previously undamaged layers fracture in rapid succession until final failure of the sample. The resulting J–Δa-curve of this configuration, containing the results of ten specimens, is shown in Fig. B.3. For the CA configuration an initiation toughness value J_i of 11.7 ± 2 kJ/m² is measured. The toughness increases strongly to maximum values J_{max} = 92.5 ± 7 kJ/m² after fracture of the first layer. Note that this value is very high, higher than the critical J-integral values of common aluminum alloys; only very tough materials, such as certain steels, exhibit higher fracture toughness values.

Fig. B.4 shows the area around the initial crack tip of a specimen tested in CD configuration, which was unloaded shortly before final fracture occurred. The photographs of the multilayers in the CA configuration with the labels a – e shown in Fig. B.5 correspond to the points a – e in Fig. B.2. The evolution of a high crack tip opening displacement (CTOD) with increasing load is visible. Fracture of the first previously undamaged layers remote from the initial crack tip can be seen in Fig. B.3c and B.3d

4. Discussion

The normalized load–displacement-curves of the single sheet SE(T) specimens and the multilayers in CD configuration are very similar (Fig. B.2), and also the J–Δa-curves are identical (Fig. B.3). In the literature, multilayers with weak interfaces in CD configuration have usually a higher fracture resistance than the homogeneous bulk material. This effect, first reported by Embury et al. [B.6], is attributed to the different prevalent stress state [B.6, B.7]. While a thick fracture mechanics specimen fractures under predominantly plane strain conditions, a multilayer with weak interfaces in CD configuration

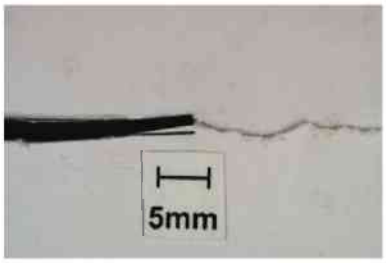

Fig. B.4. Region in front of the initial crack tip of a specimen in crack divider configuration after unloading.

resembles a series of thin parallel samples under plane stress conditions, which generally exhibit a higher fracture resistance. In our case, both the reference specimen, consisting of a single thin sheet of paper, and the multilayers in CD configuration are dominated by plane stress conditions, therefore no difference in the fracture behavior can be expected. This is the reason why the values of the fracture initiation toughness J_i and the J–Δa-curves of the multilayers in CD configuration fall together with that of the single sheet specimen.

Table B.2.
Comparison of fracture mechanical characteristics of the different tested configurations.

	J_i [kJ/m²]	J_{max} [kJ/m²]
Single layer & CD configuration	7.3 ± 0.3	8.4 ± 0.5
CA configuration	11.7 ± 2	92.5 ± 7

The fracture initiation toughness J_i for the CA configuration is higher than that for the single layer specimen, see Table B.2. This is caused by the fact that point 1 in Fig. B.2, where J_i is measured in the CA configuration, is not the point where physical fracture initiation occurs, but where final fracture of the first pre-damaged layer takes places. Therefore, it is more reasonable to compare the J_i value in CA configuration to the J-value where final fracture occurs, J_{max}, of the single sheets, which gives a better agreement.

Although all configurations show similar J_i-values, the value of J_{max} in the CA configuration rises to values approximately ten times higher than that of the other configurations. The improved fracture toughness is also clearly visible on the photographs shown in Fig. B.4 and Fig. B.5. Distinctly larger CTOD values, indicating higher fracture toughness, can be seen in the CA specimen after fracture of the first previously undamaged layers, when compared to the sample in CD configuration after testing.

The very high maximum J-integral value J_{max} of the multilayer in CA-configuration can be formally ascribed to the high shielding effect of air between the paper layers, compare Eq. (B.1) and Eq. (B.2) with $E_1 = 0$. According to the model, this allows the crack to propagate into the interlayer, but then the crack driving force at the soft-hard interface decreases to zero. This means that the

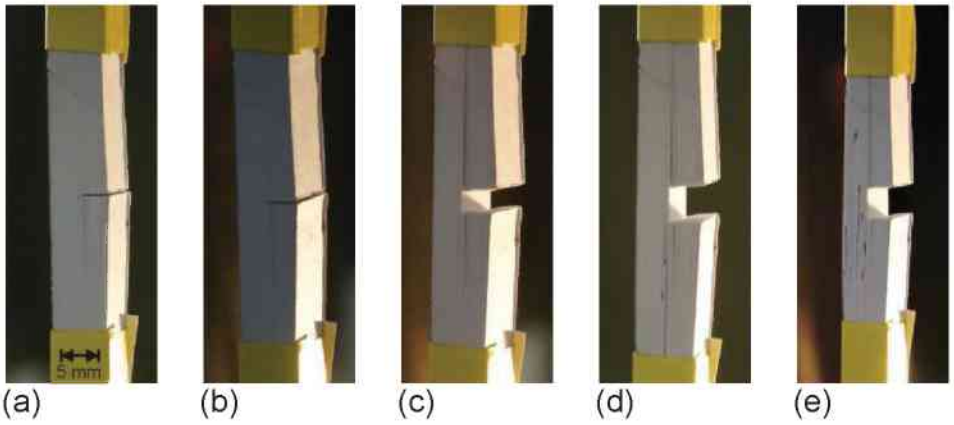

Fig. B.5. Specimen in crack arrester configuration during testing: (a) unloaded, (b) before fracture of the pre-damaged layer, (c) before reaching P_{max}, (d) after fracture of the first undamaged layers, (e) final failure. The labels of the images correspond to the letters in Fig. B.2.

specimen does not "feel" the crack anymore; the remaining ligament of the CA-multilayer should behave like a tensile specimen.

Stress–strain-curves are calculated from the load–displacement-data (Fig. B.2) for the CA configuration, by dividing the load P by the area of the initially undamaged ligament and normalizing the displacement v_{LL} with the initial gauge length. In Fig. B.6 such a stress–strain-curve is shown, together with the stress–strain-curve measured in transverse direction in the tensile tests. The curves are very similar, only the fracture strain of the multilayer in CA configuration is about 0.5% lower than the engineering fracture strain in the tensile test ε_f. This shows that after crack growth through the initially damaged layer, the crack arrests in the interlayer and the remaining ligament deforms really like a tensile test specimen, nearly until final failure.

For a given material, the volume subject to plastic deformation changes drastically with crack arrest. Before crack arrest, the plastic deformation is confined to the plastic zone around the crack tip, due to the triaxial stress state. The plastic zone size depends mainly on the applied J-integral and the yield strength, e.g. [B.15]. Upon crack arrest, the triaxial stress state in the ligament is relaxed and the ligament deforms like in a uniaxial tensile test. The plastic work during the tensile loading is given by

$$A_{pl} = V\int_0^{\varepsilon_f}\sigma d\varepsilon = Bb_{arr}L_1\int_0^{\varepsilon_f}\sigma d\varepsilon\,, \qquad (B.9)$$

where V denotes the plastically deformed volume and b_{arr} the ligament length of the specimen after crack arrest. The magnitude of the maximum J-integral value

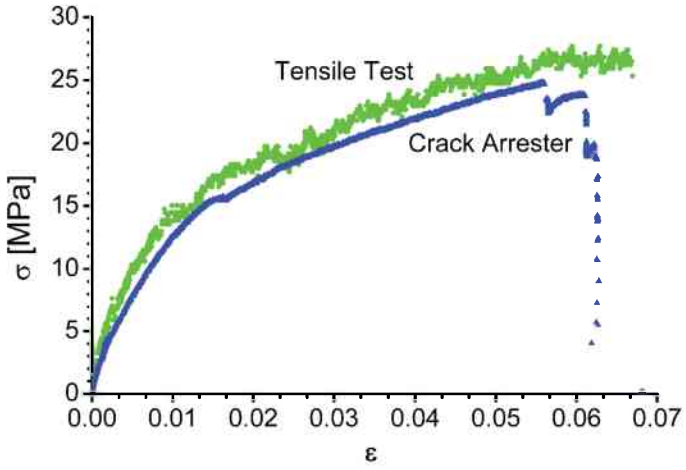

Fig. B.6 Comparison of the stress strain behavior of the CA configuration and the tensile tests conducted in transverse direction.

J_{max} of the multilayer in CA-configuration can be estimated by inserting Eq. (B.9) into Eq. (B.6), leading to

$$J_{max} \approx \eta L_1 \int_0^{\varepsilon_f} \sigma d\varepsilon \,. \tag{B.10}$$

Hereby it is assumed that b_{arr} and the initial ligament length do not differ much, $b_{arr} \approx b$. A similar relation has been derived in [B.16]. Inserting the engineering fracture strain in the tensile test ε_f = 6.5%, η = 1.03 and L_1 = 90 mm into Eq. (B.10) gives a value of $J_{max} \approx$ 110 kJ/m², which is 15 % higher than the measured J_{max}-value, see Table B.2. This discrepancy can be mainly explained by the difference in the fracture strains determined in the tensile tests and for the CA configuration (Fig. B.6).

It has to be noted here that the *J*-integral loses its meaning as a parameter describing the stress- and strain field in front of the crack tip, as described in [B.15], after crack arrest. Nevertheless, for loading beyond the point of crack arrest, J_{max} gives a specific energy consumed in the specimen until the onset of final failure.

For other interlayer materials than air with $E_1 > 0$, the magnitude of the plastically deformed volume depends on the interlayer and interface strength. Only in regions where debonding between the interlayer material and the ligament volume occurs, the triaxial stress state is fully relieved and plastic deformation can occur like in a tensile test. This means that a debonding length L_{deb} should be inserted in Eq. (B.10) instead of the full distance between the clamps L_1. For a multilayer with high interface strength, this debonding length L_{deb} is small, limiting the plastic deformation and, consequently, the achievable value of J_{max}. Therefore, a low interface and interlayer strength promotes a damage resistant behavior.

A thorough case study of the effect of compliant or soft interlayers on the crack driving force is still missing. Taking the preliminary result for interface transitions, Eq. (B.2), it is seen that the relative jump of the Young's modulus at the interface decreases with increasing Young's modulus of the interlayer material E_1. Therefore, it might be assumed that the shielding effect of a compliant interlayer will decrease correspondingly. It is interesting to consider again the very fracture resistant deep sea sponge mentioned in the Introduction: Nanoindentation measurements [B.17] gave a Young's modulus for bio-glass of E_2 = 42 GPa, the protein interlayers had $E_1 \approx 1$ GPa. Inserting these values into Eq. (B.2) give a relative jump of the Young's modulus at the protein/glass interface of $(E_1 - E_2)/(E_1 + E_2) = -0.976$. This value comes already very close to the theoretical limit of –1, which we observed with air as interlayer material.

The same effect has been also observed in structures made of geometrically locked tetrahedral elements, which also exhibit extraordinary impact resistance [B.18, B.19]. As there is no matrix between the elements, a crack propagating through one element is stopped in the void between the elements.

It should be noted that a material inhomogeneity effect appears also if the elastic modulus is constant in a multilayer configuration, but the yield strength exhibits a spatial variation [B.5, B.20]. Preliminary results show that, in general, the shielding effect of thin, soft interlayers is not as high as that in multilayers with a variation in the elastic modulus.

The findings of the current presentation can be transferred to arbitrary materials. A multilayer build-up with air or very compliant or soft interlayer materials in crack arrester configuration will show a highly improved fracture toughness compared to the bulk material.

Due to the small sheet thickness, the paper multilayer in crack divider configuration shows the same fracture toughness as the single sheet material. There exists a third loading case, commonly referred to as short transverse configuration, where the load is applied perpendicular to the layers. It is clear that the multilayer has no strength at all in the latter configuration and, thus, such a loading case must be prevented by constructive means. This is accomplished, for example, in the structure of the deep sea sponge where the skeleton consists of rods with cylindrical (and not planar) layers [B.1, B.3].

5. Conclusions

Multilayer arrangements with compliant or soft interlayer materials in crack arrester configuration show highly improved fracture toughness compared to that of the bulk material. The reason is that the spatial variation of the material properties strongly reduces the crack driving force when the crack tip is located in the interlayer. The effect can be optimized by building multilayers with very

soft interlayer materials, such as air. This is demonstrated on the example of multilayers made of commercially available printing paper. Measured in terms of the critical *J*-integral, the paper multilayer in crack arrester configuration shows approximately ten times higher fracture toughness than that of the single layer specimens. Relations are given that allow an assessment of the effect. The idea can be transferred to arbitrary materials.

Acknowledgement

Financial support by the Austrian Federal Government and the Styrian Provincial Government within the research activities of the K2 Competence Center "Integrated Research in Materials, Processing and Product Engineering", under the frame of the Austrian COMET Competence Center Program, is gratefully acknowledged (Projects A4.11 and A4.20).

References

[B.1] Dunlop JWC, Fratzl P. Ann Rev Mater 2010;40:1.
[B.2] Kamat S, Kessler H, Ballarini R, Nassirou M, Heuer AH. Acta Mater 2004;52:2395.
[B.3] Kolednik O, Predan J, Fischer FD, Fratzl P. Adv Funct Mater 2011;21:3634.
[B.4] Walter SL, Flinn BD, Mayer G. Mater Sci Eng C 2007;27:570.
[B.5] Simha NK, Fischer FD, Kolednik O, Chen CR. J Mech Phys Solids 2003;51:209.
[B.6] Embury JD, Petch NJ, Wraith AE, Wright ES. Trans Metall Soc AIME 1967;239:114.
[B.7] Herzberg RW. Deformation and fracture mechanics of engineering materials. New York: Wiley; 1976.
[B.8] Kolednik O, Predan J, Shan GX, Simha NK, Fischer FD. Int J Solids Struct 2005;42:605.
[B.9] Cravero S, Ruggieri C. Engng Fract Mech 2007;74:2735.
[B.10] Szewczyk W. Fibres Text East Eur 2008;16:117.
[B.11] Wellmar P, Fellers C, Delhage L. Nord Pulp Paper Res 1997;12:189.
[B.12] Anderson TL. Fracture mechanics: fundamentals and applications, third ed. Boca Raton: CRC Press; 2005.
[B.13] Zechner J, Janko M, Kolednik O. Comp Sci Tech 2013;74:43.
[B.14] Tanaka A, Yamauchi T. J Mater Sci 2000;35:1827.
[B.15] Hutchinson JW. J Mech Phys Solids 1968;16:337.
[B.16] Zechner J, Kolednik O. Engng Fract Mech, accepted for publication.
[B.17] Woesz A, Weaver JC, Kazanci M, Dauphin Y, Aizenberg J, Morse DE, Fratzl P. J Mater Res 2006;21:2068.

[B.18] Dyskin AV, Estrin Y, Kanel-Belov AJ, Pasternak E. Comp Sci Tech 2003;63:483.
[B.19] Dyskin AV, Estrin Y, Kanel-Belov AJ, Pasternak E. Scripta Mater 2001;44:2689.
[B.20] Kolednik O. Int J Solids Struct 2000;37:781.

5.3.2 Multilayer with elastic inhomogeneity 2: Al7075/Adhesive

The aim of the investigations on the adhesively bonded aluminum multilayers was to investigate the material inhomogeneity effect on a multilayer system with Young's modulus inhomogeneity that could be used for engineering applications and to study how far the results from the model system described in Section 5.3.1 are transferable. Furthermore the results should allow a comparison with the aluminum based multilayers with a yield strength inhomogeneity discussed in the next section. Also for this system the local jump of the Young's modulus is very high, which is reflected in a Dundurs parameter of −0.99. In Publication C the results of the investigations are presented and discussed.

The fracture mechanics tests in CD configuration yield the same crack growth resistance curve as the pure Al7075-T6 sheets, which was already observed and explained for the paper multilayers in Section 5.3.1.

Markedly higher fracture initiation toughness values are measured in the CA configuration when compared to the CD configuration or the Al7075-T6 sheets. This is caused by a change in the orientation of crack growth with respect to the rolling texture of the sheets. For the single sheets and the CD configuration the fracture mechanics tests are conducted in the long-transverse direction, whereas the crack grows in the thickness direction of the sheet in CA configuration. This difference in the crack growth direction has a significant influence on the fracture toughness and can explain the difference. After fracture initiation, the crack grows through the pre-fatigued layer into the compliant interlayer and arrests there. No delamination is observed in this early phase of crack growth and arrest. This indicates that the crack stops in the interlayer due to the material inhomogeneity effect and not because of decohesion of weak interfaces as described in Section 1.2.1. Upon further loading, delamination starts and the remaining ligament deforms again like in a tensile test in the area where delamination occurs. Before final fracture, a J_{max} being 450 times higher than the fracture initiation toughness is reached. Fracture of the ligament occurs, when the fracture stress of Al7075-T6 is reached.

Eq. (5.1), which allows the estimation of J_{max} from the mechanical properties of the stiff material and the specimen geometry (see Section 5.3.1), can be rewritten for this case as,

$$J_{max} = \eta R_m \varepsilon_F L, \tag{5.2}$$

where the strain energy density is estimated as the product of tensile strength and fracture strain. In this case L is the length where the material deforms plastically and necking occurs. The agreement of the estimated and measured values is very good, the difference is smaller than 5%.

Publication C

Fracture resistance of aluminum multilayer composites

Johannes Zechner and Otmar Kolednik

Accepted for publication in

Engineering Fracture Mechanics

Abstract

The so-called material inhomogeneity effect, which influences the crack driving force in inhomogeneous materials, has recently been found to contribute to the excellent behavior of some fracture resistant biomaterials. The current study aims to transfer these findings to engineering materials, by experimentally investigating the fracture behavior of multilayers consisting of a high-strength aluminum alloy and thin, soft polymer interlayers. Structures in crack divider and crack arrester (CA) configuration are tested. The results show that the structures in CA configuration exhibit a tremendously improved fracture resistance compared to the homogeneous bulk material. The reason is that cracks are completely arrested in the soft interlayers. This effect appears without delamination, i.e. it is basically different from the well-known delamination effect on weak interlayers.

1 Introduction

The heat-treatable Al-Zn-Mg-Cu (7xxx) alloys have the highest strength to weight ratio of all aluminum alloys, making them ideal candidates for lightweight constructions. Nevertheless, the application of these alloys in safety critical structures is limited due to their rather poor resistance to fracture and fatigue.

To overcome the dilemma that increasing strength leads to a toughness decrease in many materials and alloys, damage tolerant multilayered systems have been invented and intensively investigated in the past decades [C.1]. The basic idea behind these multilayered structures is to increase the fracture resistance by the delamination of weak interfaces, while at the same time preserving the high material strength [C.1-C.4]. Two configurations, denominated as crack divider (CD) and crack arrester (CA) configuration, are examined in these publications. In the CD configuration the crack plane is normal to the layers and the crack propagates through all layers at once (Fig. C.1a), while in the CA configuration the crack also propagates perpendicular to, yet sequentially through the layers (Fig. C.1b).

In the first works on the subject, metal/metal multilayer systems with weak interlayers, introduced by soldering, explosion-cladding, or roll-bonding, were investigated with respect to their impact toughness [C.3] or fracture toughness [C.4]. Compared to a homogeneous material of the same total thickness, the fracture behavior was improved in both configurations. This fact has been attributed to the delamination of the weak interfaces in the multilayers. The delamination diminishes the hydrostatic stress state around the crack tip, which leads to a retardation of void-initiation [C.5] and a reduction of the void growth rates [C.6] and, therefore, to an increased fracture toughness.

Nomenclature

a	crack length
a_0	initial crack length
Δa	crack extension
A_{pl}	plastic area under the load vs. load-line-displacement curve
A_{el}	elastic work
A_{tot}	total area under the load vs. load-line-displacement curve
b	ligament length
b_{arr}	ligament length after crack arrest
B	specimen thickness
C_{inh}	material inhomogeneity term
E	Young's modulus
F	applied load
F_{max}	maximum load reached in the fracture mechanics test
H	gauge length
J	J-integral
J_{el}	elastic component of the J-integral
J_{pl}	plastic component of the J-integral
J_{tip}	near-tip J-integral
J_{far}	far-field J-integral
J_{max}	maximum J-integral
$J_{F_{max}}$	J-integral value at F_{max}
J_{IC}	fracture toughness in terms of the J-integral
J_c	fracture initiation toughness in the CA configuration
K	stress intensity factor
K_{JC}	critical stress intensity factor calculated from J_{IC}
L	length plastically deformed in the fracture mechanics specimen
n	strain hardening exponent
N_u	number of undamaged layers
$r_y^{(pl\sigma)}$	plastic zone radius in plane stress
R	crack growth resistance
$R_{p0.2}$	yield strength
R_m	ultimate tensile strength
t	layer thickness
t_{opt}	optimum layer thickness
v_{LL}	load-line-displacement curve
V	volume plastically deformed in the fracture mechanics specimen
W	specimen width
γ	nondimensional factor to account for crack growth effects on J
Γ	surface energy needed to create new fracture surfaces
ε	engineering strain
ε^*	critical total strain
ε_F	engineering fracture strain
ε_U	uniform elongation
η	nondimensional factor connecting A_{pl} to J_{pl}
η^*	nondimensional factor connecting A_{tot} to J
ν	Poisson's ratio
σ	engineering stress
σ_{max}	maximum nominal stress in the ligament after crack arrest

CA crack arrester configuration
CD crack divider configuration
COD crack tip opening displacement
C(T) compact specimen
SE(T) single edge notch tension specimen

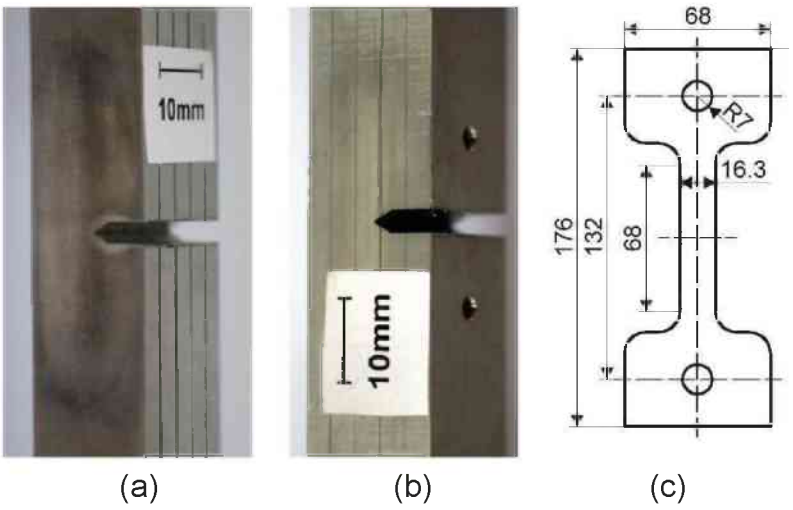

Fig. C.1 Notched and pre-fatigued areas of the (a) crack divider and (b) crack arrester configurations. (c) Outer dimensions of the laser cut aluminum sheets.

Additionally, in the CA configuration the crack tip is blunted when it grows into the delaminated area, and a re-initiation of the crack is necessary for further crack growth.

Similar observations have been made in laminates where metal layers were combined with polymer adhesives [C.7,C.8]. A recent development of these polymer/metal multilayers are fiber metal laminates, where the polymer adhesives are reinforced by glass- or aramid fibers [C.9,C.10]. The fibers bridge the zone behind the crack tip if the crack grows into the polymer, which should lead to a further improvement of the fracture behavior of the laminate.

2 The material inhomogeneity effect

An additional mechanism, denominated the material inhomogeneity effect, has recently been found to influence the fracture behavior of inhomogeneous materials. The reason for the effect is that a material inhomogeneity influences the crack driving force. The effect occurs in all materials where the mechanical properties (Young's modulus E, yield strength $R_{p0.2}$, strain hardening exponent n, or thermal residual stresses) exhibit a gradient or show jumps at interfaces. For elastically inhomogeneous materials the effect has been known for a long time already, e.g. [C.11-C.15], but recently application of the concept of

configurational forces [C.16,C.17] has enabled a more general treatment of the problem, see e.g. [C.18,C.19] for a more extensive literature review.

In an inhomogeneous material, the crack driving force, expressed in terms of the near-tip J-integral J_{tip}, is given as sum of two terms [C.18,C.19]:

$$J_{tip} = J_{far} + C_{inh} . \qquad (C.1)$$

The first term on the right hand side of Eq. (C.1), the far-field J-integral J_{far}, measures the driving force that is inserted into the specimen by the applied forces. J_{far} can be evaluated from the load–displacement-record. The second term on the right hand side of Eq. (C.1), the material inhomogeneity term C_{inh}, describes the influence of the material inhomogeneity on the crack driving force. In a homogeneous material C_{inh} = 0 and J_{tip} = J_{far}, i.e. the J-integral is path independent. If the crack grows from a material with lower Young's modulus or yield strength towards a material with higher Young's modulus or yield strength ("compliant/stiff-" or "soft/hard transition-"), C_{inh} is negative and J_{tip} becomes smaller than J_{far}; the material inhomogeneity shields the crack tip. In the opposite case where a stiff/compliant or hard/soft transition occurs, C_{inh} is positive and J_{tip} becomes bigger than J_{far}; the material inhomogeneity has an anti-shielding effect. An intuitive explanation for the influence of the material inhomogeneity on the crack driving force, which is based on the change of the stored elastic energy in the crack tip field if a crack crosses an interface, is given in [C.20].

A general criterion for initiation of crack growth under monotonic loading is that the crack driving force equals or exceeds the fracture resistance R of the material,

$$J_{tip} \geq R . \qquad (C.2)$$

Assume a (high-strength) material with a given crack growth resistance R, which is determined by the dissipating processes occurring within the process zone and the (small) plastic zone. Due to the decrease of the crack driving force J_{tip}, caused by the negative material inhomogeneity term C_{inh} in the compliant/stiff- or soft/hard transition, a higher value of J_{far}, i.e. a higher applied load, is necessary to initiate crack growth, compared to the case of a homogeneous material. This leads to an increase of the fracture initiation toughness, if a crack crosses an interface to a stiffer or harder material. On the contrary, for the stiff/compliant- or hard/soft transition, C_{inh} is positive and enhances the crack driving force, which reduces the local fracture initiation toughness.

If in a multilayer structure a soft interlayer is located in a hard bulk material, there is a hard/soft transition at the first interface and a soft/hard

transition at the second interface. Therefore, a crack in the hard material can easily grow into the soft phase due to the anti-shielding effect, but the crack driving force becomes very low near the second interface, inhibiting crack growth from the soft to the hard layer [C.20,C.21]. The effectiveness of the material inhomogeneity effect increases with increasing spatial variation of the mechanical properties [C.18,C.20,C.22]. If the inhomogeneity is pronounced enough, J_{tip} at the transition from the lower to the higher mechanical property can become lower than the fracture resistance of the material and the crack arrests in the soft interlayer. The crack arrest and the re-initiation of crack growth at the soft/hard or compliant/stiff transition determine the fracture behavior of the structure. An example where the material inhomogeneity effect is very effectively applied in nature is the skeleton of certain deep-sea sponges, which consist of glass layers separated by very thin, compliant protein layers. These structures show an excellent fracture resistance, although being mainly composed of very brittle bio-glass [C.20].

The influence of the material inhomogeneity effect on the fracture behavior of various composite systems, ranging from bimaterials to multilayers with periodically varying mechanical properties, has been described in several analytical and numerical studies and has been confirmed by experimental results [C.20,C.21,C.23-C.25]. It should be noted that the material inhomogeneity effect also influences the effective stress intensity range, the growth rate and the growth direction of fatigue cracks, which was shown both experimentally [C.26,C.27] and numerically [C.23,C.28,C.29]. All described effects caused by the material inhomogeneity term are independent of delaminating interfaces, making them fundamentally different from the effects described in Section 1.

Aim of the present study is to transfer and study the material inhomogeneity effect, which works so effectively in the skeleton of the deep-sea sponge, to engineering multilayer structures. Therefore, the influence of soft polymer interlayers on the fracture resistance of a high strength aluminum alloy is experimentally investigated. Multilayers in CD- and CA-configuration are built and tested in fracture mechanics experiments, Section 3. The experimental results, presented in Section 4, are discussed qualitatively and quantitatively in Section 5.

3 Experimental

3.1 Materials and mechanical properties

Peak aged sheets of the high strength aluminum alloy Al7075-T6 with a thickness t = 3.18 mm (1/8″) are used as the bulk material of the multilayers.

Tensile tests are conducted in rolling direction of the sheets on flat bar specimens of type H according to DIN 50125 with a width of 20 mm and a gauge length of 80 mm. A Zwick/Roell Z250 tensile testing machine with a 250 kN load cell is used to conduct the tests.

A commercially available two-component methacrylate adhesive, WELD-ON® SS315, is used to connect the aluminum layers for the multilayer build-up and serves as the soft phase in the multilayers. The mechanical properties of the adhesive are provided by the manufacturer.

3.2 Multilayer construction

Dog-bone shaped samples with dimensions given in Fig. C.1c are laser-cut from 2.3 x 0.8 m² Al7075-T6 sheets. Multilayer single edge notch tension (SE(T)) specimens in crack divider (CD) and crack arrester (CA) configuration are built using five sheets of Al7075-T6 connected by 0.1 mm thick layers of the adhesive, resulting in a total multilayer thickness of 16.3 mm. The adhesive is hardened for a minimum time of 24 h at room temperature.

3.3 Fracture mechanics testing

Fracture mechanics tests are conducted on single sheets of the aluminum alloy, as well as on multilayers in CD and CA configuration. The fracture toughness is measured in terms of J-integral versus crack extension (J–Δa-) curves. The fracture toughness of Al7075-T6 single sheets is determined in the longitudinal-long transverse direction. Pin-loaded SE(T) specimens with width W = 20 mm, thickness $B = t$, a mechanical notch length of 7 mm and a distance between the pin-loading points $H = 4W$ are tested using the multiple specimen method according to ASTM 1820-08 [C.30]. The specimens are pre-fatigued to an initial crack length a_0 of approximately $0.5W$. The critical fracture initiation toughness J_{IC} is defined as the intersection of the J–Δa-curve with the 0.2 mm offset line [C.30]. Seven SE(T) specimens are tested for the J–Δa-curve determination of Al7075-T6.

Depending on the desired configuration, notches are machined into the multilayers, which then are also pre-fatigued to an initial a_0/W-ratio of 0.5. Specimens in CD and CA configuration are depicted in Fig. C.1a and Fig. C.1b, respectively. In both configurations the specimens have a quadratic cross-section in the reduced area, where $W = B$ = 16.3 mm. In the CD configuration, single-specimen tests are conducted on two specimens to measure the J–Δa-curve. In these tests, the crack extension is measured using the direct current potential drop technique according to the International Standard ISO 12135

[C.31]. Since the potential drop technique is not applicable in the CA configuration, the J–Δa-curve is recorded using the multiple specimen method according to [C.30]. Here the fracture initiation toughness J_c is measured at the point where a first pop-in occurs on the load-displacement record. Three multilayer specimens are tested in the CA configuration.

All fracture mechanics tests are conducted on a Zwick tensile testing machine with a 100 kN load cell. The load-line-displacement (v_{LL}) is measured with a clip gauge at a gauge length of 50 mm. A constant machine crosshead speed of 0.8 mm/min is used for all fracture mechanics tests. A digital camera is mounted on the crosshead to take digital photographs of the specimens during testing.

As the J-integral evaluation is not standardized for the SE(T) specimen, the J-integral evaluation procedure described in [C.32] is applied. The crack growth corrected J-value at a given point n on the load–displacement-curve (F–v_{LL}-curve) with the corresponding crack length a_n is split into elastic and plastic components,

$$J_n = J_{eln} + J_{pln}. \tag{C.3}$$

The elastic component of the J-integral J_{eln} is given by

$$J_{eln} = \frac{K_n^2\left(1-\nu^2\right)}{E}, \tag{C.4}$$

with the stress intensity factor K calculated from the applied load F and a/W-ratio according to [C.31] and the Poisson's ratio ν = 0.33. The plastic component of the J-integral J_{pln} is given by

$$J_{pln} = \left[J_{pln-1} + \frac{\eta_{n-1}}{b_{n-1}B}\left(A_{pln} - A_{pln-1}\right)\right] \times \left[1 - \frac{\gamma_{n-1}}{b_{n-1}}\left(a_n - a_{n-1}\right)\right], \tag{C.5}$$

where the ligament length $b = W - a$ and $\eta(a/W)$ is a nondimensional factor connecting the plastic work A_{pl} to J_{pl}. The plastic work A_{pl} is determined from the F–v_{LL}-record by subtracting the elastic work A_{el}, calculated using the elastic compliance, from the total consumed energy A_{tot}. The η-factors, taken from [C.32], lie between 2 and 2.4 for a/W-values between 0.45 and 0.7. The parameter γ is a nondimensional factor introduced to account for crack extension,

$$\gamma_{n-1} = \left[-1 + \eta_{n-1} - \left(\frac{b_{n-1}}{W} \frac{\eta'_{n-1}}{\eta_{n-1}} \right) \right], \tag{C.6}$$

with

$$\eta'_{n-1} = W \left. \frac{d\eta}{da} \right|_{n-1}. \tag{C.7}$$

The parameter γ varies between 0.75 and 1.5 for a/W-values between 0.45 and 0.7.

4 Results

The engineering stress–strain (σ–ε) curve of the single sheet Al7075-T6 is plotted in Fig. C.2, showing a high strength and low strain hardening behavior of the material. The Young's modulus E, the 0.2 % proof stress $R_{p0.2}$, the ultimate tensile strength R_m, the uniform elongation ε_U, and the engineering fracture strain ε_F of the two multilayer constituents are given in Table C.1. The mechanical properties of the aluminum alloy and the adhesive vary by factors of approximately 300 for the Young's modulus and 40 for the tensile strength. Due to this strong inhomogeneity in the mechanical properties, a pronounced effect of the material inhomogeneity on the fracture behavior can be expected according to [C.20].

The J–Δa-curve of the single sheet Al7075-T6 is plotted in Fig. C.3. A valid fracture initiation toughness value of J_{IC} = 8 kJ/m² was determined in the tests. This value can be converted to a stress intensity value of K_{JC} = 25 MPa$\sqrt{m}$ using Eq. (C.4).

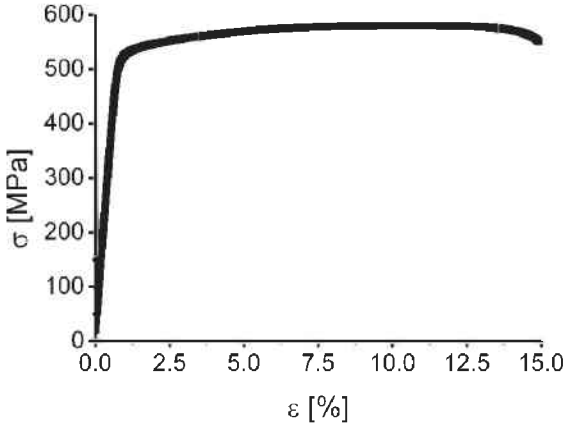

Fig. C.2 Engineering stress–strain-curve of Al7075-T6.

Table C.1.
The mechanical properties of the constituents of the multilayers.

	E [GPa]	$R_{p0.2}$ [MPa]	R_m[MPa]	ε_U [%]	ε_F [%]
Al7075-T6	70	520 ± 1.2	580 ± 1.2	9.7 ± 0.05	14 ± 0.3
SS315	0.24		15		100

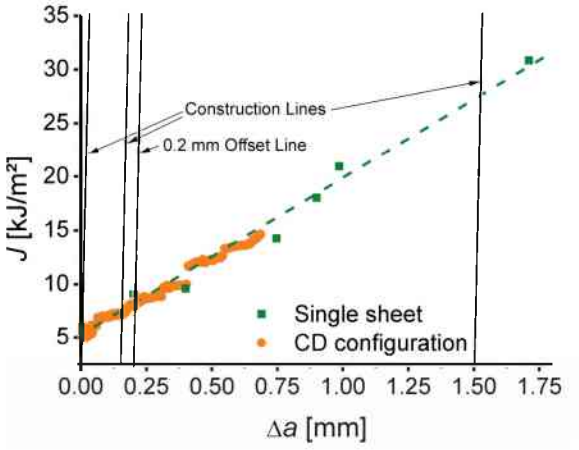

Fig. C.3 Crack growth resistance curve of the Al7075-T6 single sheets and the crack divider (CD) configuration.

Additionally, in Fig. C.3 the J–Δa-curve of a test in CD configuration is plotted, exhibiting similar fracture initiation toughness and slope of the J–Δa-curve as the single sheet specimens. The second specimen tested in CD configuration shows an identical behavior. Both single sheet and CD configuration exhibit several pop-ins during the crack extension.

The F–v_{LL}-curves of multilayers tested in CD and CA configuration and the resulting J–Δa-curve of the CA configuration are shown in Fig. C.4a and Fig. C.4b, respectively. The error bars in Fig. C.4b show the standard deviation from the average value of the three tested specimens. The difference in the energy consumed during the fracture mechanics tests, given by the area under the F–v_{LL}-records, between the two configurations is clearly visible in Fig. C.4a. In Fig. C.4a and Fig. C.4b the parts of the F–v_{LL}- and J–Δa-curve where crack growth initiation and the first crack extension (from Point b to Point b') occur are magnified in the diagrams. The fracture initiation toughness in this configuration is J_c = 30 (± 7.5) kJ/m². After this initial crack extension, the J–Δa-curve increases sharply to extremely high J-values. During this increase, crack extension is caused by the lateral contraction (Points b' – d) and localized necking (Points d – e) of the specimen, and is measured from the digital photographs. At Point e, where a maximum J-value of $J_{max} \approx 13.7 \times 10^3$ (± 500) kJ/m² is reached, unstable fracture of the remaining ligament occurs.

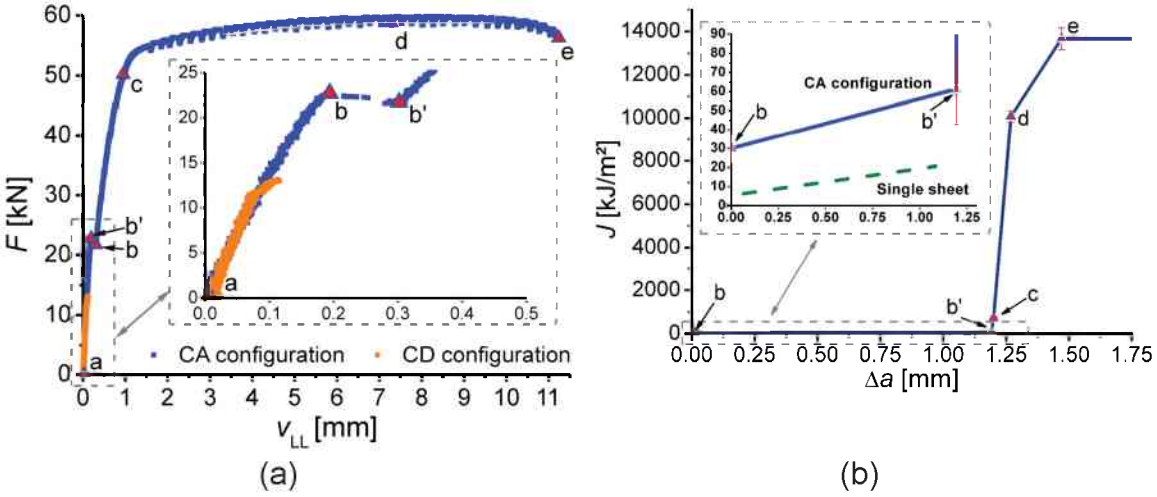

Fig. C.4 (a) Load–displacement-curves of multilayers tested in crack arrester (CA) and crack divider (CD) configuration. The letters a-e correspond to the photographs in Fig. C.6 a-e. (b) The crack growth resistance curve for the crack arrester configuration, with the letters corresponding to those in Fig. C.4a.

5 Discussion

5.1 Determination of the crack growth resistance

The crack growth resistance R is defined as, e.g. [C.33,C.34],

$$R = \frac{1}{B}\frac{d\left(A_{pl}+\Gamma\right)}{d\left(\Delta a\right)} \cong \frac{1}{B}\frac{dA_{pl}}{d\left(\Delta a\right)} \quad . \tag{C.8}$$

On the right hand side extension of Eq. (C.8) the small contribution of the surface energy Γ needed to create the new crack surfaces is neglected. Inserting the J-evaluation formula Eq. (C.5) into Eq. (C.8) yields a relation for the determination of the crack growth resistance from the J–Δa-curve valid for the SE(T) specimen,

$$R \cong \frac{b}{\eta}\frac{dJ_{pl}}{d(\Delta a)} + \frac{\gamma}{\eta}J_{pl} \quad . \tag{C.9}$$

The derivation is similar to that presented for C(T) and bend specimens in [C.33,C.35]. Since in most cases the second term on the right hand side of Eq. (C.9) is considerably smaller than the first term, the crack growth resistance is roughly proportional to the slope of the J–Δa-curve [C.33-C.35].

The difference in the slope of the J–Δa-curve of the single sheet specimen, which is similar to that of the CD configuration, and the CA configuration can be seen in Fig. C.4b. Table C.2 compares the average R-values determined from Eq. (C.9) of the single sheet material, the CD configuration, and the CA

configuration during the first crack extension stage between Points b and b' in Fig. C.4b.

Table C.2.

Average crack growth resistance (*R)* values determined from Eq. (C.9).

Specimen Configuration	*R* [kJ/m²]
Single Sheet	33.6
Crack divider	44,3
Crack arrester	73,7

5.2 The crack divider configuration

Fig. C.3 shows that the single layer specimen, with thickness $B = t$, and the multilayer specimen in crack divider (CD) configuration, with a total thickness $B = 5t$, have the same fracture initiation toughness J_{IC} and similar slope of the crack growth resistance curve (J–Δa-curve). The similarity in fracture initiation toughness was already reported in [C.4] and is not surprising as the fracture initiation toughness is, in general, only weakly dependent on the specimen geometry [C.2,C.34].

Table C.2 shows that the average R-value of the CD configuration is similar to that of the single sheet material. (Since the J–Δa-curves are not smooth, the small difference in R is not significant.) At a first glance, this seems to be in contrast to the results reported in [C.4] where an improvement of the crack growth resistance of multilayers in CD configuration was found, compared to the single sheet material. This is, however, not so:

The crack growth resistance R increases with decreasing specimen thickness B due to the effect of lateral contraction and since the formation of a shear-lip fracture surface requires more energy than that of a flat-fracture surface [C.36]. A thinner specimen has a smaller fraction of flat-fracture surface under predominant plane strain conditions and, therefore, a lower R than a thicker specimen. Due to the delamination of the weak interfaces upon loading, a 5-layer composite in CD configuration with a total thickness $B = 5t$ fractures in a similar way as five separate sheets of thickness t and, therefore, the crack growth resistance of the CD configuration will be similar to that of the single sheet material. This is what is observed in Fig. C.3 and Table C.2. If, however, a homogeneous single-sheet specimen with the same total thickness as the multilayer ($B = 5t$) were tested, a lower crack growth resistance would be expected, see Fig. C.5.

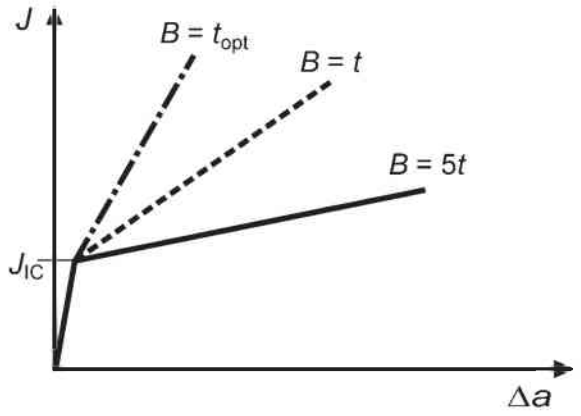

Fig. C.5 Schematics of the crack growth resistance curves of three single sheet specimens with different thickness *B*.

The highest crack growth resistance in the CD configuration is achieved, if the layers have a thickness where the fracture surfaces exhibit only shear-lip fracture and no flat-fracture regions. The optimum layer thickness t_{opt} can be estimated as twice the radius of the plastic zone under plane stress conditions [C.37]. By substituting the *J*-integral at the moment of fracture initiation, t_{opt} becomes

$$t_{opt} \cong 2r_y^{(pl\sigma)} \cong \frac{1}{\pi}\frac{J_{IC}E}{R_{p0.2}^2}. \qquad (C.10)$$

Inserting the mechanical properties of Al7075-T6 into Eq. (C.10) gives an optimum layer thickness $t_{opt} \approx 0.66$ mm, indicated by the dot-dash line in Fig. C.5. A further advantage of a reduced layer thickness is that the mechanical properties of aluminum sheets normally improve with decreasing thickness due to metallurgical reasons [C.38].

5.3 The crack arrester configuration

Several points are marked in the F–v_{LL}-curve and the corresponding J–Δa-curve of the tests in the CA configuration, Fig. C.4a and Fig. C.4b. The digital photographs taken at these points are collected in Fig 6. The unloaded sample is shown in Fig. C.6a, corresponding to Point a in Fig. C.4a. Crack growth is initiated at a load $F \approx 22$ kN (Point b in Fig. C.4a and C.4b). Fracture initiation is connected with a small load drop, and subsequently the crack grows in a stable manner, but rather quickly, into the first interlayer (Fig. C.6b and Point b' in Fig. C.4a). The measured fracture initiation value of J_c = 30 kJ/m² is significantly higher than that of the single sheet material or the CD configuration (8 kJ/m²). This difference is caused by the change of the crack growth direction with respect to the sheet orientation: In the CA configuration, crack growth occurs in

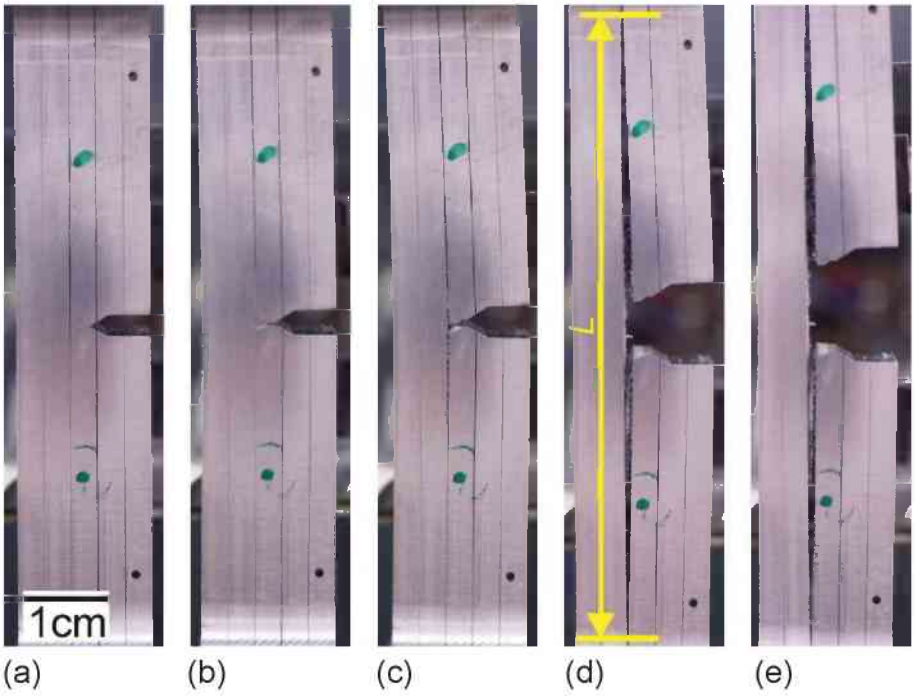

Fig. C.6 (a) Photograph of the CA specimen before loading. (b-e) Images of the opening crack showing extensive delamination, with the delamination length *L* shown in (d). The denomination of the pictures corresponds to the letters a-e in Fig. C.4a and Fig. C.4b.

the thickness direction of the sheets compared to the long transverse direction in the CD configuration, which can strongly alter the fracture initiation toughness [C.37].

The average *R*-values for the crack extension within the first, pre-fatigued sheet from Point b to b' in Fig. C.4b are significantly higher than that of the single sheet material or the CD configuration, Table C.2.

After fracture of the first pre-damaged layer, the crack arrests in the soft adhesive interlayer *without any delamination* (Fig. C.6b). This is in contrast to the classical weak interface effect where delamination occurs before the crack reaches the interface and crack arrest is a result of delamination, caused by the decrease in stress triaxiality and due to the blunt crack [C.3,C.9,C.38].

Upon further loading (Points c-e in Fig. C.4a) no crack growth from the interlayer into the remaining ligament can be observed, Fig. C.6 c-e. Only with increasing load, the soft interlayer, where the crack arrested, delamination occurs along the polymer/metal-interface, Fig. C.6c. This delamination seems to be caused by the lateral contraction of the sheets. It is difficult to determine the load where delamination starts exactly; it becomes visible at a load between F = 30 kN and 35 kN. At maximum load (Point d in Fig C.4a and Fig. C.6d), the complete length of the quadratic cross section of the specimen has delaminated. After reaching the maximum load, localized necking of the ligament starts, which leads to final fracture of the specimen.

The effectiveness of the introduction of soft interlayers in the CA configuration can be seen in the very steep slope of the J–Δa-curve in Fig.

C.4b. The J-values increase from 66 (± 18) kJ/m² in Point b' to a value at maximum load at Point d of $J_{F_{max}} \approx 10 \times 10^3$ (± 250) kJ/m², and further to the maximum observable J-value at Point e of $J_{max} \approx 13.7 \times 10^3$ (± 500) kJ/m². The latter value is 450 times higher than the fracture initiation toughness of the pre-cracked sheet J_c. A formal application of Eq. (C.9) would yield an extremely high value of crack growth resistance between Points c and d of the J–Δa-curve in Fig. C.4b, $R_{CA,c\text{-}d} \approx 3.5 \times 10^5$ kJ/m². Note that the significance of such a value is, however, very limited, since no physical crack extension occurs between Points c and e of the J–Δa-curve.

The toughness difference of the CA- and the CD configuration is clearly visible also, if the crack tip opening displacements (COD) of the specimens after final fracture are compared in Fig. C.7. For the CD configuration, as well as for the single sheet material, a COD of approximately 10 µm is measured after fracture, whereas a COD of more than 12 mm is determined from the pictures of the CA configuration.

We have seen that soft interlayers are extremely effective especially in the CA configuration with a much higher crack growth resistance than the CD configuration or the single sheet material. It should be noted that a third case could occur, denominated short-transverse configuration [C.38], where the crack propagates parallel to the weak interlayers. The fracture resistance will become very low, if the crack deviates from the nominal crack plane and grows into the soft interlayer. Crack path deviations for cracks parallel to interfaces were studied experimentally in [C.39,C.40]; a qualitative criterion for the deviation is given in [C.21]. It is clear that this case of crack extension has to be avoided in the application of such multilayered structures.

5.4 Estimates of the maximum load and J-values in the crack arrester configuration

A maximum applied load of F_{max} = 60 kN is measured at Point d, Fig. C.4a. This corresponds to a maximum nominal stress of the unbroken ligament of $\sigma_{max} = F_{max} / (B b_{arr}) = 578$ MPa, where b_{arr} denotes the ligament length after crack arrest (after crack growth through the first pre-fatigued Al-layer and through the adjacent adhesive layer). The value of σ_{max} is equal to the ultimate tensile strength R_m of the Al-alloy, see Table C.1. The fact that the maximum stress in the fracture mechanics test reaches the ultimate tensile strength of the alloy provides further evidence that the crack fully arrests at the first interlayer and the remaining ligament behaves like a tensile test of a sample without a pre-crack. The maximum load of the fracture mechanics test in the CA configuration can be simply estimated by the relation

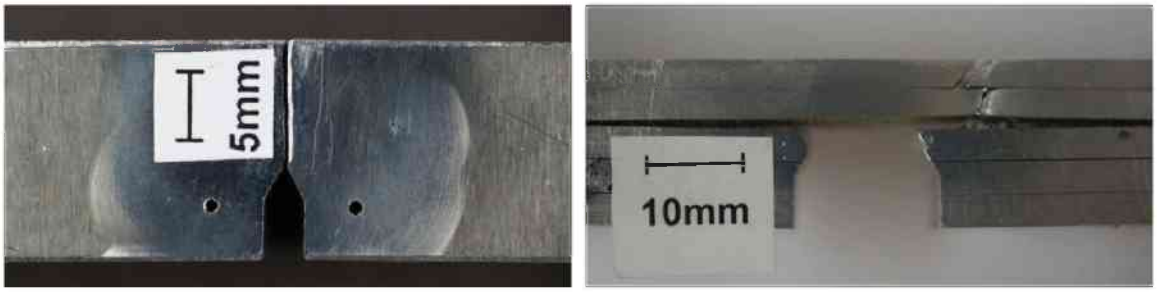

(a) (b)

Fig. C.7 Crack tip opening displacements of the specimens in (a) crack divider and (b) crack arrester configuration.

$$F_{max} = R_m B b_{arr} . \tag{C.11}$$

Since the thickness of the interlayers is small, b_{arr} approximately equals the sum of the thickness of the undamaged layers of bulk material, $b_{arr} \cong N_u t$, where N_u is the number of undamaged layers and t the layer thickness. Since the soft interlayer prevents an existing crack from growing into the neighboring layer of bulk material, the distance a crack can grow before being arrested in an interlayer should be as short as possible. Therefore, it is advantageous to decrease the layer thickness t and increase the number of layers in a composite, if for the bulk material a certain probability exists for the appearance of a crack in a given volume. It should be noted that a more sophisticated relation for the fracture stress in the tensile test and a design formula for an optimum multilayer architecture have been derived in [C.20] for linear elastic, brittle bulk materials.

In the following, a relation shall be derived for the maximum J-integral values. In order to do that, we assume the basic J-evaluation formula of the type

$$J = \frac{\eta^* A_{tot}}{Bb} , \tag{C.12}$$

where $A_{tot} = A_{el} + A_{pl}$ is the total energy supplied by the applied forces, i.e. the total area under the F–v_{LL}-curve, b is the current ligament length, and η^* is a nondimensional geometry factor, which is similar to η in Eq. (C.5) but takes into account also the elastic work. Again b_{arr} is inserted for b. Since the specimen deforms after crack arrest like a specimen in the tensile test, the total energy A_{tot} is estimated by the expression,

$$A_{tot} \approx R_m \varepsilon^* V \approx R_m \varepsilon^* B b_{arr} L . \tag{C.13}$$

In Eq. (C.13) σ_{UTS} is the ultimate tensile strength, and the term $\sigma_{UTS}\varepsilon^*$ is a critical strain energy density in a tensile test; $V = Bb_{arr}L$ is the deformed volume in the fracture mechanics specimen. The parameter ε^* is a critical total strain from the tensile test. Two different values can be inserted for ε^*: (1) the uniform strain ε_U should be taken for estimating the *J*-value at the maximum load of the fracture mechanics test, $J_{F_{max}}$ (Point d in Figs. C.4a and C.4b); (2) the technical fracture strain ε_F should be taken for an estimate of the maximum *J*-integral J_{max} (Point e in Figs. C.4a and C.4b). By inserting Eq. (C.13) in Eq. (C.12), we get estimates for the *J*-integral at the maximum load,

$$J_{F_{max}} = \eta R_m \varepsilon_U L\,, \tag{C.14}$$

and for the maximum possible *J*-integral,

$$J_{max} = \eta R_m \varepsilon_F L\,, \tag{C.15}$$

In Eq. (C.14) and Eq. (C.15), the geometry factor η^* is replaced by the geometry factor η for the evaluation of J_{pl}, Eq. (C.5). This can be done, since the elastic part of the strain energy density is small compared to the total strain energy density, see the stress–strain-curve of Fig. C.2. For the geometry of the arrested crack, η = 2.38.

The application of the estimation formulas gives $J_{F_{max}} \approx 10 \times 10^3$ kJ/m² and $J_{max} \approx 13.1 \times 10^3$ kJ/m². These values fit very well to the measured values, see Section 5.3.

Finally, it should be noted that the relations for the maximum fracture stress, Eq. (C.11), and for the maximum *J*-integral, Eq. (C.14) and Eq. (C.15), should be applied only for cases where the interlayers have significantly lower Young's modulus and yield strength than the bulk material.

6 Conclusions

In the current study the influence of compliant polymer interlayers on the fracture resistance of a high strength aluminum alloy is investigated. The main findings are:

- Since in the investigated case the layer thickness of the composite equals the thickness of the homogeneous bulk material, the crack divider (CD) configuration does not improve the crack growth resistance

compared to the homogeneous material. An estimate of the optimum layer thickness is given to achieve a high crack growth resistance.

- The composite in the crack arrester (CA) configuration shows higher fracture initiation toughness and crack growth resistance in the initial stage of crack extension, caused by the different orientation of the crack growth direction compared to the CD configuration. After growing into the first interlayer, the crack arrests completely and the crack growth resistance increases tremendously.
- The crack arrest in the compliant interlayer of the CA configuration originates from the material inhomogeneity effect, i.e. due to the (large) difference in elastic modulus and yield strength between bulk material and adhesive, and happens without any delamination.
- After the crack arrest, the unbroken ligament of the fracture mechanics specimen behaves like a tensile specimen. Delamination starts during load increase, caused by lateral contraction of the layers of the bulk material. Final fracture occurs when the nominal stress of the unbroken ligament reaches the ultimate tensile strength of the bulk material.
- Formulas are given in order to estimate the maximum load in the fracture mechanics test and the maximum *J*-integral in the CA configuration.

Acknowledgements

Financial support by the Austrian Federal Government and the Styrian Provincial Government within the research activities of the K2 Competence Center "Integrated Research in Materials, Processing and Product Engineering", under the frame of the Austrian COMET Competence Center Program, is gratefully acknowledged (Project A4.11 and A4.20).

References

[C.1] Lesuer DR, Syn CK, Sherby OD, Wadsworth J, Lewandowski JJ, Hunt WH. Mechanical behaviour of laminated metal composites. Int Mater Rev 1996;41:169–97.

[C.2] Anderson TL, Fracture Mechanics: Fundamentals and Applications, 3rd ed. Boca Raton: Taylor & Francis; 2005.

[C.3] Embury JD, Petch NJ, Wraith AE, Wright ES. The fracture of mild steel laminates. Trans Metall Soc AIME 1967;239:114–8.

[C.4] Taylor LG, Ryder DA. The fatigue and fracture toughness of laminated composites based on 7075-T6 aluminum alloy. Composites 1976;7:27-33.

[C.5] Argon AS, Im J, Safoglu R, Cavity formation from inclusions in ductile fracture. Metall Trans A 1975;6:825–37.

[C.6] Rice JR, Tracey DM. On the ductile enlargement of voids in triaxial stress fields. J Mech Phys Solids 1969;17:201–17.
[C.7] Alic JA, Danesh A. Fracture of laminates combining 2024-T3 and 7075-T6 aluminum alloys. Engng Fract Mech 1978;10:177–86.
[C.8] Kaufman JG. Fracture toughness of 7075-T6 and -T761 sheet, plate, and multi-layered adhesive bonded panels. J Basic Engng Trans ASME 1967;89:503–7.
[C.9] Cepeda-Jiménez CM, Alderliesten RC, Ruano OA, Carreño F. Damage tolerance assessment by bend and shear tests of two multilayer composites: Glass fibre reinforced metal laminate and aluminium roll-bonded laminate. Compos Sci Technol 2009;69:343–8.
[C.10] Alderliesten RC, Schijve J, Zwaag SVD. Application of the energy release rate approach for delamination growth in Glare. Engng Fract Mech 2006;73:697–709.
[C.11] Zak AR, Williams ML. Crack point singularities at a bi-material interface. J Appl Mech 30;1963:142–3.
[C.12] Cook TS, Erdogan F. Stresses in bonded materials with a crack perpendicular to the interface. Int J Eng Sci 10;1972;667–96.
[C.13] Gao H. Fracture analysis of nonhomogeneous materials via a moduli perturbation approach. Int J Solids Struct 1991;27:1663–1682.
[C.14] Muju S. Crack propagation in bimaterial multilayered periodically microcracking composite media. Compos Sci Technol 2000;60:2213–21.
[C.15] Fischer FD, Predan J, Fratzl P, Kolednik O. Semi-analytical approaches to assess the crack driving force in periodically heterogeneous elastic materials. Int J Fracture 2012;173:57–70.
[C.16] Maugin GA. Material forces: concepts and applications. ASME Appl Mech Rev 1995;48:213–45.
[C.17] Gurtin ME. Configurational forces as basic concepts of continuum physics. New York: Springer; 2000.
[C.18] Simha NK, Fischer FD, Kolednik O, Chen CR. Inhomogeneity effects on the crack driving force in elastic and elastic–plastic materials. J Mech Phys Solids 2003;51:209–40.
[C.19] Simha NK, Fischer FD, Kolednik O, Predan J, Shan GX. Crack tip shielding or anti-shielding due to smooth and discontinuous material inhomogeneities. Int J Fract 2005;135:73–93.
[C.20] Kolednik O, Predan J, Fischer FD, Fratzl P. Bioinspired design criteria for damage-resistant materials with periodically varying microstructure. Adv Funct Mater 2011;21:3634–41.
[C.21] Kolednik O. The yield-stress gradient effect in inhomogeneous materials. Int J Solids Struct 2000;37:781–808.

[C.22] Kolednik O, Predan J, Shan GX, Simha NK, Fischer FD. On the fracture behavior of inhomogeneous materials – A case study for elastically inhomogeneous biomaterials. Int J Solids Struct 2005;42:605–20.
[C.23] Kolednik O, Predan J, Fischer FD. Cracks in inhomogeneous materials: Comprehensive assessment using the configurational forces concept. Engng Fract Mech 2010;77:3611–24.
[C.24] Fratzl P, Gupta HS, Fischer FD, Kolednik O, Hindered crack propagation in materials with periodically varying Young's modulus – Lessons from biological materials. Adv Mater 2007;19;2657–61.
[C.25] Chen C , Pascual J, Fischer FD, Kolednik O, Danzer R. Prediction of the fracture toughness of a ceramic multilayer composite – Modeling and experiments. Acta Mater 2007;55:409–21.
[C.26] Suresh S, Sugimura Y, Tschegg E. The growth of a fatigue crack approaching a perpendicularly-oriented, bimaterial interface. Scripta Metall 27;1992:1189–94.
[C.27] Pippan R, Flechsig K, Riemelmoser FO. Fatigue crack propagation behavior in the vicinity of an interface between materials with different yield stresses. Mater Sci Engng A 2000;283:225–33.
[C.28] Sugimura Y, Lim PG, Shih CF, Suresh S. Fracture normal to a bimaterial interface: effects of plasticity on crack-tip shielding and amplifcation. Acta Metall Mater 43;1995:1157–69.
[C.29] Kolednik O, Predan J, Gubeljak N, Fischer FD. Modeling fatigue crack growth in a bimaterial specimen with the configurational forces model. Mater Sci Eng A 2009;519:172–83.
[C.30] Standard test method for measurement of fracture toughness. E-1820-08. Annual Book of ASTM Standards, Vol. 03.01, West Conshohocken: ASTM; 2008.
[C.31] Metallic materials – Unified method of test for the determination of quasistatic fracture toughness. ISO-12135-02. Geneva:ISO; 2002.
[C.32] Cravero S, Ruggieri C. Estimation procedure of *J*-resistance curves for SE(T) fracture specimens using unloading compliance. Engng Fract Mech 2007;74:2735–57.
[C.33] Kolednik O. On the physical meaning of the J–Δa-curves. Engng Fract Mech 1991;38:403–12.
[C.34] Kolednik O. Fracture mechanics. In: Nicolais L, Borzacchiello A, editors. Encyclopedia of Composites, Second Edition. Hoboken: John Wiley & Sons; 2012.
[C.35] Kolednik O. A simple model to explain the geometry dependence of J–Δa-curves. Int J Fract 1993;63:263–74.
[C.36] Stampfl J, Kolednik O. The separation of the fracture energy in metallic materials. Int J Fracture 2000;101:321–45.
[C.37] Irwin GR. Plastic zone near a crack and fracture toughness. In: Sagamore Research Conference Proceedings, Vol. 4; 1961.

[C.38] Herzberg RW. Deformation and fracture mechanics of engineering materials. New York: Wiley; 1976.

[C.39] Tschegg EK, Kirchner HOK, Schwalbe K-H. Cracks at interfaces of different cohesion. Acta Metall Mater 1993;41;2783–90.

[C.40] Tschegg EK, Kirchner HOK, Kocak M, Zelezny MF. Subinterfacial fracture in bimaterial joints. In: Schwalbe K-H, Kocak M, editors. Mismatching of Welds, ESIS 17, pp. 291–305. London: Mechanical Engineering Publications; 1994.

5.3.3 Multilayer with yield strength inhomogeneity: Al7075/Al1050

The results of the fracture mechanics tests on the roll-bonded multilayer specimens are presented and discussed here. The sample preparation and details on the experiments are given in Section 4.4. The discussed specimens have the same outer dimensions but the initial crack length is different, with a_0/W being 0.65 and 0.35 for Specimen 1 and Specimen 2, respectively.

Specimen 1

Fig. 5.2 shows a digital photograph of the pre-fatigued multilayer Specimen 1, with an initial a_0/W-ratio of 0.65, before testing. The initial pre-crack goes through three hard and two soft layers. The load–displacement-curve determined in the fracture mechanics test is plotted in Fig. 5.3. The letters a – e in Fig. 5.3 mark the points where photographs are taken during testing, which are collected in Fig. 5.4. A magnification of the crack tip area of the unloaded sample, Point a in Fig. 5.3, is shown in Fig. 5.4a. Crack growth initiates at a load of approximately 1 kN (Point b in Fig. 5.3 and Fig. 5.4b) in the hard layer and grows in a stable manner towards the interlayer, where no delamination is observed. At Point c in Fig. 5.3, see Fig. 5.4c, the crack reaches the hard/soft interface and arrests there. Delamination occurs in the crack tip area. Upon further loading, Points d – e in Fig. 5.3, the crack does not grow into the soft interlayer.

A maximum load of 2 kN is reached at Point d in Fig. 5.3, which corresponds to a stress of 585 MPa in the unbroken ligament area. The stress is calculated by dividing the applied load by the area of the unbroken ligament. The similarity of this value and the ultimate tensile strength of Al7075-T6, R_m = 585 MPa, shows that after crack arrest the ligament deforms like in a tensile test, as described in Sections 5.3.1 and 5.3.2. Localized necking starts upon further loading in the ligament area, which is clearly visible in Fig. 5.4d. Shortly after reaching Point e, the specimen fractures catastrophically.

A crack growth resistance curve is evaluated for the test, in the same manner as in Publication C, which is shown in Fig. 5.5. The letters in Fig. 5.5 correspond to those in Fig. 5.3 and the labels of the photographs in Fig. 5.4. A fracture initiation toughness of J_i = 26 kJ/m² is measured at Point b, which is in good accordance with the J_i-value of 30 ± 7 kJ/m² measured in the Al7075/Adhesive multilayers in the thickness direction of the sheets, see Publication C. After crack arrest the crack growth toughness rises steeply and reaches a value of J_{max} = 848 kJ/m² at Point e, which is more than 33 times higher than J_i.

Fig. 5.2 Photograph of Al7075/Al1050 fracture mechanics Specimen 1 in the unloaded state.

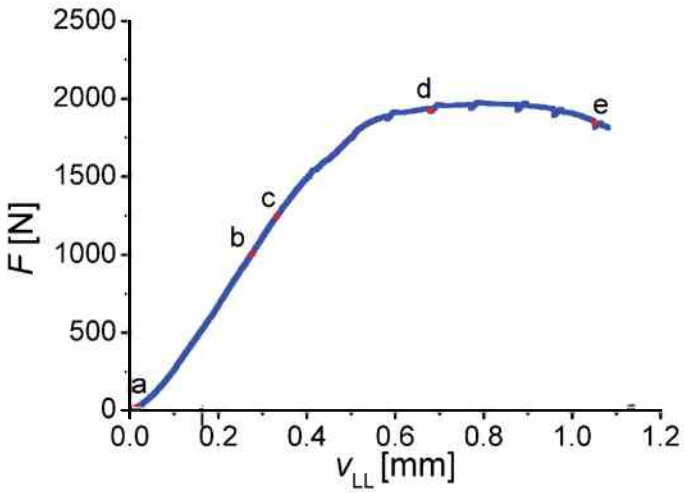

Fig. 5.3 Load–displacement-curve of the Al7075/Al1050 multilayer Specimen 1. The letters correspond to the labels of the photographs in Fig. 5.4.

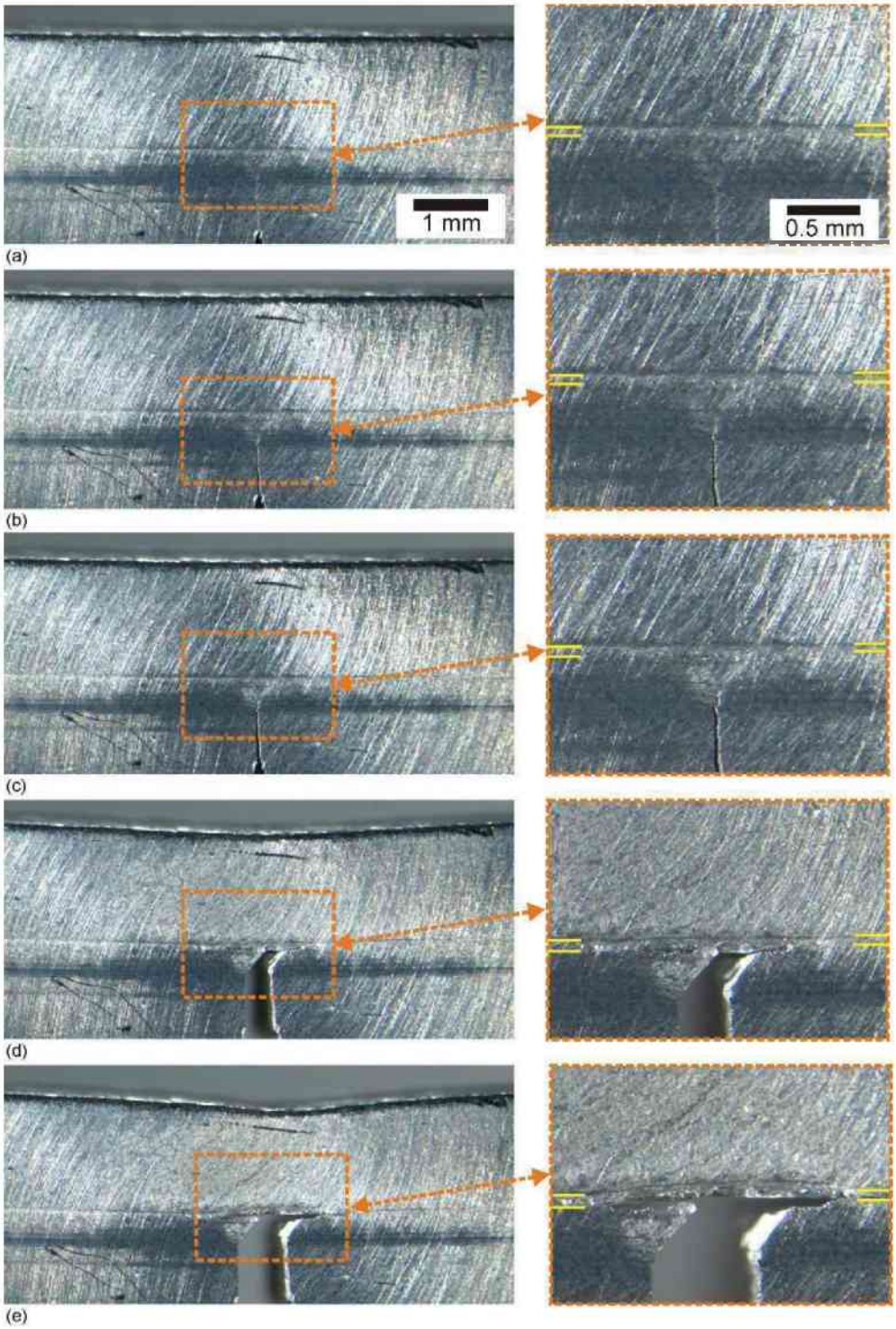

Fig. 5.4 Photographs of Al7075/Al1050 Specimen 1: (a) Unloaded state, (b) at fracture initiation, (c) after fracture of the pre-damaged layer, (d) at maxium load, (e) shortly before final fracture. Magnifications of the crack tip area are shown on the right side for each image; the interface positions are indicated by yellow lines. The labels correspond to the letters given in Fig. 5.3 and Fig. 5.5.

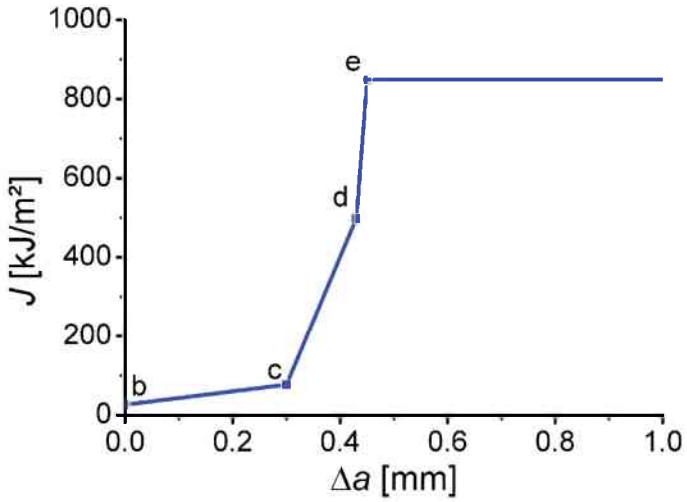

Fig. 5.5 Crack growth resistance curve for Al7075/Al1050 multilayer Specimen 1.

Specimen 2

A photograph of Specimen 2 is shown in Fig. 5.6. The initial crack length is 1.87 mm, resulting in an a_0/W-ratio of 0.35. The initial crack tip is located in the second hard layer, approximately 0.7 mm from the next soft interlayer. The load–displacement-curve of the fracture mechanics test is shown in Fig. 5.7. The letters a – e in Fig. 5.7 correspond to the labels of the images collected in Fig. 5.8. Upon loading of the specimen, fracture initiation occurs at a load of 3.5 kN, see Point b in Fig. 5.7 and Fig. 5.8b.

After fracture initiation, a load drop is observed. This load drop is caused by delamination of the soft/hard interface in front of the crack tip, which is clearly visible in Fig. 5.8c. Thereafter, the load increases again slightly until a second load drop occurs. Here, the pre-cracked Al7075-T6 layer fractures and the crack arrests at the hard/soft interface, which also delaminates, see Fig. 5.8d. The soft Al1050 interlayer is not fractured at this point and bridges the crack tip. The crack arrest in this specimen is not caused by the material inhomogeneity effect, which is the case for Specimen 1, but due to the delamination of the weak soft/hard interface, which causes crack deflection and blunting. A detailed description of these mechanisms is given in Section 1.2.1.

Between the points d – e in Fig. 5.7, the specimen deforms again like in a uniaxial tensile test. At Point 1 on the load–displacement-curve, the net stress in the ligament reaches the ultimate tensile strength of Al7075-T6. Thereafter, necking starts in the delaminated area and the soft interlayer fractures, see Fig. 5.8e. After reaching Point e in Fig. 5.7, the specimen fractures.

Also for this specimen a crack growth resistance curve was evaluated, which is shown in Fig. 5.9. The fracture initiation toughness J_i for this specimen is 25 kJ/m². The shape of the J–Δa-curve between points b and d, where delamination occurs is unknown and assumed to be linear here. A maximum crack growth toughness J_{max} = 900 kJ/m² is measured before final fracture occurs, being 36 times higher than J_i.

Fig. 5.6 Photograph of Al7075/Al1050 fracture mechanics Specimen 2 before testing.

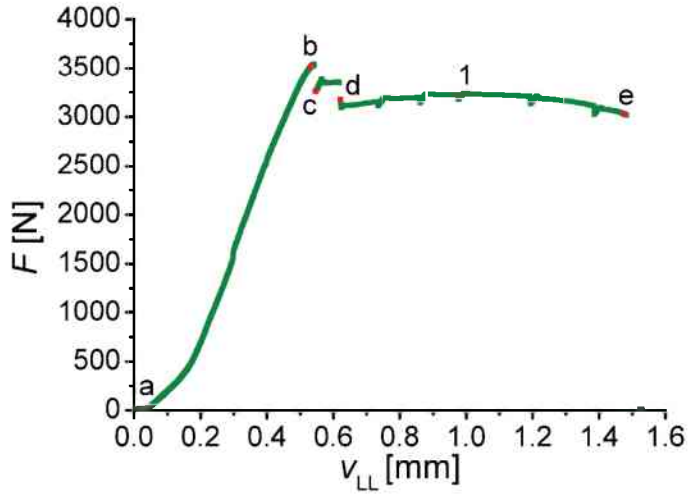

Fig. 5.7 Load–displacement-curve of Al7075/SS315 fracture mechanics Specimen 2. The letters given in the figure correspond to the labels of the photographs in Fig. 5.8.

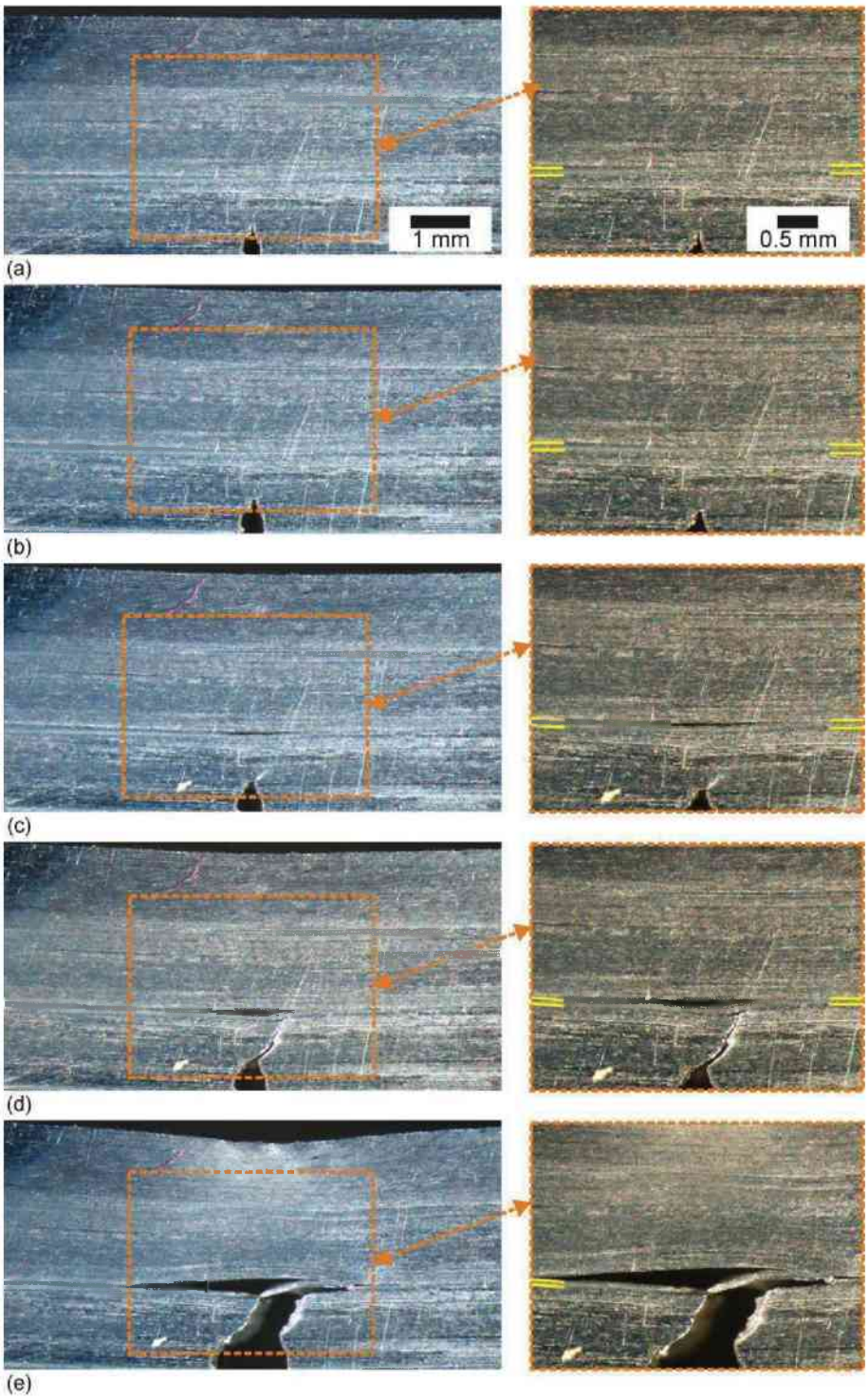

Fig. 5.8 Photographs of Al7075/Al1050 Specimen 2: (a) Unloaded state, (b) at maximum load where fracture initiation occurs, (c) after the first load drop, (d) after the second load drop, (e) before final fracture. Magnifications of the crack tip area are shown on the right side for each image; the interface positions are indicated by yellow lines. The labels correspond to the letters given in Fig. 5.7 and Fig. 5.9.

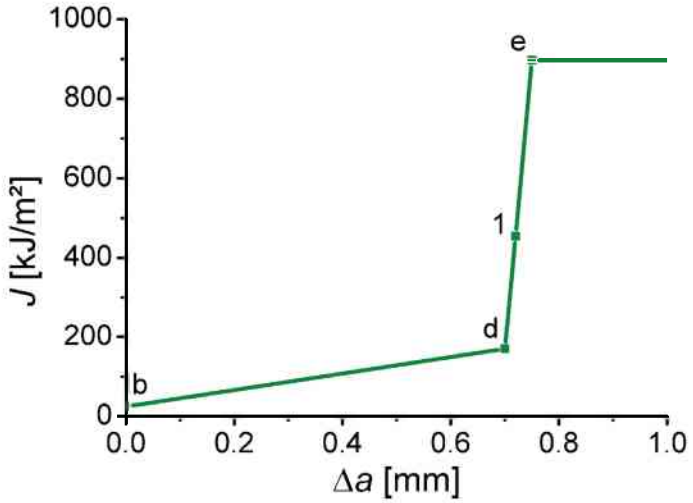

Fig. 5.9 Crack growth resistance curve of Al7075/Al1050 fracture mechanics Specimen 2.

Concluding remarks

The crack growth resistance curves of the two Al7075/Al1050 multilayer specimens are compared in Fig. 5.10. Crack growth starts at similar initiation toughness values of $J_i \approx 25$ kJ/m² for both specimens. It is interesting to note that there is no difference in J_i for the two specimens, although one was pre-fatigued and the other one only notched with a razorblade.

In Specimen 1, after fracture initiation the crack grows 0.3 mm through the first hard layer and arrests at the hard/soft interface. As delamination is observed in the vicinity of the crack tip at the hard/soft interface when the crack tip reaches it, it is unclear if the crack arrests due to the material inhomogeneity effect or due to delamination of a weak interface (see Section 1.2.1). Specimen 2 shows a different behavior at this stage of the test. Here delamination occurs at the soft/hard interface in front of the crack tip first and only thereafter the hard layer fractures and crack arrest occurs at the hard/soft interface. Here crack arrest is clearly caused by the delamination of a weak interface as described in Section 1.2.1.

A possible explanation for the difference in the material response could be locally weak bonding of the interlayer in Specimen 2. Local oxidation on the aluminum surface prior to roll bonding could promote delamination of the interlayers, as explained by Cepeda-Jimenez et al. in [72].

A comparison of the photographs in Fig. 5.4e and Fig. 5.8e reveals that approximately the same amount of soft/hard interface area delaminates and allows unconstrained plastic deformation of the undamaged ligament, as described above. As a consequence of this, both specimens reach comparable J_{max} values being more than 30 times higher than J_i.

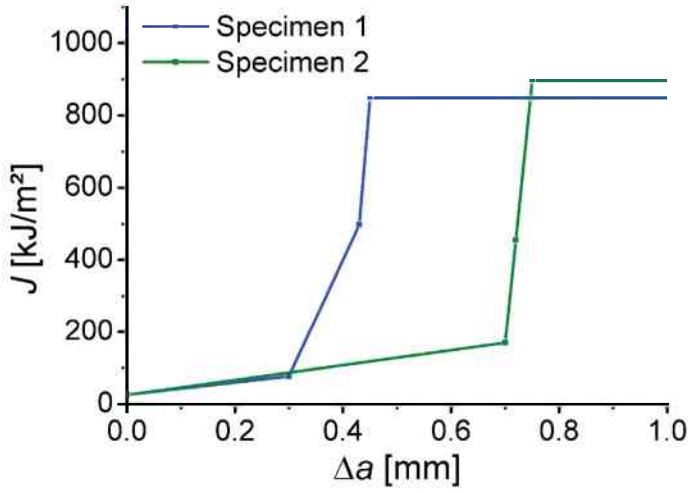

Fig. 5.10 Crack growth resistance curves of Al7075/Al1050 Specimens 1 and 2.

5.4 Summary of the fracture mechanics tests

Three multilayer systems, two showing an elastic inhomogeneity and one a yield strength inhomogeneity, are investigated with respect to their fracture resistance in this chapter. The first multilayer with an elastic inhomogeneity consists of a paper and air, the second of high strength aluminum connected with compliant adhesive layers. The multilayer with the yield strength inhomogeneity is a metal laminate composed of high strength and technically pure aluminum. The main findings of the investigations are:

- Independently of the system, the crack divider configuration shows similar crack growth resistance curves as the homogeneous materials. This is explained by the similarity of the prevailing stress state during the fracture mechanics test.
- An explanation on how an optimum layer thickness to achieve a maximum crack growth resistance could be found in the crack divider configuration is given in Publication C.
- For all multilayer systems the crack arrester configuration showed highly improved fracture toughness compared to the homogeneous materials. For both multilayers with elastic inhomogeneities this behavior is caused by the material inhomogeneity effect. The delamination of weak interfaces is responsible for crack arrest in Al7075/Al1050 Specimen 2. In Al7075/Al1050 Specimen 1 the mechanism causing crack arrest could not be uniquely identified, crack arrest due to delamination or the material inhomogeneity effect are possible.
- After fracture of the pre-damaged layers, all specimens in crack arrester configuration deform like tensile test samples in a uniaxial tensile test. Final fracture occurs when the ultimate tensile strength of the homogeneous material is reached.

- A simple formula was derived to estimate the maximum achievable *J*-integral J_{max} of multilayers in CA configuration. It was found that J_{max} depends on the mechanical properties of the material and the volume that can deform plastically, which roughly corresponds to the area where delamination occurs.

6

FATIGUE OF INHOMOGENEOUS MATERIALS

6.1 Preface

In Chapter 3 the influence of the material inhomogeneity effect on the local crack driving force in terms of the *J*-integral in a cracked structure is explained. As also fatigue crack propagation can be described by fracture mechanics, the aim of this chapter is to investigate the influence of the material inhomogeneity effect on fatigue crack propagation in multilayered materials.

Fatigue crack growth is often characterized by the crack growth rate d*a*/d*N* resulting from a given cyclic load at a certain crack length [15]. The most widely used of these fatigue crack growth models is Paris' law [73] of the form,

$$\frac{\mathrm{d}a}{\mathrm{d}N} = C\Delta K^{m}, \tag{6.1}$$

where C and m are factors depending on the material and the fatigue test parameters. The parameter ΔK is denoted stress intensity factor range and is defined as the difference between the stress intensity factors (see Eq. (2.7)) at maximum and minimum load, $K_{max} - K_{min}$.

The power relationship in Eq. (6.1) is violated at high ΔK values, where K_{max} approaches K_{IC} and at low ΔK values, where the crack growth rate decreases rapidly to zero at a certain positive, non-zero ΔK level. This lower limit of ΔK is denominated threshold stress intensity factor range ΔK_{th}, and usually defined at the point where the fatigue crack growth rate falls below one lattice spacing per cycle [74].

Fatigue cracks can close, i.e. the surfaces of the crack flanks come into contact, even at applied far-field tensile loads due to residual stress in the plastic wake of the crack. This effect, first described by Elber [75,76], is called plasticity-induced crack closure and has been found to influence the crack growth rate by altering the effective stress intensity range. The crack flanks open fully at a stress intensity factor K_{op}. According to Elber, fatigue crack propagation only occurs during the fraction of the cycle where the crack flanks are separated. Thus an effective stress intensity factor range ΔK_{eff} is defined as

$$\Delta K_{\text{eff}} = K_{\text{max}} - K_{\text{op}}, \tag{6.2}$$

which is controlling crack growth and depends on the stress ratio R, given by

$$R = \frac{K_{\text{min}}}{K_{\text{max}}}. \tag{6.3}$$

According to [75,76] K_{op} and ΔK_{eff} can be calculated by the empirical relations,

$$K_{\text{op}} = \left(0.5 + 0.1R + 0.4R^2\right) K_{\text{max}}, \tag{6.4}$$

and

$$\Delta K_{\text{eff}} = (0.5 + 0.4R)\Delta K_{\text{app}}. \tag{6.5}$$

The influence of the material inhomogeneity effect on the stress intensity factor and, consequently, on the stress intensity range, should be shown here for small scale yielding and plane stress conditions. Expressing the local stress intensity factor at the crack tip K_{tip}, in terms of the applied stress intensity factor K_{app} and the material inhomogeneity term C_{inh} yields,

$$K_{\text{tip}} = K_{\text{app}} \sqrt{1 + \frac{EC_{\text{inh}}}{K_{\text{app}}^2}}, \tag{6.6}$$

Assuming fatigue loading where $K_{max} >> K_{min}$, it is seen that the qualitative influence of C_{inh} on the stress intensity factor range is similar to that for fracture, compare Eq. (3.9), i.e. for a stiff/compliant or hard/soft transition an anti-shielding effect is expected and a shielding effect in the opposite case.

Fatigue tests are conducted on the Al7075/Adhesive and Al7075/Al1050 multilayer structures, which are described in Chapter 4.3.2 and tested with respect to their fracture toughness in Chapter 5. The tests are conducted at constant applied stress intensity ranges ΔK_{app}, i.e. the load is decreased with increasing crack length, and constant R = 0.1 for all tests. Reconsidering Eq. (6.1) shows that for a constant ΔK_{app}, da/dN also remains constant. Consequently, a change in da/dN at constant ΔK_{app} indicates a change in the local crack driving force ΔK_{tip}, due to the material inhomogeneity effect, see Eq. (6.3).

The main questions to be answered in this chapter are: How do interlayers with an elastic or yield strength inhomogeneity influence the fatigue crack propagation in multilayers, and what are the similarities and differences in the influence between the types of inhomogeneities?

6.2 Fatigue behavior of Al7075-T6

The Paris' law of homogeneous Al7075-T6 in longitudinal–long transverse direction was determined by Marissen [77] for R = 0.1 and 0.5 and is given by,

$$\frac{da}{dN} = 6.04 \times 10^{-7} \Delta K_{eff}^{3.215} . \qquad (6.7)$$

Eq. (6.5) is used to compare the crack growth rates of homogeneous Al7075-T6 with those of the tested multilayer structures, to determine the influence of the material inhomogeneity effect on the crack driving force for fatigue crack growth.

The effective threshold of fatigue crack propagation $\Delta K_{eff,th}$ for peak-aged Al7075 was determined by Pippan [78] for R = 0.1 and 0.7. A $\Delta K_{eff,th}$ of 0.85 MPa$\sqrt{m}$ was found for both stress ratios. In the same study similar $\Delta K_{eff,th}$ values were also found for several other aluminum alloys and technically pure aluminum.

6.3 Preliminary fatigue experiment on Al7075/Adhesive

A first fatigue experiment has been conducted by Jozef Predan at the University of Maribor on an Al7075/Adhesive multilayer specimen, consisting of 5 Al7075-T6 and 4 Al1050 layers, with the outer dimensions shown in Fig. 4.10. By machining two symmetrical notches into the two outer layers a double edge notch tension (DE(T)) specimen is produced, see Fig. 6.1. The specimen is cycled at constant load amplitude between 3 kN and 30 kN at a frequency of 15 Hz.

Fatigue crack growth through the notched outer layers within 4 x 10^4 cycles is observed during testing. Thereafter, the crack arrests in the interlayer or at an interface, which has not been monitored. Only after an additional 1.8 x 10^6 cycles, the crack re-initiates in a previously undamaged layer and leads to failure of this layer. With the applied load amplitude being constant, the applied stress intensity

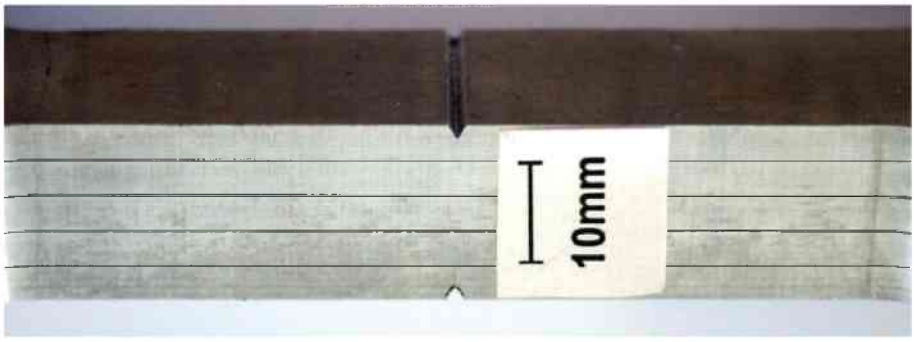

Fig. 6.1 Al7075/Adhesive DE(T) specimen.

range increases with crack extension, leading to the re-initiation and crack growth through the next undamaged layer within 4 x 10^4 cycles and failure of the last layer within an additional 200 cycles. Fig. 6.2 shows a photograph of the specimen after testing, where the numbers indicate the sequence in which the layers fractured. Re-initiation of fatigue crack growth in the previously undamaged layers takes place at locations remote from the initial notches, e.g. the location where layer 4 fails. Throughout the test no delamination is observed at the interfaces between the layers.

Fatigue failure of a homogeneous specimen of the same geometry, loading conditions and initial notch length would be expected after 10^5 cycles, which shows that the fatigue life of the structure was increased by a factor of nearly 19 by the introduction of the interlayers.

To gain a better understanding of the effects leading to crack arrest, further experiments are carried out in the current study at constant ΔK_{app} on Al7075/Al1050 specimens.

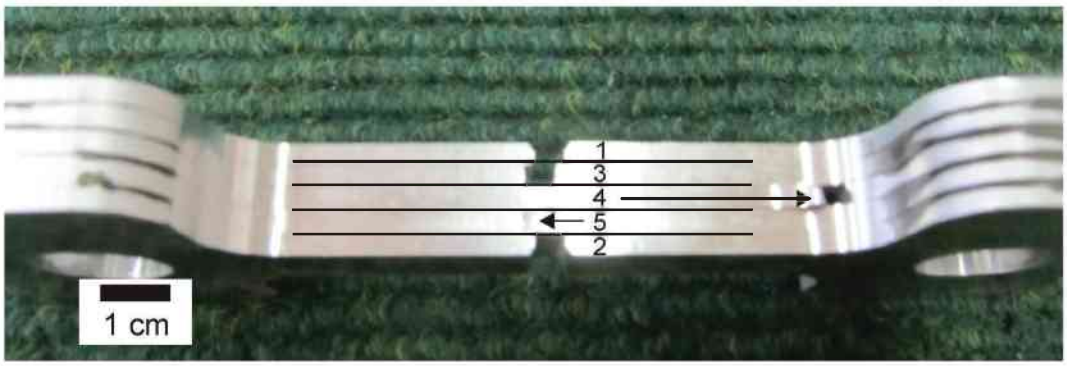

Fig. 6.2 Photograph of the Al7075/Adhesive DE(T) specimen after testing. The numbers indicate the sequence in which the layers fractured.

6.4 Multilayer with elastic inhomogeneity: Al7075/Adhesive

Two Al7075/Adhesive specimens are tested at a constant applied stress intensity range ΔK = 9 MPa$\sqrt{m}$ and R = 0.1. Specimen 1 consists of 5 Al7075-T6 and 4 adhesive layers and has the same single edge notch tension (SE(T)) geometry as the fracture mechanics specimens in CA configuration (see Fig. 4.12a), with W = B = 16.3 mm. Specimen 2 is smaller, consisting of only 2 Al7075-T6 layers of 2.47 mm thickness and 1 adhesive layer of 0.05 mm thickness. The outer dimensions, are identical to those of the Al7075/Al1050 fatigue test specimens, shown in Fig. 4.13, with W = 5 mm and B = 1 mm.

The fatigue tests are halted every 250 – 500 cycles to take photographs of the specimens with an optical microscope attached to the fatigue testing machine.

6.4.1 Results for Specimen 1

A digital photograph of Al7075/Adhesive Specimen1 before fatigue testing is shown in Fig. 6.3 and a magnification of the notch tip area can be seen in Fig. 6.4a. The initial notch length, including the razorblade cut, is 6.86 mm, resulting in an initial ligament length b = 9.44 mm. The first stiff/compliant interface, which lies at a crack length of 9.14 mm, lies 2.28 mm from the initial notch tip. The first interlayer has a thickness of 0.1 mm; therefore the first compliant/stiff interface is 2.38 mm from the notch tip, at a crack length of 9.24 mm.

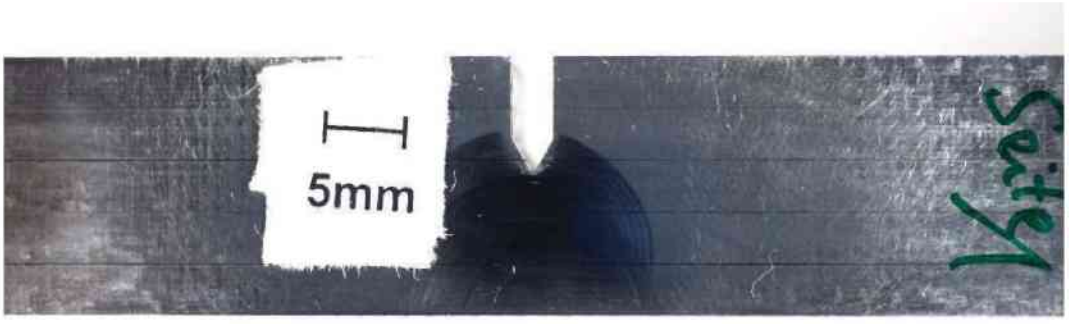

Fig. 6.3 Photograph of Al7075/Adhesive Specimen 1 before testing. A magnification of the notch tip is shown in Fig. 6.4a.

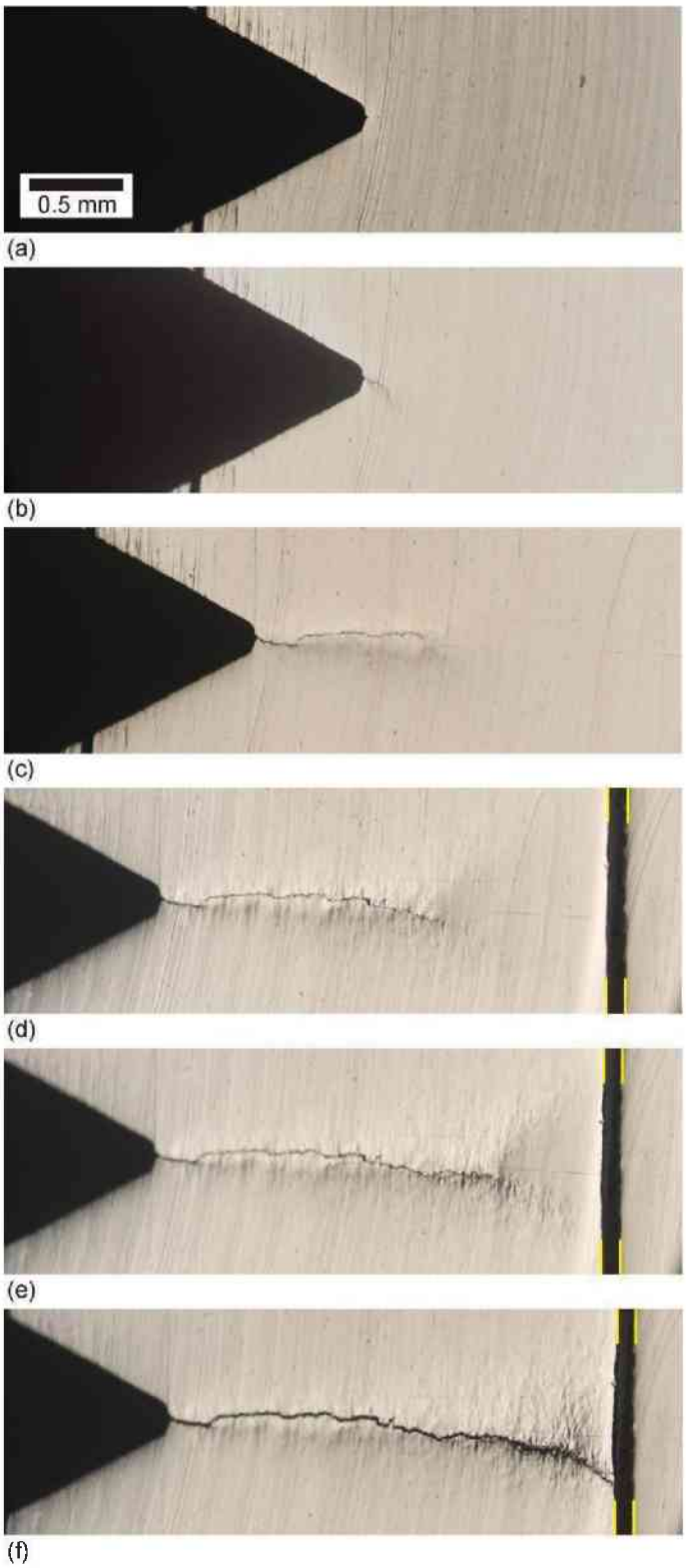

Fig. 6.4 Fatigue crack propagation in Al7075/Adhesive Specimen 1. (a) Before the test is started, (b) initiation of fatigue crack growth, (c-e) growth towards the interlayer, (f) growth into and through the interlayer, see Fig. 6.6. The investigated interlayer is marked by yellow lines.

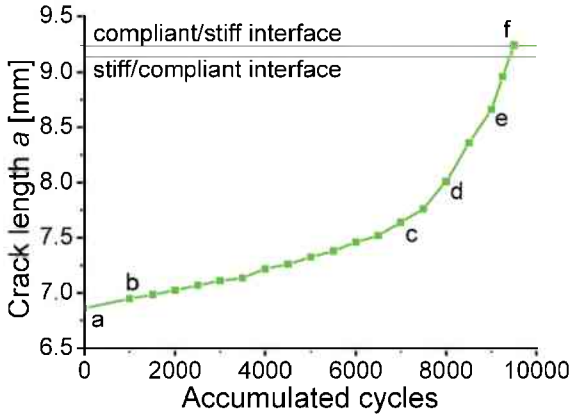

Fig. 6.5 Al7075/Adhesive Specimen 1. Crack length *a* vs. the total number of cycles. The letters correspond to the labels of the photographs in Fig. 6.4. The horizontal lines show the interlayer position.

After 1000 cycles at an applied ΔK of 9 MPa$\sqrt{m}$, the fatigue crack has grown 0.088 mm to a crack length of a = 6.948 mm, see Fig. 6.4b, which corresponds to an average crack growth rate da/dN = 8.8 x 10^{-5} mm/cycle. In Fig. 6.5, the crack length is plotted vs. the accumulated number of cycles. The rectangles show where images are taken during testing and the letters a-f indicate where the images a-f in Fig. 6.4 have been taken. The slope of the curve resembles the crack growth rate da/dN which increases with increasing steepness. For the first 4000 cycles the slope of the curve is relatively constant with an average da/dN of 9 x 10^{-5} mm/cycle. Thereafter da/dN increases strongly with the crack tip approaching the interface, reaching a maximum da/dN = 1.2 x 10^{-3} mm/cycle shortly before the stiff/compliant interface, which is shown by a horizontal line at a = 9.14 mm in Fig. 6.5. At point e in Fig. 6.5 the plastic zone in front of the crack tip, visible in Fig. 6.4e, reaches the stiff/compliant interlayer. In the area where the plastic zone interacts with the interlayer delamination occurs at the stiff/compliant interface. Within the next 500 cycles the crack grows through the remaining distance to the stiff/compliant interface, shown as a horizontal line at a = 9.14 mm in Fig. 6.5. Remote from the initial fatigue crack, a crack initiates and the interlayer fractures at the position marked by an arrow in Fig. 6.6. The crack stops at the compliant/stiff interface, symbolized by the horizontal line at a = 9.24 in Fig. 6.5. The position where the crack grows through the interlayer is not connected to the initial fatigue crack, therefore it is assumed that the crack in the adhesive is initiated when initial fatigue crack reaches the stiff/compliant interface. No delamination occurs at the compliant/stiff interface.

Fatigue crack growth from the notch tip through the first Al7075-T6 layer to the compliant/stiff interface, occurs within 9500 cycles, which results in an average da/dN of 2.5 x 10^{-4} mm/cycle.

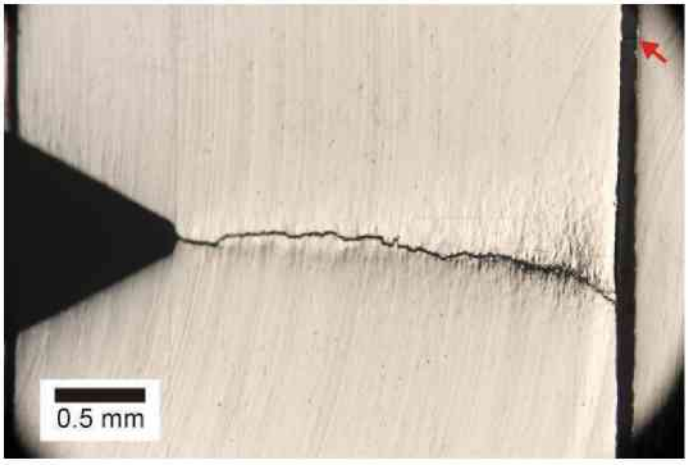

Fig. 6.6 Al7075/Adhesive Specimen 1. The specimen after fatigue crack growth through the compliant interlayer. The crack tip, located inside the interlayer is marked by an arrow.

After crack growth to the compliant/stiff interface, point f in Fig. 6.5, the specimen is cycled for an additional 4.8 x 10^6 cycles without any further crack growth or delamination at the interfaces. Taking into account the resolution of the microscope, which is approximately 1 µm, it can be concluded that the crack stopped at the interface, as a crack growing with a rate of one lattice spacing per cycle would be detected.

Fig. 6.7 shows a graph where the crack growth rate d*a*/d*N*, equaling the slope of the curve in Fig. 6.5, is plotted at a logarithmic scale vs. the distance of the crack tip to the stiff/compliant interface *d*, which is symbolized by a vertical grey line at *d* = 0 mm. The second vertical grey line indicates the location of the compliant/stiff interface. The letters in the graph again correspond to the labels of the images in Fig. 6.4. The solid green line shows in which interval the crack propagates at a certain d*a*/d*N*, e.g. the crack grows from point a to point b at a rate of 8.8 x 10^{-5} mm/cycle. The green squares give the average crack tip position and crack growth rate for each interval of crack growth. It has to be noted that the same input data are used to plot Fig. 6.5 and Fig. 6.7 and only the layout of the graphs varies. The data of all subsequent fatigue tests will be presented in d*a*/d*N* vs. distance to the stiff/compliant interface (d*a*/d*N*–*d*-) plots.

Fig. 6.7 clearly shows that d*a*/d*N* increases constantly starting at a distance *d* = –1.6 mm. A maximum d*a*/d*N* = 1.2 x 10^3 mm/cycle is reached near the interface, which is14 times higher than the initial d*a*/d*N*. At point f d*a*/d*N* drops to zero upon the crack arrest at the compliant/stiff interface.

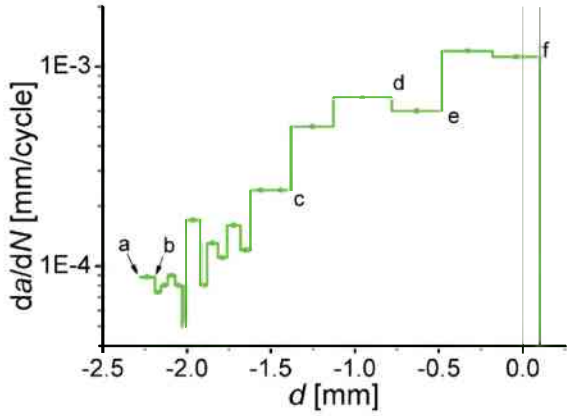

Fig. 6.7 Al7075/Adhesive Specimen 1. Crack growth rate d*a*/d*N* vs. distance to the stiff/compliant interface. The letters correspond to the letters in Fig. 6.5 and the labels of the photographs in Fig. 6.4.

6.4.2 Results for Specimen 2

Specimen 2 consists of two Al7075-T6 layers of approximately 2.47 mm thickness bonded with one 0.05 mm thick SS315 layer, resulting in a width W = 5 mm. The initial crack length is a = 0.57 mm and the initial d = –1.68 mm. Fig. 6.8 shows a photograph of the area around the notch tip before the test is started. Images of the fatigue crack propagating through the first stiff layer into the interlayer are collected in Fig. 6.9. The labels of the photographs correspond to the letters in Fig. 6.10, where they mark the positions where the images are taken.

The average d*a*/d*N* for the first steps of crack extension is 1 x 10^{4} mm/cycle. Approximately 1.5 mm before the interface, d*a*/d*N* increases strongly, reaching a maximum d*a*/d*N* of 1.6 x 10^{-3} mm/cycle before entering the interlayer. No delamination at the interfaces is visible before the fatigue crack reaches the interlayer.

Fig. 6.8 The notch tip area of Al7075/Adhesive Specimen 2 with the interlayer at 0.5*W*. The interlayer location is marked by yellow lines.

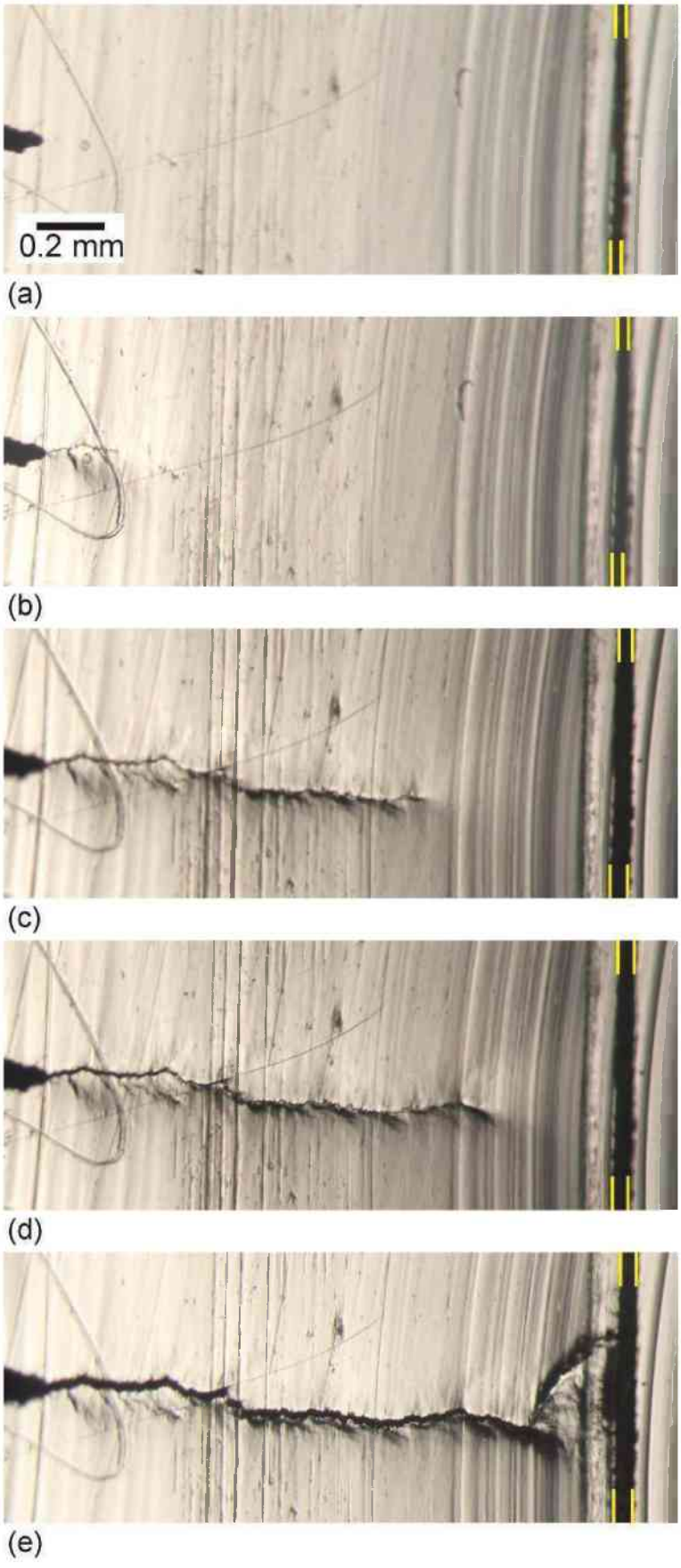

Fig. 6.9 Fatigue crack growth in Al7075/Adhesive Specimen 2. (a) Before testing, (b-d) fatigue crack propagation towards the interlayer, (e) growth into the interlayer. The interfaces are marked by yellow lines.

Fatigue crack propagation through the first Al7075-T6 layer needs 3250 cylces. After crack growth into the interlayer, the fatigue test is continued for 5 x 10^5 cycles, where final failure of the specimen occurs. Within these 5 x 10^5 cycles the fatigue crack re-initiates remote from the initial fatigue crack and leads to failure of the specimen. The location where the fatigue crack re-initiates and propagates through the second Al7075-T6 layer is shown in Fig. 6.11.

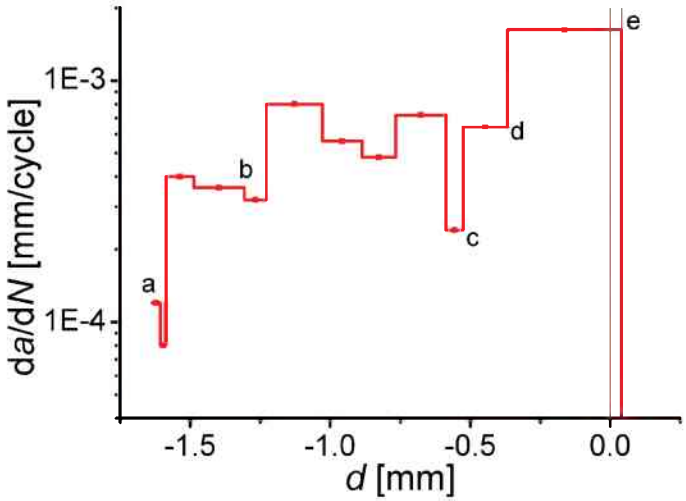

Fig. 6.10 Crack growth rate vs. distance to the stiff/compliant interface for Al7075/Adhesive Specimen 2.

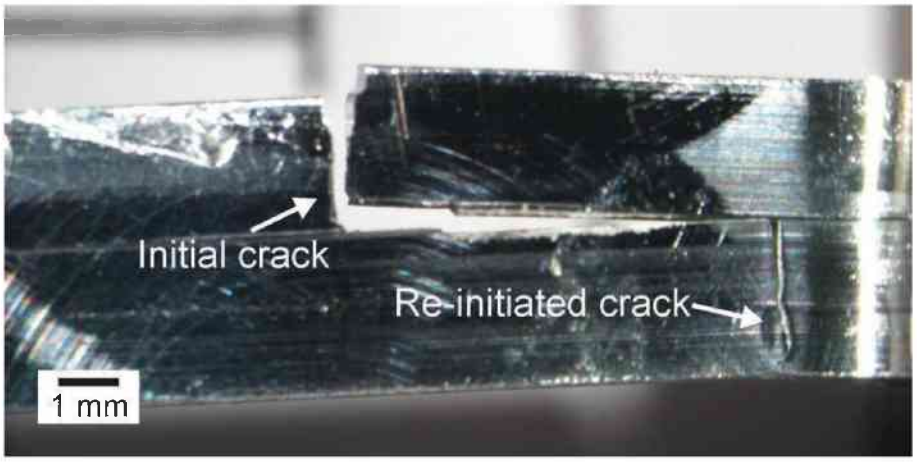

Fig. 6.11 Al7075/Adhesive Specimen 2 after re-initiation of fatigue crack growth in the second stiff layer.

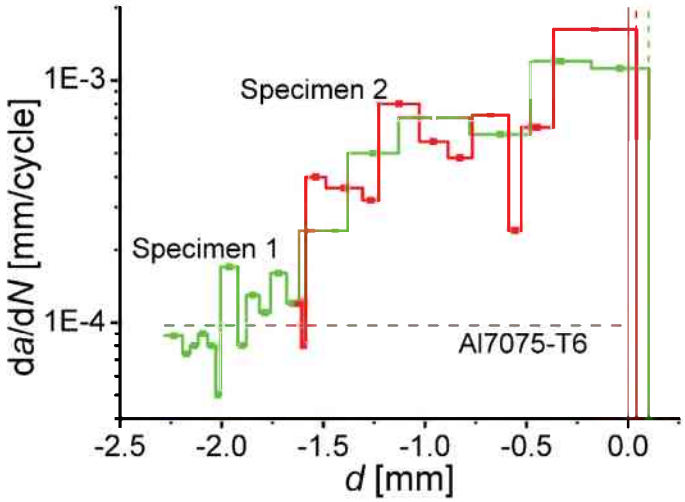

Fig. 6.12 Al7075/Adhesive specimens: Comparison of the crack growth rate vs. distance to the stiff/compliant interface data.

6.4.3 The material inhomogeneity effect in fatigue of multilayers with an elastic inhomogeneity

The crack growth rate vs. distance to the stiff/compliant interface (d*a*/d*N*–*d*) data of the two specimens are compared in Fig. 6.12. Additionally, d*a*/d*N* calculated for ΔK_{app} = 9 MPa√m and R = 0.1, which corresponds to ΔK_{eff} = 4.86 MPa√m (see Eq. (6.6)) according to Eq. (6.5), is plotted as a horizontal dashed grey line in Fig. 6.12. For ΔK_{app} = 9 MPa√m a d*a*/d*N* of 9.74 x 10^{-5} mm/cycle is calculated.

It can be seen that for the first intervals of crack extension, for d < –1.5 mm, the experimental data and those calculated according to Eq. (6.5) are in good accordance. Thus it can be concluded that the material inhomogeneity effect does not influence the crack driving force at that stage and $\Delta K_{app} = \Delta K_{tip}$.

In both specimens d*a*/d*N* increases strongly for d > –1.5 mm. The maximum crack propagation rates in the vicinity of the interlayer are 12 and 16 times higher than that for the homogeneous material for Specimen 1 and Specimen 2, respectively. This pronounced increase in d*a*/d*N* for a constant ΔK_{app} can be attributed to the anti-shielding effect caused by the strong elastic inhomogeneity between Al7075-T6 and the adhesive, visible in the Dundurs parameter of –0.99, see Section 4.3.2. This anti-shielding effect is detrimental to the fatigue life.

For both specimens fatigue crack growth stops at the compliant/stiff interface after propagation into the adhesive interlayer. This originates from the material inhomogeneity effect, which reduces the local crack driving force and leads to the strong shielding effect, see Chapter 3. The shielding effect leads to crack arrest at the interface and necessitates a re-initiation of crack growth in the hard layer for further crack propagation. No delamination at the

compliant/stiff interfaces is seen upon crack arrest, which allows the conclusion that not the mechanisms of crack deflection and crack blunting, see Section 1.2.1, are responsible for stopping the fatigue crack.

For a homogeneous specimen of the same geometry as Specimen 1, with initial ligament length b = 9.44 mm, and ΔK_{app} = 9 MPa√m, final failure of the specimen would occur after approximately 10^5 cycles, which can be estimated by rearranging Eq. (6.5). Nevertheless, sample 1 did not show any signs of re-initiation of fatigue crack growth after the additional 4.6 x 10^6 cycles, after which the test was stopped. This allows the conclusion that the material inhomogeneity effect caused by the introduction of 2 % compliant adhesive into the high strength aluminum alloy leads to a prolongation of the fatigue lifetime of at least 46 times in the CA configuration in Specimen 1. A similar estimation for Specimen 2 gives that the fatigue life of the specimen is prolonged by a factor 11, before final failure occurs. A detailed examination of the area where re-initiation of fatigue crack growth occurred shows that a shallow notch was introduced during machining, which facilitated the initiation of a new fatigue crack. Nevertheless, the strong improvement of the fatigue lifetime due to the introduction of the compliant interlayer is also clearly visible in Specimen 2.

Concludingly it can be remarked that the resistance to fatigue damage in multilayered structures with an elastic inhomogeneity is highly improved to that of a homogeneous material due to the material inhomogeneity effect, although only 2 % of the compliant phase are introduced.

6.5 Multilayer with yield strength inhomogeneity: Al7075/Al1050

Fatigue tests on multilayers with similar Young's moduli but a difference in the yield strength are carried out at constant ΔK_{app} = 5 MPa√m, 9 MPa√m, 12 MPa√m and 18 MPa√m with R_{app} = 0.1. Specimens of the geometry described in Chapter 4.3.2 are used, which consist of 4 hard Al7075-T6 and 3 soft Al1050 layers. In these tests, crack extension is measured on both specimen surfaces, therefore separate da/dN–d-graphs are subsequently shown for both specimen sides.

The following sections present the results of the fatigue tests of the different ΔK_{app} values, which are subsequently discussed and compared in Section 6.5.5.

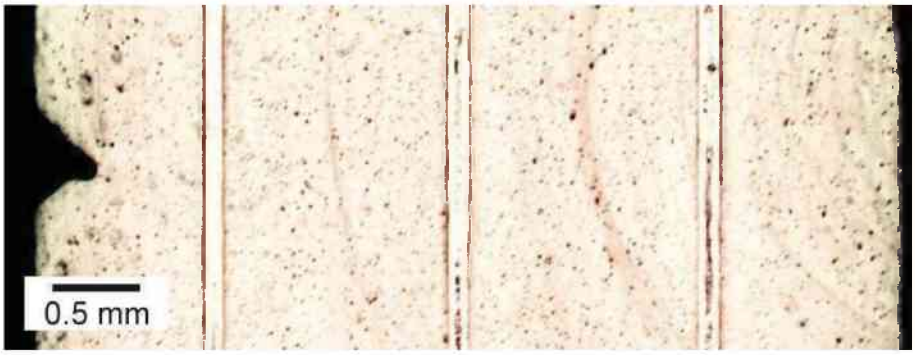

Fig. 6.13 LM-micrograph of Specimen 1–$\Delta K5$ before testing.

6.5.1 ΔK_{app} = 5 MPa$\sqrt{m}$

A light-optical microscope (LM-) micrograph of one specimen subjected to cycling at the lowest applied stress intensity range ΔK_{app} = 5 MPa$\sqrt{m}$, denominated Specimen 1-$\Delta K5$, is shown in Fig. 6.13. The da/dN–d-plots for crack growth towards the middle interlayer on specimen sides 1 and 2 are given in Fig. 6.14. The hard/soft interface is shown as a vertical grey line at d = 0 mm; the second vertical grey line at d ≈ 0.125 mm symbolizes the soft/hard transition. Additionally, the average da/dN values in the hard and soft layers are shown as dash-dot lines and the da/dN of homogeneous Al7075-T6, calculated according to Eq. (6.5), as horizontal dashed grey lines.

Fig. 6.14 shows that da/dN inside the hard layer remains constant on both sides at an average da/dN = 7.5 x 10^{-6} mm/cycle, which is half the da/dN predicted by Eq. (6.5) being 1.47 x 10^{-5} mm/cycle. No significant increase in da/dN is observed when the crack approaches the soft interlayer.

On both sides the crack propagates through the hard/soft interface into the Al1050 interlayer without any or only very little delamination, see the SEM pictures in Fig. 6.15. The average crack growth rate in the Al1050 interlayer is da/dN = 1.5 x 10^{-6} mm/cycle, which is 5 times lower than that in the hard phase.

Although the crack growth rate is decreased in the interlayer, the fatigue crack does not stop but propagates through the soft/hard interface into the next Al7075-T6 layer, where da/dN increases again, see Fig. 6.14a. Dividing the total crack extension Δa of the test by the total number of cycles performed in the test gives an average crack growth rate da/dN_{tot} which includes the influence of the interlayer. For this test da/dN_{tot} = 5.95 x 10^{-6} mm/cycle, which is 20 % lower than the average da/dN observed in the hard Al7075-T6.

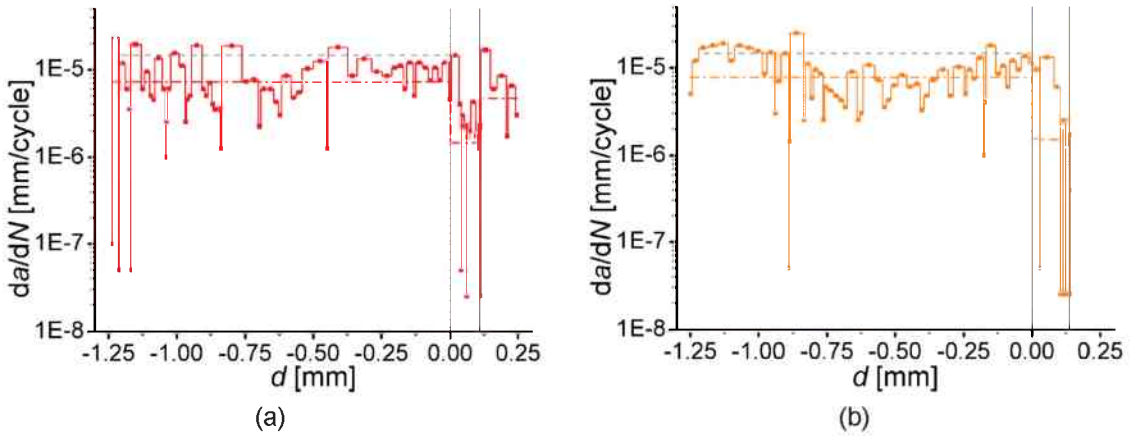

Fig. 6.14 Specimen 1–$\Delta K5$: Crack growth rate vs. distance to the hard/soft interface curves for the specimen side 1 (a) and side 2 (b) tested at ΔK = 5 MPa$\sqrt{m}$.

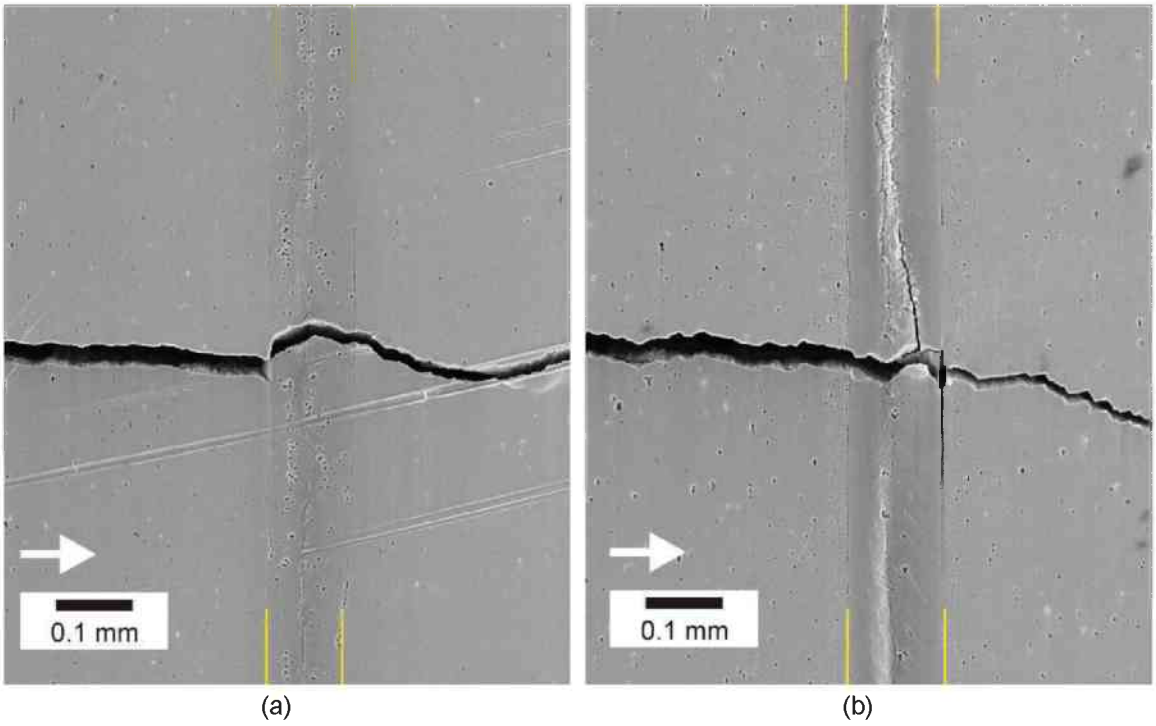

Fig. 6.15 Specimen 1–$\Delta K5$: SEM pictures of side 1 (a) and side 2 (b) of the investigated interlayer. The arrows mark the crack growth direction and the yellow lines indicate the location of the interfaces.

The d*a*/d*N*–*d*-plot of one side of a second specimen, denominated Specimen 2-$\Delta K5$, tested with the same ΔK_{app} and R is shown in Fig 6.13a. Specimen 2-$\Delta K5$ shows a very similar behavior to the one discussed above, see Fig. 6.16b. An SEM image is shown in Fig. 6.17a which shows crack propagation into the interlayer, happening without delamination, and crack growth out of the interlayer. A magnification of the interlayer area shown in Fig. 6.17a is shown in Fig. 6.17b, where the location of the fatigue crack tip after growing through the soft/hard interface is indicated by an arrow.

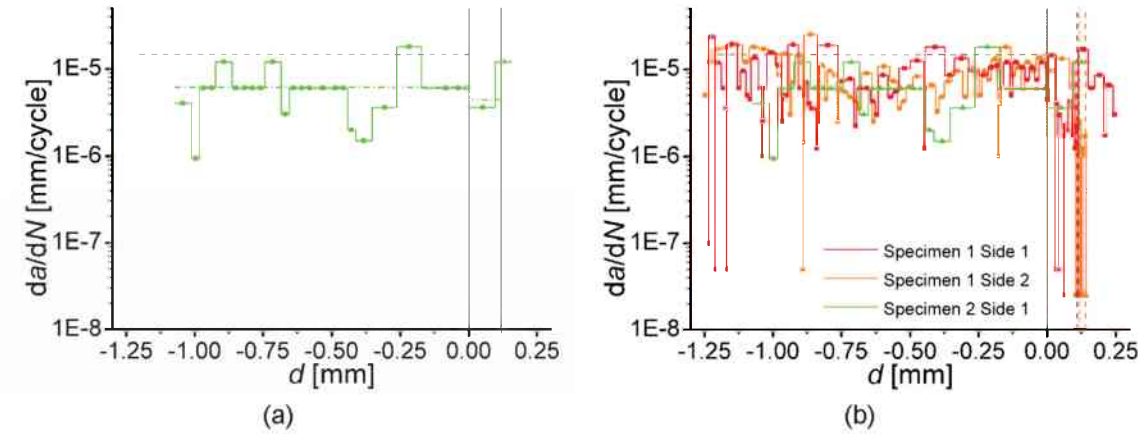

Fig. 6.16 Crack growth rate vs. distance to the hard/soft interface for the Specimen 2–$\Delta K5$ (a) and comparison of the curves of the two specimens tested at ΔK = 5 MPa$\sqrt{m}$ (b).

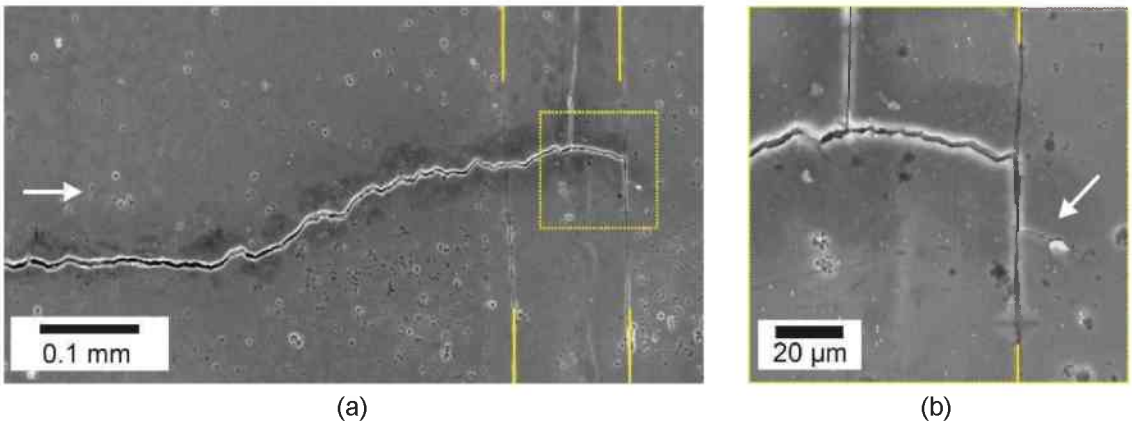

Fig. 6.17 Specimen 2–$\Delta K5$: (a) SEM image of the fatigue crack growing through the interlayer. The area marked by the yellow square is magnified in (b).

In Fig. 6.15b, Fig. 6.17a and Fig. 6.17b fatigue cracks propagating perpendicular to the initial fatigue crack growth direction are visible. These cracks do not form at the interfaces but in the middle of the soft interlayers.

6.5.2 ΔK_{app} = 9 MPa√m

Fig. 6.18 shows the first two interlayers in front of the initial notch of Specimen 1-ΔK9 tested at ΔK_{app} = 9 MPa√m with R = 0.1. The da/dN–d-plots for crack growth towards the second interlayer are shown in Fig. 6.19.

On side 1 the fatigue crack propagates towards the interlayer with an average da/dN = 9.92 x 10^{-5} mm/cycle. This is in good accordance with da/dN = 9.74 x 10^{-5} mm/cycle, calculated for homogeneous Al7075-T6 for ΔK_{app} = 9 MPa√m. For -0.15 mm < d < 0 mm an increase in da/dN is observed, with a maximum value of 2.64 x 10^{-4} mm/cycle. Inside the soft interlayer, the crack growth rate decreases by a factor of 15 compared to the homogeneous material, to an average da/dN of 6.45 x 10^{-6} mm/cycle.

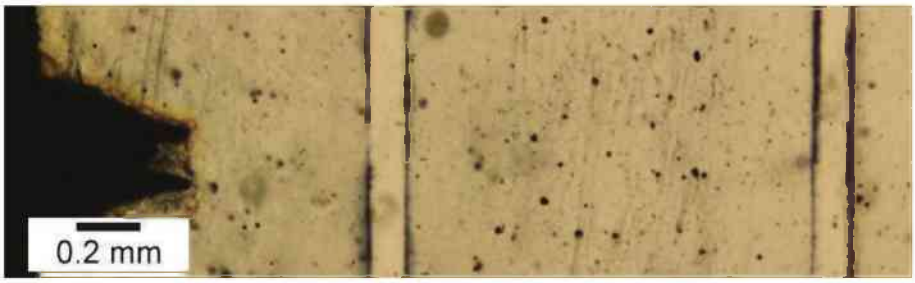

Fig. 6.18 The initial notch and the first two interlayers of Specimen 1–ΔK9 before testing.

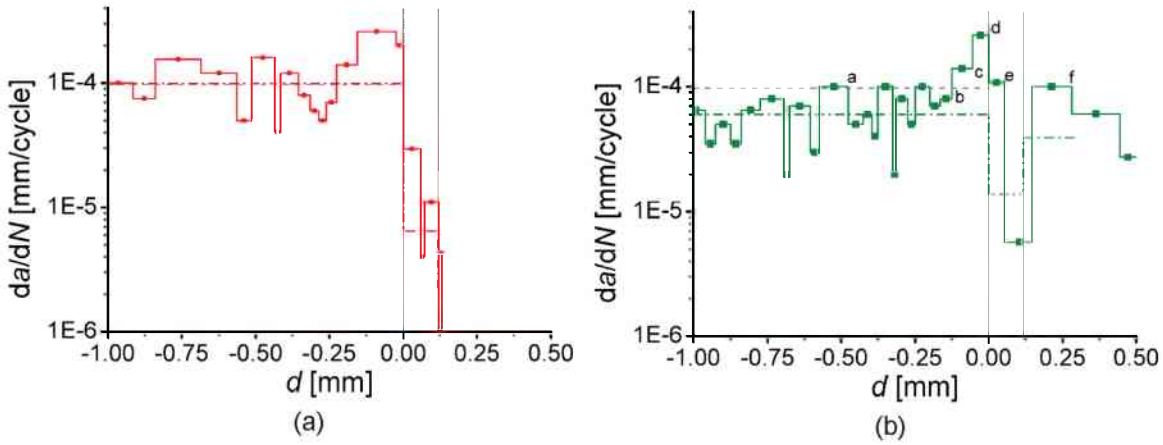

Fig. 6.19 Specimen 1–ΔK9: Crack growth rate vs. distance to the hard/soft interface curves for side 1 (a) and side 2 (b). The letters in (b) correspond to the labels of the photographs in Fig. 6.22.

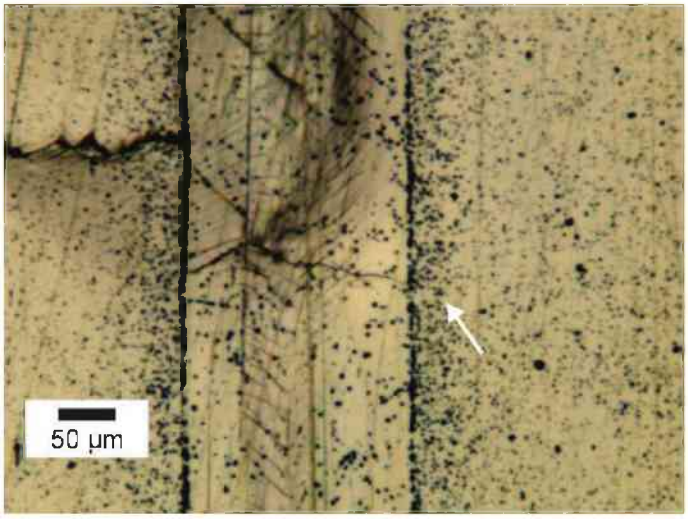

Fig. 6.20 Specimen 1–ΔK9: LM-micrograph of the fatigue crack growing through the soft interlayer on side 1.

The retardation of crack growth inside the interlayer might be promoted by delamination of the hard/soft interface and bifurcation of the crack inside the pure aluminum, see Fig. 6.20. Despite the strong retardation, the crack is not arrested in the interlayer, but grows through the soft/hard interface remote from the initial crack into the next Al7075-T6 layer without any delamination at the second interface. The fatigue crack tip after crack growth through the second interface is marked with an arrow in Fig. 6.20.

On the second side of Specimen 1-ΔK9, Fig. 6.19b, the average da/dN is 6 x 10^{-5} mm/cycle in the first hard layer, which is nearly 40 % slower than the value estimated according to Eq. (6.5) for d < -0.1 mm. For -0.1 mm < d < 0 mm da/dN increases to a maximum of 2.6 x 10^{-4} mm/cycle, which is similar to the maximum seen on side 1. Inside the interlayer the average da/dN = 1.39 x 10^{-5}, corresponding to a 20 % decrease compared to the average rate in Al7075-T6. Unlike on side 1, the fatigue crack propagates through the soft interlayer without pronounced bifurcation and grows through the soft/hard interface without any delamination. A SEM image and a photograph of the soft interlayer after stopping the test are shown in Fig. 6.21. Propagation in the second hard layer takes place at a similar rate as in the first hard layer.

For this test da/dN_{tot} = 3.45 x 10^{-5} mm/cycle, which is a reduction of 60 % compared to the average da/dN in Al7075-T6 for the applied ΔK.

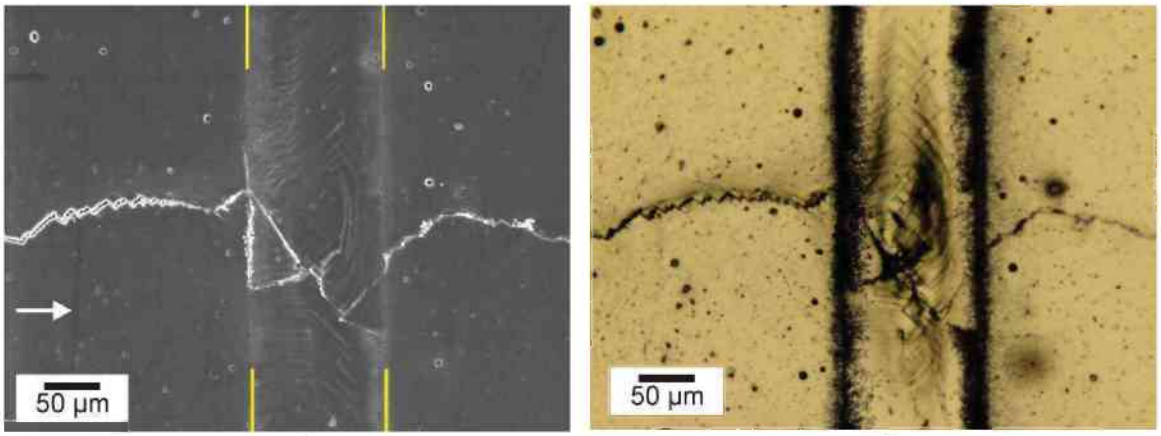

Fig. 6.21 Specimen 1–ΔK9: (a) SEM image and (b) photograph of the soft interlayer on side 2 after stopping the fatigue test. The fatigue crack growth direction is indicated by an arrow in (a).

Fig. 6.22 shows a series of photographs during the experiment. The labels of the images correspond to letters given in Fig. 6.19b. In Fig. 6.22a the crack is 480 µm from the hard/soft interface and no deformation inside the interlayer is visible. Also in Fig. 6.22b, where d = –125 µm, no deformation in the interlayer can be seen. For the crack advancing closer to the interlayer, the formation of a plastic zone inside the interlayer is visible, see Fig. 6.22c. In this interval of crack growth, between points b and c in Fig. 6.19b, the first increase in da/dN is observed. Thereafter the crack grows into the interlayer, Fig. 6.22d and Fig. 6.22e, in which the plastic zone is constrained. Crack growth through the soft/hard interface into the second hard layer is clearly visible in Fig. 6.22f.

The photographs in Fig. 6.21b and Fig. 6.22 also show that an exact fatigue crack length measurement inside the interlayer using an optical microscope is complicated and sometimes impossible due to the formation of the plastic zone inside the Al1050 interlayer. Therefore, the use of a SEM to regularly control the crack path is recommended for detailed analysis of the crack path. Nevertheless, the use of the SEM has the drawback that it is very time consuming.

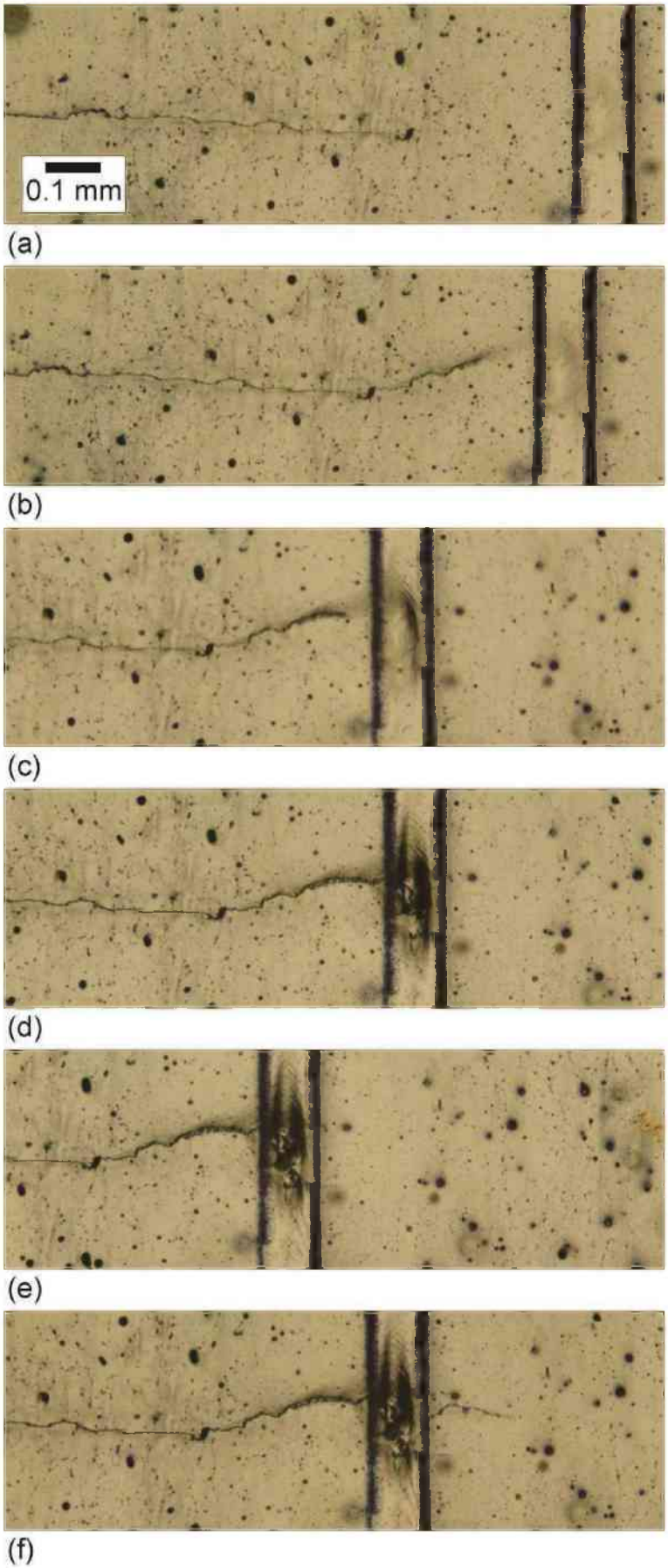

Fig. 6.22 Specimen 1–ΔK9: LM-micrograph of the fatigue crack in the vicinity of the interlayer on side 2. The labels correspond to the letters given in Fig. 6.19b.

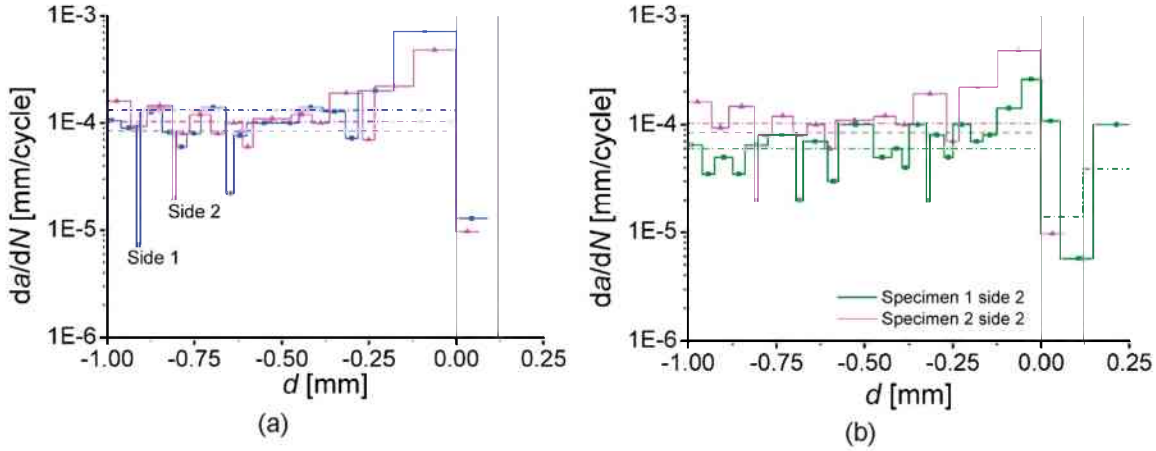

Fig. 6.23 Crack growth rate vs. distance to the hard/soft interface plots for Specimen 2-ΔK9 (a) and a comparison of the two specimens (b).

The d*a*/d*N*–*d*-plots of both sides of a second specimen tested with the same parameters, Specimen 2-ΔK9, are shown in Fig. 6.23a. The overall trend in Specimen 2-ΔK9 is similar to that of Specimen 1-ΔK9. A constant d*a*/d*N* is observed when the crack tip is far from the interlayer with an increase in d*a*/d*N* for the crack growing close to the hard/soft interface, with a subsequent drop in the growth rate inside the interlayer. The test of the specimen was stopped before crack growth from the soft to the hard layer occurred. Fig. 6.23b shows a comparison of the two specimens making the similar trends in the behavior obvious.

6.5.3 ΔK_{app} = 12 MPa√m

Specimen 1-ΔK12 is tested at ΔK_{app} = 12 MPa√m and R = 0.1. Fig. 6.24 shows a LM-micrograph of the specimen before testing. Fatigue crack growth through the first two hard and soft layers is analyzed here. The d*a*/d*N*–*d*-plots of the two specimen sides are shown in Fig. 6.25 and a series of photographs taken during the test on side 1 are shown in Fig. 6.26. The letters in Fig. 6.25a correspond to the labels of the images in Fig. 6.26.

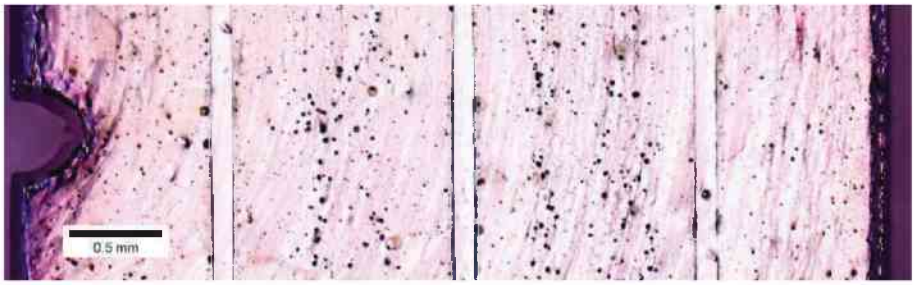

Fig. 6.24 The area in front of the notch of one specimen tested at ΔK = 12 MPa√m.

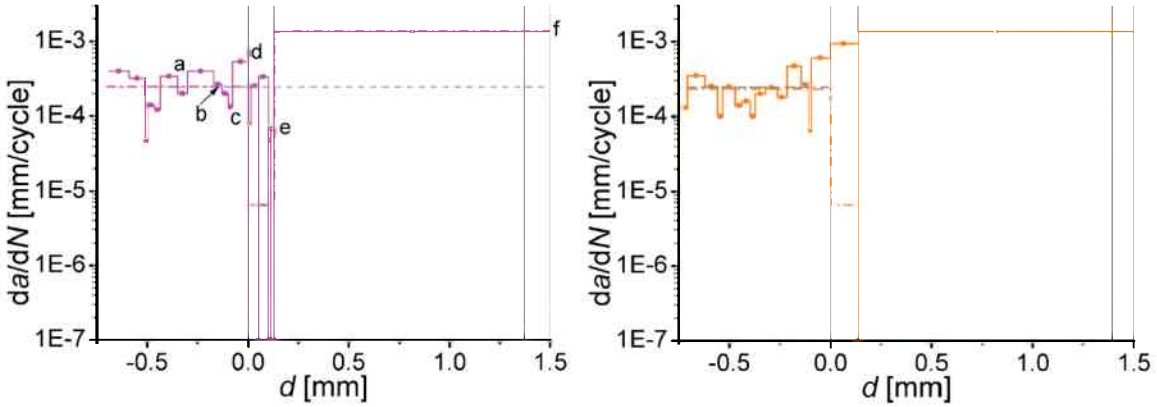

Fig. 6.25 Specimen 1-Δ*K*12: Crack growth rate vs. distance to the hard/soft interface plots for (a) side 1 and (b) side 2.

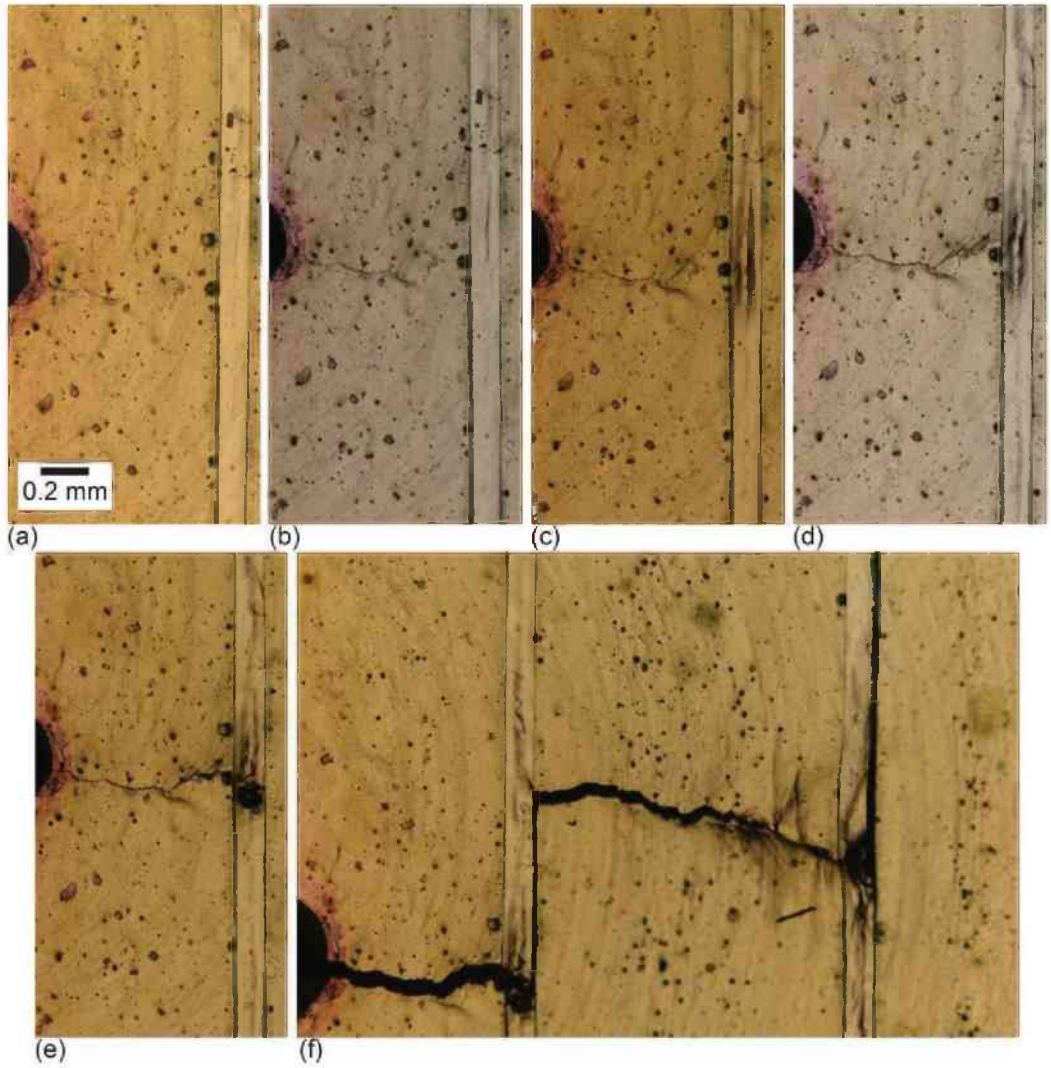

Fig. 6.26 Specimen 1-Δ*K*12: LM-micrographs of the fatigue crack in the vicinity of the interlayer on side 1. The labels correspond to the letters given in Fig. 6.25b.

On both sides of Specimen 1-$\Delta K12$ the fatigue crack grows with an average speed very similar to the one calculated using Eq. (6.5) up d = –0.11 mm, see Fig. 6.25a and Fig. 6.25b. Average da/dN values of 2.6 x 10^{-4} mm/cycle and 2.3 x 10^{-4} mm/cycle are measured on side 1 and side 2, respectively. For ΔK_{app} = 12 MPa$\sqrt{m}$ and R = 0.1 da/dN is 2.45 x 10^{-4} mm/cycle according to Eq. 6.5. Crack growth from the initial notch to the first interface happens within approx. 3000 cycles. An increase in da/dN is measured for crack growth towards the interlayer; directly before the interlayer da/dN reaches 5.1 x 10^{-4} mm/cycle on side 1 and 6.07 x 10^{-4} mm/cycle on side 2. A comparison of Fig. 6.26b and Fig. 6.26c shows that in this interval of crack growth plastic deformation starts inside the interlayer.

On side 1 the crack grows slowly through the interlayer and stops at the hard/soft interface, see Fig. 6.26e. On the second side the fatigue crack grows through the interlayer rapidly, but also stops at the second interface. The crack arrests at the soft/hard interface at both sides for approximately 2 x 10^4 cycles, without any crack growth or delamination occurring, resulting in an average da/dN of 6.45 x 10^{-6} mm/cycle inside the interlayer, which is 31 times lower than the average da/dN in Al7075-T6.

Thereafter, crack growth re-initiates remote from the main fatigue crack and the crack grows rapidly through the next hard and soft layer within 1000 cycles, which corresponds to an average da/dN of 1.37 x 10^{-3} mm/cycle, being nearly 6 times higher than the estimated value. Delamination at the second soft/hard interface is clearly visible in Fig. 6.26f, leading to crack arrest at the interface.

In this test da/dN_{tot} = 9.3 x 10^{-5} mm/cycle, which is a reduction in da/dN by a factor of 2.5 compared to the homogeneous material.

A second specimen, Specimen 2-$\Delta K12$, was tested at ΔK_{app} = 12 MPa$\sqrt{m}$ and R = 0.1, which is not discussed here. It should only be mentioned that the behavior of the specimen is very similar to the above described one, up to crack arrest in the first interlayer, where the test was stopped.

6.5.4 ΔK_{app} = 18 MPa√m

Testing of Specimen 1-ΔK5 shown in Fig. 6.13 with ΔK_{app} = 5 MPa√m has been stopped after fatigue crack propagation through the middle interlayer on both sides. Thereafter, ΔK_{app} is increased to 18 MPa√m for crack growth towards the third interlayer. The da/dN–d-data of both specimen sides are given in Fig. 6.27.

According to Eq. (6.5) a da/dN of 9.04 x 10^{-4} mm/cycle is expected for ΔK_{app} = 18 MPa√m, which is 30 % higher than the experimentally determined average da/dN. At d = –0.37 mm da/dN starts to increase strongly to da/dN = 7.1 x 10^{-3} mm/cycle, which is 11 times higher than the measured average values before. At d = –0.27 mm the test is aborted as significant delamination is observed at the hard /soft interface in front of the crack tip where the plastic zone touches the interface, see Fig. 6.28.

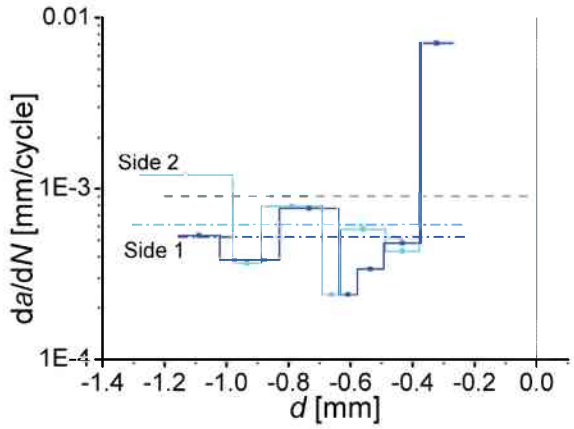

Fig. 6.27 Crack growth rate vs. distance to the hard/soft interface plots for the specimen tested at ΔK = 18 MPa√m.

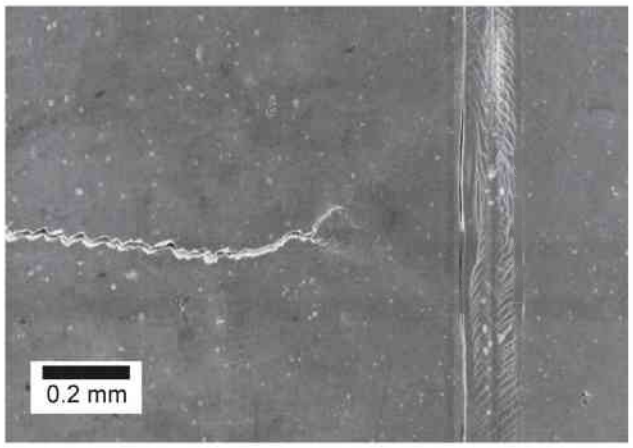

Fig. 6.28 SEM image of the specimen tested at ΔK = 18 MPa√m after stopping the test.

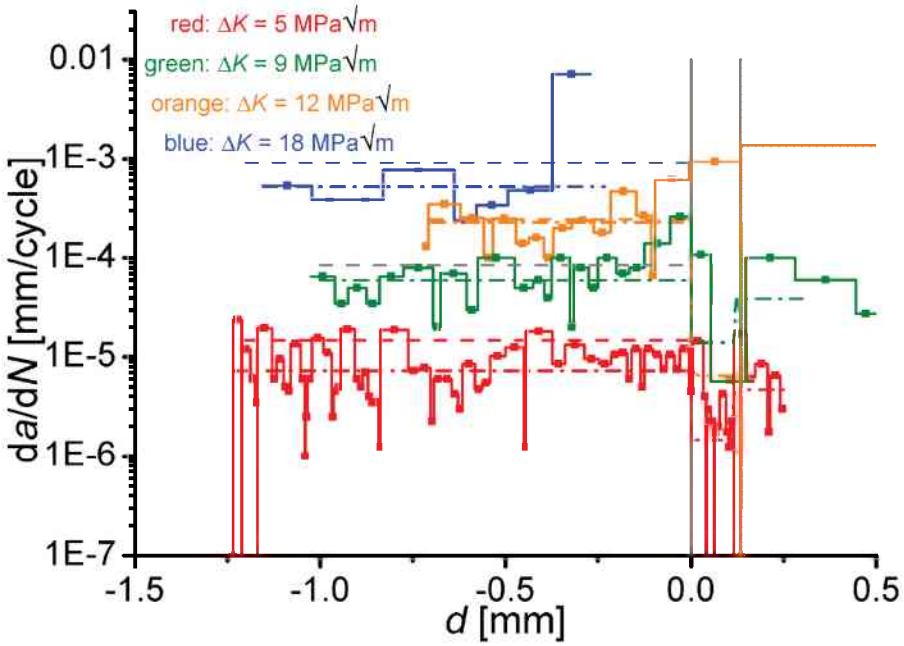

Fig. 6.29 Comparison of the fatigue test results for the different tested stress intensity ranges.

6.5.5 The material inhomogeneity effect in fatigue of multilayers with a yield strength inhomogeneity

The images of the specimen taken during or after testing at ΔK_{app} = 5 MPa√m, 9 MPa√m and 12 MPa√m, shown in Fig. 6.15, Fig. 6.21 and Fig. 6.26, exhibit that fatigue crack growth through the soft interlayers occurs with little to no delamination at the interfaces. This allows the conclusion that not the "classical" toughening mechanisms of crack deflection and bifurcation, which depend on delamination, are primarily responsible for the multilayer behavior discussed below.

In Fig. 6.29 representative d*a*/d*N*–*d*-plots of the specimens tested at the different stress intensity factor ranges are displayed. The dashed lines give the d*a*/d*N* values calculated for homogeneous Al7075-T6 according to Eq. (6.5) and the dash-dot lines show the average d*a*/d*N* values determined from the experiments.

Far from the interlayer, d*a*/d*N* for all ΔK_{app} values remains relatively constant. For ΔK_{app} = 5 MPa√m, 9 MPa√m and 18 MPa√m the average d*a*/d*N* far from the interlayer is lower than the one calculated according to the Paris' law determined by Marissen. A possible reason for this discrepancy could be that the fatigue crack growth direction with respect to the orientation of the sheets varies. In the current study, the fatigue crack propagate in thickness direction of the sheets, whereas in the tests conducted in [77] the fatigue crack

Table 6.1 Comparison of the plastic zone radii and the distance to the interface where a first increase in da/dN is observed.

	r_y	d_i
ΔK_{app} = 9 MPa√m.	0.06 mm	0.125 mm
ΔK_{app} = 12 MPa√m.	0.1 mm	0.11 mm
ΔK_{app} = 18 MPa√m.	0.24 mm	0.27 mm

propagates in the long transverse direction of the sheets. This orientation change can cause a strong alteration in the material response. This has also been observed in the fracture mechanics experiments and is discussed in Publication C, Section 5.3.2.

At the lowest ΔK_{app} no significant variation of da/dN is observed within the first hard layer. For all other ΔK_{app} values the initially constant da/dN increases in front of the hard/soft interface. The d-value where this increase occurs should be connected to the plastic zone size in front of the crack tip [24,25,63]. The radius of the monotonic plastic zone under plane stress conditions at $K_{app,max}$ can be estimated using the equation proposed by Irwin [79],

$$r_y = \frac{1}{2\pi}\frac{K_{app,max}^2}{R_{p0.2}}. \tag{6.7}$$

Inserting the $K_{app,max}$ and $R_{p0.2}$ = 520 MPa into Eq. (6.7) yields plastic zone radii of 0.06 mm for ΔK_{app} = 9 MPa√m, 0.01 mm for ΔK_{app} = 12 MPa√m and 0.24 mm for ΔK_{app} = 18 MPa√m. In Table 6.1 r_y is compared to the d values where the first increase in da/dN is observed, denominated d_i here. For all ΔK_{app} values the calculated r_y is smaller than d_i. A possible explanation for this difference is that the local stress intensity range ΔK_{tip} is higher than ΔK_{app} and therefore the actual plastic zone size is larger than estimated according to Eq. (6.7). This case of $\Delta K_{tip} > \Delta K_{app}$ corresponds to an anti-shielding case, which could occur here due to the decrease in material strength in crack propagation direction. It has to be remarked, that the actual plastic zone shape is more complicated than the assumption of a circular shape by Irwin and is also affected by the presence of the interlayer. Therefore, it is complicated to quantify the influence the anti-shielding effect has on the plastic zone size, without the knowledge about the real shape of the plastic zone.

In Fig. 6.28 it is also clearly visible that the plastic zone, after stopping the test at ΔK_{app} = 18 MPa√m test at d = –0.27 mm, is interacting with the interface. This is assumed to be caused by the anti-shielding effect originating in the material inhomogeneity. Due to the delamination caused by the high strains at the interface, the crack is expected to stop at the interlayer, in accordance with the mechanisms of crack arrest described in Section 1.2.1.

Whenever the fatigue crack propagates into a soft interlayer, the average da/dN decreases significantly before crack growth through the soft/hard interface occurs. In absence of delamination this can again be explained by the material inhomogeneity effect causing a shielding effect, which hinders crack propagation through the soft interlayer and into the next hard layer.

An effect worth noticing is the formation of cracks perpendicular to the main fatigue crack in the middle of the interlayer, e.g. side 2 of the specimen tested at ΔK_{app} = 5 MPa√m, see Fig. 6.15b. Such cracks not only form at ΔK_{app} = 5 MPa√m but also at higher ΔK_{app}. It is assumed that these cracks form due to the high plastic strains in loading direction and the constrained lateral contraction inside the soft interlayer. For high strains and in the absence of delamination at the interfaces between hard and soft layers, the hard material hinders the lateral contraction perpendicular to the interface and the loading direction in the soft layer. This induces tensile stresses perpendicular to loading direction, which may lead to the formation of the crack inside the soft interlayer.

In all cases where crack growth in the interlayer occurs, it is possible for the fatigue crack to grow through the soft/hard interface. For ΔK_{app} = 5 MPa√m and ΔK_{app} = 9 MPa√m the main fatigue crack grows through the interlayer (Fig. 6.15 and Fig. 6.21). In the specimen tested at ΔK_{app} = 12 MPa√m, a different behavior is observed, where the fatigue crack stops at the hard/soft interlayer and crack growth is re-initiated at another location along the interface, see Fig. 6.26f. The difference that at low ΔK_{app} the crack is not fully arrested and can grow through the interface without re-initiation, may be responsible for the weak decrease in the average da/dN values in the interlayer discussed above.

After crack growth through the soft/hard interface, it is found for the tests conducted with ΔK_{app} = 5 MPa√m and ΔK_{app} = 9 MPa√m that da/dN in the second hard layer reaches values comparable to those of the first interlayer. In case of the specimen tested at ΔK_{app} = 12 MPa√m, da/dN increases strongly after re-initiation of crack growth in the second hard layer. The high da/dN in the second hard layer can be explained by an increase in ΔK_{app}, which originates due to the fact that the applied load was not decreased during crack extension. Due to the constant load, the increasing crack length causes ΔK_{app} to increase, e.g. at d = 1.5 mm (soft/hard interface of the second interlayer) $\Delta K_{app} \approx$ 36 MPa√m and $K_{max} \approx$ 40 MPa√m, which is 1.6 times higher than K_{JC} of Al7075-T6, compare Section 0. That a K_{max} higher than the fracture toughness does not lead to fracture of the specimen can be attributed to the delamination at the soft/hard interface of the second interlayer, which leads to a complete crack arrest and once again shows the excellent fracture behavior of the multilayers in crack arrester configuration.

Finally the overall influence of the interlayers on the fatigue behavior of the multilayers should be discussed. For all ΔK_{app} values, except ΔK_{app} = 18 MPa√m, da/dN_{tot} is calculated, which can be used as a measure of the influence

the interlayer has on the fatigue behavior. In Table 6.2 the average da/dN values measured in the first hard layers are compared to da/dN_{tot}. In all investigated cases da/dN_{tot} is smaller, which corresponds to an improvement in fatigue lifetime. The crack growth rate is decreased by 20 % for ΔK_{app} = 5 MPa√m, by 60 % for ΔK_{app} = 9 MPa√m and by 260 % for ΔK_{app} = 12 MPa√m.

It can be concluded that the introduction of the 10 % Al1050 into the structures improves the fatigue behavior due to the material inhomogeneity effect, and that the magnitude of the effect depends strongly on the applied ΔK. A complete arrest of the fatigue crack is only expected for ΔK_{app} = 18 MPa√m, as there delamination occurs in front of the crack tip.

Table 6.2 Comparison of the average da/dN in Al7075-T6 and da/dN_{tot}.

	da/dN (Al7075-T6) [mm/cycle]	da/dN_{tot} [mm/cycle]
ΔK_{app} = 5 MPa√m.	$7{,}5 \times 10^{-6}$	5.95×10^{-6}
ΔK_{app} = 9 MPa√m.	8×10^{-5}	3.45×10^{-6}
ΔK_{app} = 12 MPa√m.	2.45×10^{-4}	9.3×10^{-5}

6.5.6 Comparison of the experiments with fatigue crack growth modeling

In Appendix I the procedure to model fatigue crack growth in multilayer structures is outlined, which follows the work by Kolednik et al. [30]. The results of the simulations and the experiments should be compared shortly in this chapter. In Fig. 6.30 the experimentally determined da/dN–d-plots of all ΔK_{app} values are shown together with the modeling results. In all graphs, the results from modeling in plane strain conditions are given as black lines. Additionally, the curve modeled for ΔK_{app} = 9 MPa√m and plane stress conditions is shown in orange in Fig. 6.30b.

In Fig. 6.30a,b,d the calculated crack growth rates for crack growth far from the interlayer are higher than the average experimental values. This results from the way da/dN is calculated based on the Paris' law determined by Marissen [77]. As discussed in Section 6.5.5, this da/dN vs. ΔK_{eff} curve might overestimate the crack growth rate due to differences in the investigated orientation.

For ΔK_{app} = 5 MPa√m, see Fig. 6.30a, modeling shows that the anti-shielding effect caused by the yield strength inhomogeneity causes da/dN to increase steeply only for -0.03 mm < d < 0 mm, which might not be detectable in the test. This could explain why no anti-shielding effect was observed experimentally in front of the hard/soft interface.

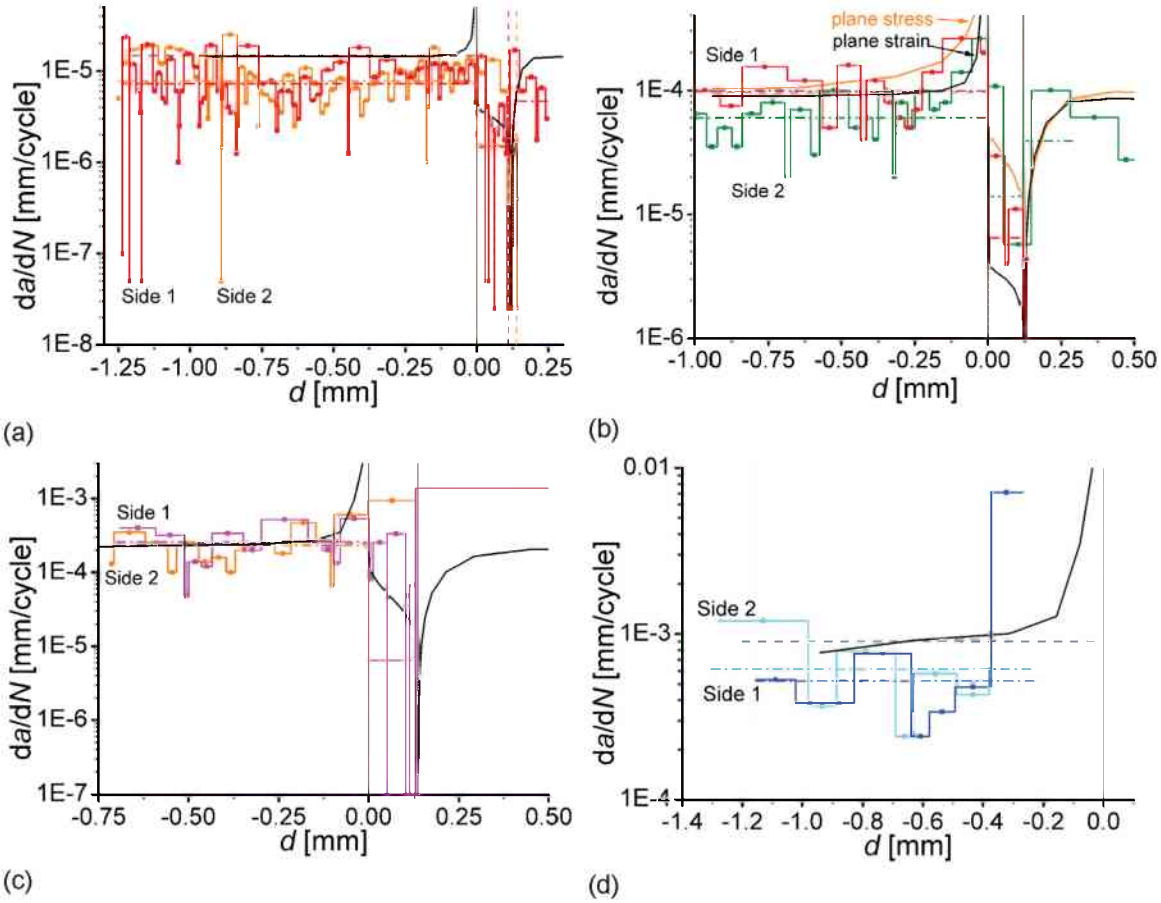

Fig. 6.30 Crack growth rate vs. distance to the hard/soft interlayer plots for (a) ΔK = 5 MPa√m, (b) ΔK = 9 MPa√m, (c) ΔK = 12 MPa√m and (d) ΔK = 18 MPa√m. The black curves show the results of the simulations.

For ΔK_{app} = 9 MPa√m simulations are done for plane stress and plane strain conditions, see Fig. 6.30b. This was tried to see which influence a difference in the stress state has on the material inhomogeneity effect. In the specimen, which has a thickness B = 1 mm approximately 88 % of the thickness are dominated by plane strain conditions and only 6 % close to each surface are dominated by a plane stress state. This estimation is based on the plastic zone radius given in Table 6.1 and the assumption that at each specimen side plane stress conditions are dominant to a depth of the plastic zone radius. Due to this mixture of the stress states, the experimental data are expected to lie between the modeled curves. The larger plastic zone under plane stress conditions causes the anti-shielding effect to start at smaller d values than under prevailing plane strain. Fig. 6.30b shows that except for the overestimation of da/dN far from the interlayer, the anti-shielding effect at the first interface, as well as the shielding effect inside the interlayer are reflected well in the calculations.

For ΔK_{app} = 12 MPa√m, Fig. 6.30c, the crack growth rate and its increase in da/dN originating in the anti-shielding effect are predicted well in the simulations. The agreement of the experimental and modeled curves in the second hard layer is poor, which is simply caused by the fact that the

experimentally applied ΔK value was not held constant during this interval of crack growth and was distinctly higher than the modeled ΔK_{app} = 12 MPa√m.

For ΔK_{app} = 18 MPa√m, see Fig. 6.30d, only few data points are available to allow a comparison. The strong increase in the experimental d*a*/d*N* values in front of the interface, which is attributed to the anti-shielding effect, occurs at significantly smaller *d* values than predicted by modeling. A possible explanation for this difference can be an influence of the developing delamination of the hard/soft interface in front of the crack tip on the crack driving force. The delamination in front of the crack tip influences the in-plane constraint, as the area where delamination occurs is an additional free surface. This can strongly alter the crack driving force and cannot be accounted for in modeling, as only perfect interfaces are modeled.

Concludingly, it can be remarked that the agreement between the modeling and experimental results is good as long as no delamination occurs. It should also be noted that in the simulations only the mechanical properties of the materials and the geometry of the specimen are introduced and no fit parameters are used.

6.6 Comparison of the multilayers with elastic and yield strength inhomogeneities

In this section the results of the tests conducted at ΔK_{app} = 9 MPa√m on the multilayers with elastic (Section 0) and yield strength (Section 0) inhomogeneity should be compared. The d*a*/d*N*–*d*-curves of the two Al7075/Adhesive specimens with Young's modulus inhomogeneity and Al7075/Al1050 Specimen 1-ΔK9 with the yield strength inhomogeneity are plotted in Fig. 6.31.

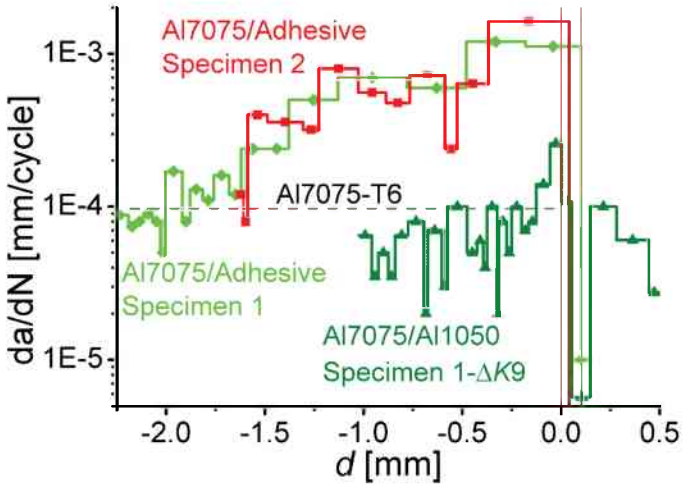

Fig. 6.31 Comparison of the fatigue test results of the multilayers with elastic and yield strength inhomogeneities.

The anti-shielding effect is more pronounced in the Al7075/Adhesive system as is clearly seen in Fig. 6.31: The increase in da/dN starts at a larger distance to the interface and leads to higher maximum crack growth rates. Fig. 6.32a shows the modeled variation of $\Delta K_{tip,eff}$ for –1 mm < d < 0.25 mm for ΔK_{app} = 9 MPa√m, R = 0.1, and plane strain conditions for the elastic and yield strength inhomogeneities. The dashed red line gives $\Delta K_{tip,eff}$ for the applied ΔK in a homogeneous material. The experimental observation that the elastic inhomogeneity causes a stronger anti-shielding effect is supported by the modeling results. For the elastic inhomogeneity $\Delta K_{tip,eff}$ starts to increase at smaller d and reaches higher values than for the yield strength inhomogeneity, which is in good accordance with the experimental results.

In the elastically inhomogeneous multilayers, no fatigue crack growth through the interlayer is observed. Instead, fracture of the compliant interlayer is visible remote from the initial fatigue crack. In the Al7075/Adhesive multilayer the crack grows into the soft interlayer at a high da/dN but the growth rate generally decreases for growth through the soft interlayer due to the shielding effect.

Neither Fig. 6.6 for the elastically inhomogeneous structure, nor Fig. 6.21 for the composite with the yield strength inhomogeneity show delamination at the second interface after the crack tip has reached it. But while the fatigue crack can propagate through the soft/hard interface into the next hard layer of the metal laminate it arrests at the second interface in the Al7075/Adhesive specimens.

Fig. 6.32b, being a magnification of the interlayer area of Fig. 6.32a, shows the variation of $\Delta K_{tip,eff}$ inside the interlayer for the two multilayer systems. For the multilayer with the yield strength inhomogeneity, $\Delta K_{tip,eff}$ decreases from 5.9 MPa√m near the hard/soft interface to 3.2 MPa√m close to the soft/hard interface inside the interlayer. Inside the compliant interlayer, $\Delta K_{tip,eff}$ is 0.45 MPa√m near the stiff/compliant interface and decreases to 0.2 MPa√m close to the compliant/stiff interface. The modeling results clearly show that the Young's modulus inhomogeneity leads to a more pronounced shielding effect in the interlayer than the yield strength inhomogeneity, which can explain why the crack arrests in the compliant - but not in the soft interlayer.

This difference that the crack can grow through the soft/hard interface, while it arrests at the compliant/stiff interface and has to re-initiate in the stiff phase has a big influence on the fatigue behavior of the structures. As discussed before, the initiation of a fatigue crack is very energy consuming and leads to a significant increase in fatigue lifetime. Consequently the improvement

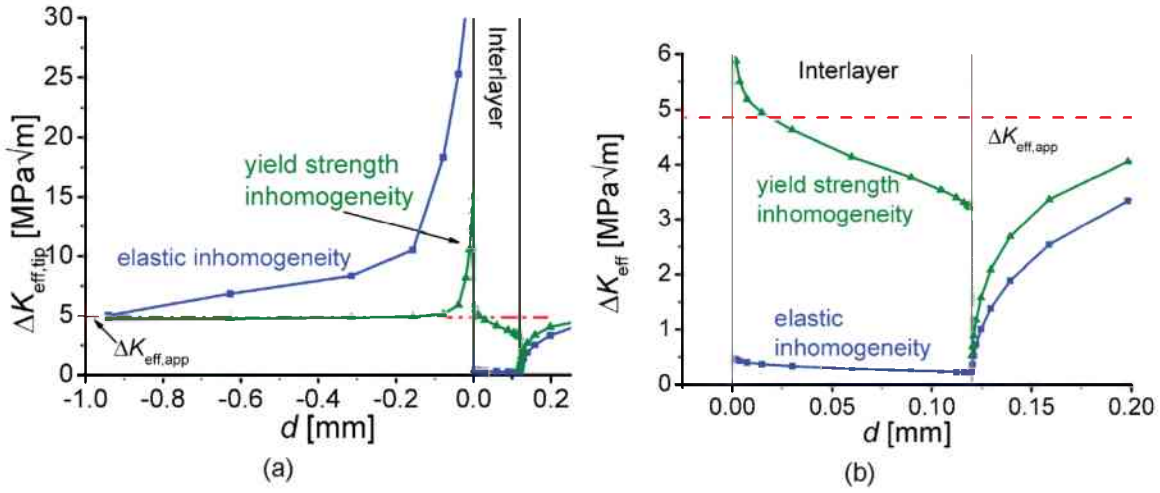

Fig. 6.32 The modeled curves show the variation of the effective stress intensity range in the interlayer for plane strain conditions.

of the fatigue lifetime is not as pronounced in the multilayers with yield strength inhomogeneity as in the elastically inhomogeneous ones. At the applied ΔK the fatigue lifetime of the Al7075/Al1050 structure is increased by a factor 2.5, while it increases by factors of 46 and 11 for the Al7075/Adhesive Specimens 1 and 2, respectively.

Summarizing it can be stated that the introduction of either soft or compliant interlayers has a beneficial effect on the fatigue behavior of Al7075-T6, but the effect is much more pronounced for the compliant than for the soft interlayers. This behavior is caused by a difference in the effectiveness of the shielding effect of the Young's modulus and yield strength inhomogeneities.

The experimental and modeling results of the fatigue tests at ΔK_{app} = 9 MPa√m for the multilayers with elastic or yield strength inhomogeneities and the conclusions drawn in this chapter are currently prepared for publication.

7

SUMMARY

Aim of the present work was to experimentally investigate the influence of the material inhomogeneity effect on the fracture and fatigue behavior of layered composite structures and to gain a better understanding of the mechanisms leading to damage resistant behavior in such multilayers.

Two phase multilayers were constructed and investigated representing two different types of inhomogeneities: The first one has a difference in the elastic material properties and is denominated Young's modulus inhomogeneity while in the second both phases have the same elastic but different plastic properties, which is therefore denoted yield strength inhomogeneity. Two multilayers with Young's modulus inhomogeneities were tested, the first consisting of a commercial printing paper, acting as stiff phase, separated by air and the second based on Al7075-T6, a high strength aluminum alloy serving as stiff phase, which was connected by a thermoplastic adhesive. The same high strength aluminum alloy was chosen as base material for a multilayer with a yield strength inhomogeneity, which was connected by roll-bonding with layers of soft technically pure aluminum.

To be able to characterize the multilayers, the base materials had to be investigated with respect to their fracture toughness. This led to the development of two new methods allowing the determination of crack growth resistance curves of short fiber composites, e.g. the used printing paper, using cohesive zone modeling and local deformation analysis.

Fracture toughness experiments on the multilayers with the Young's modulus inhomogeneity in crack arrester configuration showed that both tested systems exhibit strongly improved fracture resistance compared to the base materials. Equations allowing the estimation of the maximum fracture resistance and the optimum multilayer structure from the mechanical properties of the constituents and the specimen geometries are derived and applied successfully. A similar behavior was also found for fracture of the system with the yield strength inhomogeneity. One important result was that crack arrest in the interlayers can occur without the onset of delamination distinguishing the material inhomogeneity effect from the classical crack arrest mechanisms of crack blunting and bifurcation. Nevertheless, it was found that the amount of occurring delamination after crack arrest in the interlayer strongly influences the maximum achievable fracture resistance.

Fatigue testing was conducted on the aluminum based multilayer with the Young's modulus inhomogeneity and the system exhibiting the yield strength inhomogeneity. The introduction of the interlayers leads to a significant improvement of the fatigue behavior for both investigated systems. However, the much more pronounced improvement was observed for the Young's modulus inhomogeneity than for the yield strength inhomogeneity. Modeling of the fatigue experiments using the concept of configurational forces revealed that the Young's modulus inhomogeneity leads to a stronger decrease of the crack driving force in the interlayer than the yield strength inhomogeneity. This necessitated a re-initiation of crack growth in the Al7075-T6, which is generally very energy consuming. In the multilayers with yield strength inhomogeneity the crack was able grow through the interface, as the decrease in crack driving force was not as pronounced as in the elastically inhomogeneous case. As the crack did not need to re-initiate, the improvement in the system with the yield strength inhomogeneity was not as strong as in the system with the Young's modulus inhomogeneity.

To sum up the results it can be stated that the fracture and fatigue behavior of multilayer structures with a Young's modulus or yield strength inhomogeneity is generally better than that of the homogeneous constituents, making these structures attractive candidates for the design of damage resistant materials. Furthermore, it was seen that the material inhomogeneity effect increases strongly with increasing variation of the mechanical properties of the constituents of the multilayers.

APPENDIX I: FATIGUE CRACK GROWTH MODELING

A short general overview on the numerical evaluation of the material inhomogeneity term using the configurational forces concept (see Chapter 3) and the crack driving forces in an inhomogeneous material using finite element modeling is given in Section I.1. In Section I.2 the application of the numerical results to describe fatigue crack growth is outlined, which is then applied in Section I.3 to model the fatigue experiments from Chapter 6.

I.1 Evaluation of the material inhomogeneity term

To evaluate the configurational forces numerically a post-processing program was developed for the finite element program ABAQUS [80]. The post processing procedure is based on the works of Mueller [81,82] and Denzer [83] and is described in detail in the work by Schöngrundner [84].

The analysis can be carried out for both small strain and large strain formulations and plane strain or plane stress conditions. In general two-dimensional models containing a stationary crack are used. To account for crack growth either crack length, distance to the interface, or both, are varied. The materials on both sides of the interface are modeled as isotropic and the interface bonding is assumed to be perfect. Thus, no crack deflection or delamination can be modeled. Elastic or elastic-plastic material behavior can be modeled, the latter using the incremental plasticity model provided in ABAQUS.

The far-field J-integral J_{far} is evaluated using the virtual crack extension method implemented in ABAQUS. A rectangular contour Γ_{far} close to the outer boundary of the body is used to calculate J_{far}. There are two possibilities to calculate J_{tip}: The first is using the virtual crack extension method along a boundary Γ_r around the crack tip, see Fig. 3.1. The resulting J_{tip} should be path independent as long as Γ_r does not touch the interface. Due to numerical reasons this is not always the case [84]. The second possibility is to evaluate J_{tip} as the sum of C_{inh} and J_{far}, see Eq. (3.9),

$$J_{tip} = J_{far} + C_{inh} \,. \tag{I.1}$$

Especially for a crack tip close to the interface, the latter method yields more accurate results and is therefore applied in the current work.

If the assumptions made in Section 3.2 are valid, Eq. (3.8) can be rewritten in component form for small strain theory as:

$$C_{inh} = -\int_{\Sigma} \left([\![\Phi]\!] - \langle \sigma_{ik} \rangle [\![\varepsilon_{ik}]\!] \right) n_j e_j \, \mathrm{d}l \,, \tag{I.2}$$

The evaluation of the configurational forces by the post-processing procedure is done using the equilibrium stress and strain fields determined in the finite element stress analysis. The parameter ϕ is taken as the total strain energy density, which means that deformation theory of plasticity is assumed in post-processing. The integration along the interface is conducted using the trapezoid formula. Hereby the integration point values of the stress and strain components of the elements are extrapolated to the element nodes on both sides of the interface.

Thus J_{tip} can be calculated by inserting J_{far}, determined using the virtual crack extension method, and C_{inh}, calculated according to Eq. (I.2).

I.2 Modeling of fatigue crack growth using the configurational forces model

Aim of fatigue crack growth modeling is the determination of the effective stress intensity range ΔK_{eff}, which allows the evaluation of the fatigue crack growth rate da/dN for the experimentally studied multilayers. Therefore, J_{tip} is converted into a near-tip stress intensity factor K_{tip} using the relation,

$$K_{tip} = \sqrt{E' J_{tip}} , \tag{I.3}$$

where $E' = E$ for plane stress and $E' = E/(1-\nu^2)$ for plane strain conditions. Using Eq. (I.3) $K_{tip,max}$ and $K_{tip,min}$ are calculated at the maximum and minimum applied loads, which allows to calculate the near-tip stress intensity range,

$$\Delta K_{tip,app} = K_{tip,max} - K_{tip,min} . \tag{I.4}$$

To exclude the effect of plasticity induced crack closure, the effective near-tip stress intensity range $\Delta K_{tip,eff}$ is calculated from $\Delta K_{tip,app}$ by applying Elber's relation [75,76], see also Chapter 6,

$$\Delta K_{tip,eff} = (0.5 + 0.4 R_{tip}) \Delta K_{tip,app} , \tag{I.5}$$

where the near-tip stress ratio is given by,

$$R_{tip} = \frac{K_{tip,min}}{K_{tip,max}} . \tag{I.6}$$

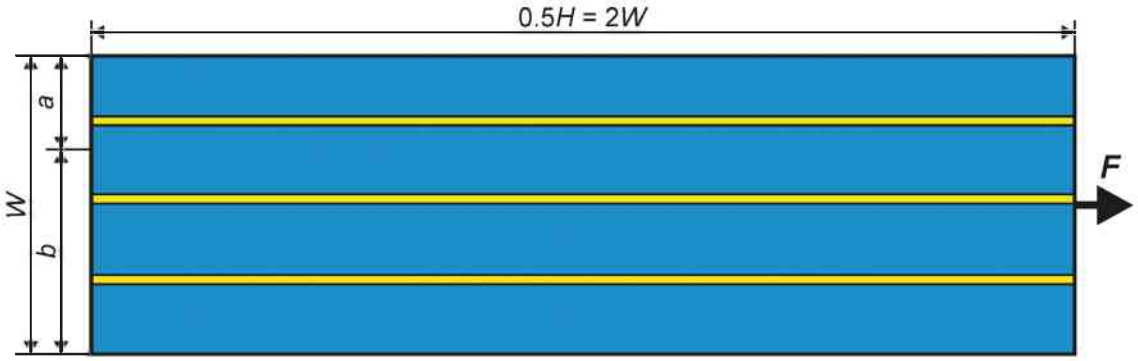

Fig. I.1 Draft of the numerical model of the multilayer SE(T) specimen. The hard/stiff phase is shown in blue, the soft/compliant phase in yellow.

I.3 Numerical d*a*/d*N*-evaluation for multilayer structures

A 2D SE(T) specimen, with the same geometry as described in Chapter 4.3.2 and shown Fig. 4.13, was modeled by Jozef Predan at the University of Maribor. Both the stiff/compliant and hard/soft multilayer structures are investigated numerically. Constant applied stress intensity ranges ΔK_{app} = 5 MPa√m, 9 MPa√m, 12 MPa√m and 18 MPa√m with R_{app} = 0.1are modeled in plane strain conditions. Additionally, ΔK_{app} = 9 MPa√m is modeled using plane stress conditions for the hard/soft multilayers. Simulations are carried out using a commercial implementation of the finite element method (ABAQUS). Due to symmetry only one half of the multilayered specimen, shown in Fig. I.1, is modeled using 568400 elements. Two-dimensional first order 4-node elements are used. The smallest mesh edge size is 0.051 µm at the crack tip and along the interfaces. The smallest distance of the crack tip to the interfaces is 3.1 µm.

For strains lower than the yield strain the multilayer constituents are modeled as linear elastic and as elastic-plastic for higher strains using the hardening behavior determined in the tensile tests. Cyclic hardening or softening of the constituents is neglected.

Modeling is conducted using a stationary crack of length *a*. The crack length and consequently the distance *d* of the crack tip from the second hard/soft or stiff/compliant interface are varied. Modeling is conducted for -1 mm ≤ *d* ≤ 1 mm. The final modeling result shows the variation of $\Delta K_{tip,eff}$ in dependence of *d*. To allow a comparison with the experimentally determined d*a*/d*N*–*d*-plots, d*a*/d*N* is calculated from $\Delta K_{tip,eff}$. Therefore, $\Delta K_{tip,eff}$ is inserted into the Paris's laws of the constituents. The Paris' law of Al7075-T6, determined by Marissen [77], was already given in Eq. (6.5) and is repeated here,

$$\frac{da}{dN} = 6.04 \times 10^{-7} \Delta K_{eff}^{3.215} \quad \text{(I.7)}$$

For Al1050 the Paris' law is given by,

$$\frac{da}{dN} = 1.65 \times 10^{-7} \Delta K_{eff}^{3.264} \quad \text{(I.8)}$$

Eq. (I.8) is calculated from fatigue data of Al1050 given for various *R*-ratios in the book by Taylor [85]. The Paris' laws of Al7075-T6 and Al1050 are plotted in Fig. I.2. No fatigue data could be obtained experimentally or from literature for SS315, the adhesive used in the stiff/compliant multilayer, therefore only $\Delta K_{tip,eff}$–*d*-plots are given for the stiff/compliant multilayers.

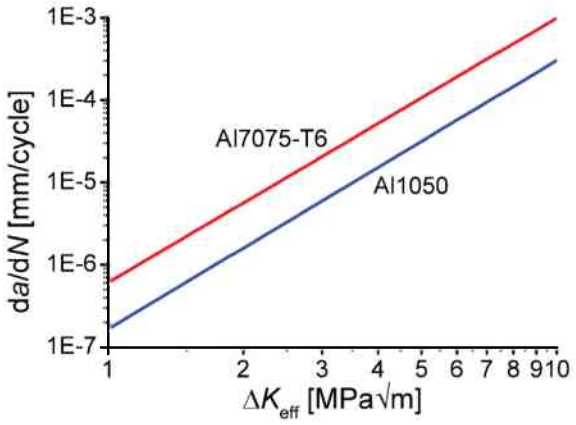

Fig. I.2 Paris' laws of Al7075-T6 and Al1050 [77,85].

REFERENCES

[1] Anderson TL. Fracture Mechanics: Fundamentals and Applications, 3rd ed. Boca Raton: Taylor & Francis; 2005.

[2] Embury JD, Petch NJ, Wraith AE, Wright ES. The fracture of mild steel laminates. Trans Metall Soc AIME 1967;239:114.

[3] Lesuer DR, Syn CK, Sherby OD, Wadsworth J, Lewandowski JJ, Hunt WH. Mechanical behaviour of laminated metal composites. Int Mater Rev 1996;41:169.

[4] Wadsworth J, Lesuer DR. Ancient and modern laminated composites - from the Great Pyramid of Gizeh to Y2K. Mater Charact 2000;45:289.

[5] Embury D, Bouaziz O. Steel-Based Composites: Driving Forces and Classifications. Ann Rev Mater Res 2010;40:213.

[6] Cepeda-Jiménez CM, García-Infanta JM, Pozuelo M, Ruano OA., Carreño F. Impact toughness improvement of high-strength aluminium alloy by intrinsic and extrinsic fracture mechanisms via hot roll bonding. Scripta Mater 2009;61:407.

[7] Cepeda-Jiménez CM, Pozuelo M, García-Infanta JM, Ruano OA, Carreño F. Interface Effects on the Fracture Mechanism of a High-Toughness Aluminum-Composite Laminate. Metall Mater Trans A 2008;40:69.

[8] Alic JA, Danesh A. Fracture of laminates combining 2024-T3 and 7075-T6 aluminum alloys. Engng Fract Mech 1978;10:177.

[9] Kaufman JG. Fracture toughness of 7075-T6 and -T761 sheet, plate, and multi-layered adhesive bonded panels. J Basic Engng Trans ASME 1967;89:503.

[10] Marouf BT, Bagheri R, Mahmudi R. Role of interfacial fracture energy and laminate architecture on impact performance of aluminum laminates. Composites Part A 2008;39:1685.

[11] Alderliesten RC, Schijve J, Zwaag SVD. Application of the energy release rate approach for delamination growth in Glare. Engng Fract Mech 2006;73:697.

[12] Sadighi M, Alderliesten RC, Benedictus R. Impact resistance of fiber-metal laminates: A review. Int J Impact Eng 2012;49:77.

[13] Castrodeza EM, Perez Ipiña JE, Bastian FL. Fracture toughness evaluation of unidirectional fibre metal laminates using traditional CTOD (δ) and Schwalbe (δ5) methodologies. Engng Fract Mech 2004;71:1107.

[14] Castrodeza EM, Bastian FL, Perez Ipiña JE. Fracture toughness of unidirectional fiber–metal laminates: crack orientation effect. Engng Fract Mech 2005;72:2268.

[15] Herzberg RW. Deformation and fracture mechanics of engineering materials. New York: Wiley; 1976.

[16] Kolednik O, Predan J, Fischer FD, Fratzl P. Bioinspired design criteria for damage-resistant materials with periodically varying microstructure. Adv Funct Mater 2011;21:3634.
[17] Hassan HA, Lewandowski JJ, Abd El-Latif MH. Effects of lamination and changes in layer thickness on fatigue-crack propagation of lightweight laminated metal composites. Metall Mater Trans A 2004;35:45.
[18] Hassan HA, Lewandowski JJ. Effects of high temperature and thermal exposure on fatigue crack propagation of laminated metal composites. Mater Sci Technol 2007;23:1505.
[19] Alderliesten R, Homan J. Fatigue and damage tolerance issues of Glare in aircraft structures. Int J Fatigue 2006;28:1116.
[20] Khan SU, Alderliesten RC, Benedictus R. Delamination in Fiber Metal Laminates (GLARE) during fatigue crack growth under variable amplitude loading. Int J Fatigue 2011;33:1292.
[21] Osman TM, Hassan HA., Lewandowski JJ. Interface Effects on the Quasi-Static and Impact Toughness of Discontinuously Reinforced Aluminum Laminates. Metall Mater Trans A 2008;39:1993.
[22] Rakin M, Kolednik O, Medjo B, Simha NK, Fischer FD. A case study on the effect of thermal residual stresses on the crack-driving force in linear-elastic bimaterials. Int J Mech Sci 2009;51:531.
[23] Simha NK, Kolednik O, Fischer FD. Material force models for cracks – Influences of eigenstrains, thermal strains and residual stresses. In: Proc. ICF 11, 2005.
[24] Suresh S, Sugimura Y, Tschegg E. The growth of a fatigue crack approaching a perpendicularly-oriented, bimaterial interface. Scripta Metall Mater 27;1992:1189.
[25] Pippan R, Flechsig K, Riemelmoser FO. Fatigue crack propagation behavior in the vicinity of an interface between materials with different yield stresses. Mater Sci Eng A 2000;283:225.
[26] Jiang F, Deng ZL, Zhao K, Sun J. Fatigue crack propagation normal to a plasticity mismatched bimaterial interface. Mater Sci Eng A 2003;356:258.
[27] Bhat S, Narayanan S. A computational model and experimental validation of shielding and amplifying effects at a crack tip near perpendicular strength-mismatched interfaces. Acta Mech 2010;216:259.
[28] Sugimura Y, Lim PG, Shih CF, Suresh S. Fracture normal to a bimaterial interface: Effects of plasticity on crack-tip shielding and amplification. Acta Metall Mater 1995;43:1157.
[29] Pippan R, Riemelmoser F. Fatigue of bimaterials. Investigation of the plastic mismatch in case of cracks perpendicular to the interface. Comp Mater Sci 1998;13:108.

[30] Kolednik O, Predan J, Gubeljak N, Fischer DF. Modeling fatigue crack growth in a bimaterial specimen with the configurational forces concept Mater Sci Eng A 2009;519:172.

[31] Broek D. Elementary engineering fracture mechanics, Kluwer Academic Publishers Group, 1982.

[32] Wells AA. Unstable crack propagation in metals-cleavage and fast fracture. Proc Crack Propagation Symposium,1961:210.

[33] Wells AA. Application of fracture mechanics at and beyond general yielding. Br Welding J 1963;10:563.

[34] Rice JR. A Path Independent Integral and the Approximate Analysis of Strain Concentration by Notches and Cracks. J Appl Mech 1968;35:379.

[35] Kolednik O, Stüwe HP. The stereophotogrammetric determination of the critical crack tip opening displacement. Engng Fract Mech 1985;21:145.

[36] Kolednik O. Fracture mechanics. In: Nicolais L, Borzacchiello A, editors. Encyclopedia of Composites, Second Edition. Hoboken: John Wiley & Sons; 2012.

[37] Hutchinson JW. Plastic stress and strain fields at a crack tip. J Mech Phys Solids 1968;16:337.

[38] Rice JR, Rosengren GF. Plane strain deformation near a crack tip in a power-law hardening material. J Mech Phys Solids 1968;16:1.

[39] Standard test method for measurement of fracture toughness. E-1820-08. Annual Book of ASTM Standards, Vol. 03.01: ASTM; 2008.

[40] Metallic materials – Unified method of test for the determination of quasistatic fracture toughness. ISO-12135-02. Geneva:ISO; 2002.

[41] ESIS procedure for determining the fracture behavior of materials. P2-92, ESIS, 1992.

[42] Tada H, Paris PC, Irwin GR. The stress analysis of cracks, 3rd ed., New York: The American Society of Mechanical Engineers; 2000.

[43] Cravero S, Ruggieri C. Estimation procedure of J-resistance curves for SE(T) fracture specimens using unloading compliance. Engng Fract Mech 2007;74:2735.

[44] Sumpter JDG, Turner CE. Method for Laboratory Determination of J_c. ASTM STP 1976;601:3.

[45] Turner CE. The ubiquitous η factor. ASTM STP 1980;700:647.

[46] Johnson HH. Calibrating the electrical potential method for studying slow crack growth. Mater Res Stan 1965;5:442.

[47] Maugin GA. Configurational Forces: Thermomechanics, Physics, Mathematics, and Numerics. Boca Raton: Chapman and Hall; 2010.

[48] Gurtin ME. Configurational forces as basic concepts of continuum physics. New York: Springer; 2000.

[49] Kienzler R, Herrmann G. Mechanics in material space. Berlin: Springer; 2000.
[50] Eshelby JD. The force on an elastic singularity, Phil. Trans. R. Soc. Lond. A. 1951;244:87.
[51] Maugin GA. Material Inhomogenieties in Elasticity. London: Chapman and Hall; 1993.
[52] Maugin GA. Material forces: Concepts and applications. ASME Appl. Mech. Rev. 1995;48:213.
[53] Maugin GA, Trimarco C. Pseudo-momentum and material forces in nonlinear elasticity: variational formulation and application to brittle fracture. Acta Mech 1992;94:1.
[54] Gurtin ME, Podio-Guidugli P. Configurational forces and the basic laws for crack propagation. J Mech Phys Solids 1996;44:905.
[55] Simha NK, Fischer FD, Shan GX, Chen CR, Kolednik O, J-integral and crack driving force in elastic–plastic materials. J Mech Phys Solids 2008;56:2876.
[56] Kolednik O, Predan J, Fischer FD. Cracks in inhomogeneous materials: Comprehensive assessment using the configurational forces concept. Engng Fract Mech 2010;77:3611.
[57] Simha NK, Fischer FD, Kolednik O, Chen CR. Inhomogeneity effects on the crack driving force in elastic and elastic–plastic materials. J Mech Phys Solids 2003;51:209.
[58] Simha NK, Fischer FD, Kolednik O, Predan J, Shan GX. Crack tip shielding or anti-shielding due to smooth and discontinuous material inhomogeneities. Int J Fract 2005;135:73.
[59] Fischer FD, Predan J, Kolednik O, Simha NK. Application of material forces to fracture of inhomogeneous materials: illustrative examples. Arch Appl Mech 2006;77:95.
[60] Kolednik O, Predan J, Shan GX, Simha NK, Fischer FD. On the fracture behavior of inhomogeneous materials – A case study for elastically inhomogeneous bimaterials. Int J Solids Struct 2005;42:605.
[61] Woesz A, Weaver JC, Kazanci M, Dauphin Y, Aizenberg J, Morse DE, Fratzl P. Micromechanical properties of biological silica in skeletons of deep-sea sponges. J Mater R 2006;21:2068.
[62] Dundurs J. Edge-bonded dissimilar orthogonal elastic wedges. ASME J Appl Mech 1969;36:650.
[63] Kolednik O. The yield stress gradient effect in inhomogeneous materials Int J Solids Struct 2000;37:781.

[64] Kolednik O, Predan J, Gubeljak N, Fischer DF. Modeling fatigue crack growth in a bimaterial specimen with the configurational forces concept. Mater Sci Eng A 2009;519:172.
[65] Aluminum and Aluminum Alloy Sheet and Plate. B-209M-04. Annual Book of ASTM Standards, ASTM; 2004.
[66] Schrader GF, Elshennawy AK. Manufacturing Processes & Materials, 4th ed. Society of Manufacturing Engineers; 2000.
[67] Groover MP. Fundamentals of Modern Manufacturing: Materials, Processes, and Systems, 4th ed. Wiley 2010.
[68] Urena A, Gomez De Salazar JM, Escalera MD. Diffusion bonding of an aluminum-copper alloy reinforced with silicon carbide particles (AA2014/SiC/13p) using metallic interlayers. Scripta Mater 1996;35:1285.
[69] Kim S-H, Kim H-W, Euh K, Kang J-H, Cho J-H. Effect of wire brushing on warm roll bonding of 6XXX/5XXX/6XXX aluminum alloy clad sheets. Mater Design 2012;35:290.
[70] Standard practice for heat treatment of wrought aluminum alloys. B-918-01. Annual Book of ASTM Standards, Vol. 02.02: ASTM; 2001.
[71] Schmied F. Atomic Force Microscopy investigations of fiber-fiber bonds in paper. PhD-thesis, University of Leoben, 2011.
[72] Cepeda-Jiménez, CM, Hidalgo P, Pozuelo M, Ruano OA, Carreño, F. Effect of thermal treatment on the interfacial shear toughness of an aluminium composite laminate. Mater Sci Eng A 2010;527:2579.
[73] Paris PC, Fatigue – An Interdisciplinary Approach, Proc. 10th Sagamore Conf, Syracuse University Press, 1964:107.
[74] Suresh S. Fatigue of Materials, 2nd ed. Cambridge University Press; 1998.
[75] Elber W. Fatigue crack closure under cyclic tension. Engng Fract Mech 1970;2:37.
[76] Elber W. Damage tolerance in aircraft structures, ASTM STP 486, Philadelphia, 1971, pp. 203.
[77] Marissen R. Fatigue crack growth in ARALL – A hybrid aluminium-aramid composite material, PhD-thesis, Delft, 1988.
[78] Pippan R. The effective threshold of fatigue crack propagation in aluminium alloys. I. The influence of yield stress and chemical composition. Philos Mag A 1998;77:861.
[79] Irwin GR. Plastic zone near a crack and fracture toughness. In: Sagamore Research Conference Proceedings, Vol. 4; 1961.
[80] http://www.3ds.com/products/simulia/portfolio/abaqus/overview/, 9/11/2012.
[81] Mueller R, Kolling S, Gross D. On configurational forces in the context of the finite element method. Int J Numer Meth Engng 2002;53:1557.
[82] Mueller R, Gross D, Maugin GA. Use of material forces in adaptive finite element methods. Comput Mech 2004;33:421.

[83] Denzer R, Barth FJ, Steinmann P. Studies in elastic fracture mechanics based on the material force method. Int J Numer Methods Engng 2003;58:1817.
[84] Schöngrundner R. Numerische Studien zur Ermittlung der risstreibenden Kraft in elastisch-plastischen Materialien bei unterschiedlichen Belastungesbedingungen. PhD-thesis, Leoben, 2010.
[85] D. Taylor, A compendium of fatigue thresholds and growth rates, EMAS, Warley, 1985.